CHARACTERIZING SINGLE ATOM DIPOLE TRAPS FOR QUANTUM INFORMATION APPLICATIONS

A Thesis
Presented to
The Academic Faculty

by

Chung-Yu Shih

In Partial Fulfillment
of the Requirements for the Degree
Doctor of Philosophy in the
School of Physics

Georgia Institute of Technology
May 2013

CHARACTERIZING SINGLE ATOM DIPOLE TRAPS FOR QUANTUM INFORMATION APPLICATIONS

Approved by:

Professor Michael S. Chapman,
Advisor
School of Physics
Georgia Institute of Technology

Professor Rick Trebino
School of Physics
Georgia Institute of Technology

Professor Kenneth R. Brown
School of Chemistry & Biochemistry
Georgia Institute of Technology

Professor Kurt Wiesenfeld
School of Physics
Georgia Institute of Technology

Professor T. A. Brian Kennedy
School of Physics
Georgia Institute of Technology

Date Approved: 19 Feb 2013

"If I have seen further it is by standing on the shoulders of giants."

- Isaac Newton

ACKNOWLEDGEMENTS

I would like to thank everyone who has played a part of my life throughout the years of my graduate study in Georgia Institute of Technology. To begin with, I would like to thank my advisor, Professor Michael Chapman, for giving me the opportunity to study the interaction between light and matter at Georgia Tech. Throughout my graduate career, I have greatly benefited from his experience and insightful suggestions when it comes to trying new things. Without his patient guidance and encouragement, much of the work in this thesis would not been possible.

I would also like to thank my colleagues for their efforts on many things. Dr. Paul Griffin showed me the techniques of laser spectroscopy in the first few months after I joined the lab. When I started to work on the cavity QED experiment, Dr. Peyman Ahmadi and Dr. Soo Kim showed me how to set up and run the experiment. Their determination and diligence in doing research have always provided encouragement to me when the experiment failed to work. Dr. Michael Gibbons showed me how to trap single atoms and measure their quantum state. I must also acknowledge help from Dr. Chris Hamley, for his knowledge on electronics. He is also generous in sharing thoughts and ideas on how to improve the experiment, many of which proved to be essential. Benjamin Land offered his expertise in numerical simulation, allowing me to compare the results of the many-atom cavity QED experiment to theory. I am fortunate to have the privilege of working with other talented people: Dr. Ghazal Behin-Aein, Dr. Adam Steele, Dr. Eva Bookjans, Dr. Layne Churchill, Michael DePalatis, Thai Hoang, Corey Gerving, Martin Anquez, and Brian Rose. They are an integral part of my life in Georgia Tech, and make the lab a very enjoyable place to do research.

Professor Brian Kennedy has offered his experience and expertise during many valuable discussions for which I am grateful. I would also like to thank other members of my thesis reading committee for their help on correcting this thesis: Professors Kenneth Brown, Rick Trebino, and Kurt Wiesenfeld.

Finally, I would like to thank my family members for being supportive and understanding throughout the years of my graduate career.

TABLE OF CONTENTS

LIST OF TABLES

LIST OF FIGURES

SUMMARY

Ultracold neutral atoms confined in optical dipole traps have important applications in quantum computation and information processing, quantum simulators of interacting-many-body systems and atomic frequency metrology. While optical dipole traps are powerful tools for cold atom experiments, the energy level structures of the trapped atoms are shifted by the trapping field, and it is important to characterize these shifts in order to accurately manipulate and control the quantum state of the system.

In order to measure the light shifts, we have designed a system that allows us to reliably trap individual ^{87}Rb atoms. A non-destructive detection technique is employed so that the trapped atoms can be continuously observed for over 100 seconds. Single atom spectroscopy, trap frequency measurements, and temperature measurements are performed on single atoms in a single focus trap and small number of atoms in a 1D optical lattice in order to characterize the trapping environment, the perturbed energy level structures, and the probe-induced heating.

In the second part of the thesis, we demonstrate deterministic delivery of an array of individual atoms to an optical cavity and selective addressability of individual atoms in a 1D optical conveyor, which serves as a potential candidate for scalable quantum information processing. The experiment is extended to a dual lattice system coupled to a single cavity with the capability of independent lattice control and addressability. The mutual interactions of atoms in different lattices mediated by a common cavity field are demonstrated. A semi-classical model in the many-atom regime based on the Jaynes-Cummings model is developed to describe the system that

is in good qualitative agreement with the data. This work provides a foundation for developing multi-qubit quantum information experiments with a dual lattice cavity system.

CHAPTER I

INTRODUCTION

The foundation of modern atomic physics was established by the dramatic development of quantum physics in the first three decades of the twentieth century. Landmarks in this development include the quantum nature of radiation introduced by Planck [1], Einstein's hypothesis of quantized radiation energy to explain the photoelectric effect [2], the model introduced by Bohr explaining the quantized nature of the hydrogen atom energy level [3, 4], the Stern-Gerlach experiment suggesting the quantization of space [5], and the demonstration by Compton that the X-rays scattered by the electrons have a wavelength shift that can only be explained by the particle nature of electromagnetic wave [6]. In the 1920s and early 1930s, the work by Heisenberg, Schrödinger, Dirac [7], Hilbert [8], and von Neumann [9] set the foundation of the mathematical formulation of quantum mechanics that we still use today.

Over the following decades, significant progress was made in experiments with atomic and molecular beams [10]. In 1939, Rabi demonstrated that the nuclear magnetic moment could be measured by the resonance absorption of an oscillating magnetic field, and the nuclear magnetic moments of fluoride and several lithium isotopes are measured with molecular beams [11]. In the 1950s, Ramsey's work on developing the separated oscillatory field method [12] led to accurate measurements of the hyperfine splitting of the cesium ground states, which was later adopted as the primary frequency standard and the first cesium atomic clock was made in 1955 [13].

The work by Townes, Schawlow [14], Gould, Basov, and Prokhorov in the late 1950s had led to the demonstration of the first laser by Maiman in 1960 [15]. The

invention of laser revolutionized many fields of science and technology, not the least of which is atomic physics. Significant progress in the field of spectroscopy was made after the invention of tunable dye laser in 1967. One of the essential application of laser is the cooling of atoms, which was proposed in 1975 by Hänsch, Schawlow [16], Wineland, and Dehmelt [17]. The developments of laser cooling and trapping led to the realization of the Bose-Einstein condensation with alkali atoms [18]. In 1997, the Nobel prize was awarded to Chu, Phillips, and Cohen-Tannoudji for developments of cooling and trapping atoms with laser [19–21]. In 2001, the Nobel prize was awarded to Cornell, Ketterle, and Wieman for the achievement of Bose-Einstein condensation. In less than two decades, laser cooling and atom trapping have become standard techniques for atomic physicists.

1.1 Neutral Atom Trapping And Its Application To Quantum Information Science

Since the first demonstration of laser cooling and trapping neutral atoms, most of the experiments have focused on trapping large number of atoms ($10^3 \sim 10^9$). However, in parallel, there has been increasing interest and progress in trapping individual neutral atoms. The motivation is to develop registers of neutral atom qubits for the field of quantum information science. Cooling and trapping single atoms in a magneto-optical trap (MOT) was first accomplished by Kimble's group in 1994 [22]. Loading of single atoms into a optical dipole trap was demonstrated by Meschede's group in 2000 [23]. In 2001, Grangier's group demonstrated the sub-Poissonian loading of single atoms in tightly focused optical dipole traps [24]. In 2004, Meschede's group utilized neutral atom as quantum registers [25]. Recently, near-deterministic preparation of single atoms in microtraps [26], and ground state cooling of single atoms in a single focus trap [27, 28] have also been demonstrated. Large scale quantum registers can be achieved by building arrays of single-atom traps, with independent control of the atoms in the trap. Alternatively, registers can also be realized by trapping large

number of distinguishable atoms with single atom addressability in optical lattices, which were demonstrated in a 3D optical lattice with 4.9 μm lattice spacing [29], in a quantum gas microscope with 640 nm lattice spacing [30], and in a 1D optical lattice with a periodicity of 433 nm [31].

Entanglement between neutral atoms was demonstrated with individually trapped neutral atoms. In 2006, Weinfurter's group successfully created entanglement between a single photon and a neutral single atom in free space [32]. A Rydberg blockade between two individual atoms was observed in 2009 [33, 34], leading to the creation of entanglement between two neutral atoms using Rydberg blockade in the following year [35]. The recent progress in utilizing optically trapped neutral atoms as quantum registers is promising, and it is important to improve the storage and coherence time of the registers by characterizing the trapping environment.

Optical trapping of neutral atoms is a powerful technique for atomic physicists, however, there is one important issue that complicates its use for precise spectroscopy and quantum information processing: optical dipole traps induce state dependent light shifts on the trapped atoms, typically, on the order of tens of MHz for the excited states [36–39]. For quantum information applications that utilize hyperfine ground states as qubits, the differential light shifts of the hyperfine clock transition is the major source of decoherence. On the other hand, coherent manipulation and laser cooling rely on precise control of the laser detuning from the light shifted transition resonances. Therefore, it is important to measure the light shifts of the optically trapped atoms. Various techniques have been used to measure the AC-Stark shift for optically trapped neutral atoms. For instance, a destructive imaging technique was performed with cesium atoms to measure the differential light shift of the D2 transition [37], where a strong, unidirectional, and near resonant beam is applied to kick the atom out of the trap for different frequency detunings. In other work, the

transmission spectra of singly trapped ^{87}Rb atoms were obtained and showed a polarization dependent light shift difference of 20 MHz between the $|F = 2, m_F = \pm 2\rangle \rightarrow |F' = 3, m_{F'} = \pm 3\rangle$ transitions in a circularly polarized far-off-resonant trap (FORT) at 980 nm [39]. Shifts of higher level states were measured using Rydberg excitation spectrum of the ^{85}Rb $5P \rightarrow 50S$ transition in a FORT at 1064 nm [36]. Finally, measurements of the AC-Stark shift for the ^{87}Rb $14D_{5/2}$ Rydberg state was determined by a photoionization spectrum [38].

One of the goals of this thesis is to characterize the trapping environments of the optical dipole traps for single atoms by measuring the atom lifetime in the trap, the forced oscillation of the atom in the trap (to measure the trap frequency), the temperature of the atom, and the AC-Stark shifts of the D2 transition manifold. Along the way, a new detection technique is developed, which enables us to observe one and the same atom for up to hundreds of seconds. In the following chapters, the theoretical background of optical dipole trapping and the results of the experiments will be presented.

The single atom experiment in our group was established by my predecessor, Dr. Michael Gibbons, with the initial purpose of studying atom heating mechanisms and achieving long atom lifetimes in a 1D optical lattice [40]. The study was later focused on demonstrating non-destructive measurements of the hyperfine states of single atoms, with the individual atoms being initialized and detected over 100 times before getting lost from the trap. Hyperfine state measurements of single atoms was demonstrated with 95% accuracy and 1% loss rate [41]. Although these experiments demonstrated the ability to measure the hyperfine state of the single atoms and reuse them many times to increase the repetition rate, much work remains before it can be implemented for large-scale quantum information architecture.

1.2 Cavity Quantum Electrodynamics

The interaction between a single atom and a single mode of electromagnetic field represents a fundamental form of matter-light interaction in nature, and has long been a major research topic in the fields of atomic physics and quantum optics [42–44]. The rate of interaction between an atom and a photon can be enhanced by making an optical resonator with highly reflective mirrors, creating a strongly interacting atom-field system. In 1946, Edward Purcell proposed that the spontaneous emission rate of the atoms can be enhanced in a cavity resonant with the respective transition [45]. The presence of the atoms in the cavity changes the energy spectrum of the system such that the atoms and the cavity light field can not be considered separately [46]. Spontaneous emission of photons can be understood as the stimulated emission induced by the vacuum fluctuation of the electromagnetic field. In the case where the coupling between the atom and the cavity light field is stronger than the coupling between the atom and the environment, a photon emitted into the cavity can re-excite the atom many times before escaping from the system, and the system is considered to be in the strong coupling regime.

The early work in cavity QED were performed using microwave cavities with Rydberg atoms [47–50]. It was later extended to the optical domain where the vacuum Rabi splitting was observed in a cavity system with twenty atoms by Raizen *et al.* in 1989 [51]. In 1992, this phenomenon was also observed in a microwave cavity with as few as three atoms by Haroche's group [52]. In the same year, the observation of vacuum Rabi splitting for a single cesium atom was reported by Thompson *et al.* [53].

A single-atom cavity system in the strong coupling regime serves as a promising candidate for quantum information science due to higher entanglement probability compared to atoms trapped in free space. Deterministic delivery of single atoms to the cavity has been demonstrated [54–56], and deterministic generation of single

photons by single atoms in the cavity was demonstrated by Kuhn *et al.* [57]. In 2007, Wilk *et al.* [58] showed that the entanglement between a single photon and a single atom in the cavity could be created and that the state of the atom could be mapped onto another photon thus creating a entangled photon pair. In 2011, remote entanglement between a single atom in the cavity and a Bose-Einstein condensate was created by Lettner *et al.* in a similar fashion [59]. Cavity systems have also enabled new studies in nonlinear physics such as the dynamical fluctuations and bifurcations [60], nonlinear optics [61], and detection of atomic motion [62, 63].

Cavity QED can also be realized in solid-state systems such as superconducting circuits, semiconductors, and photonic crystals. In 2004, strong coupling cavity QED with a superconducting qubit and a single photon was observed in a superconducting circuit (so-called "circuit-QED") [64]. Vacuum Rabi splitting was also shown with a single quantum dot coupled to a cavity in the photonic crystal [65] and to a semiconductor microcavity [66].

The cavity QED experiments in this lab were first established by Dr. Jacob Sauer in 2002. The interaction of the cavity with the optically transported atoms was demonstrated in 2003 [67]. Over the following few years, several major improvements have been made to the cavity and laser systems. In 2007, the deterministic delivery of single atoms to the cavity was reported by Dr. Kevin Fortier and Dr. Soo Kim [55]. I joined this project in January 2008, and the experiment was expanded to dual optical lattices coupled to a single cavity.

In this thesis, we demonstrate deterministic delivery of an array of individual ^{87}Rb atoms to an optical cavity and selective addressability of individual atoms in a 1D optical conveyor; which is followed by coupling neutral atoms in dual quantum registers to a high-finesse optical cavity. In the latter case, an initial attempt is made to identify individual atoms in two independently controlled optical lattices and bring a pair of atoms back for coherent interaction through the cavity mode. The motivation

for developing a dual lattice cavity system with single atom selective addressability is to provide an alternative route for scalable quantum information processing designs. As an intermediate step to achieve this goal, the dynamical interaction between atoms in these two independently controlled conveyor belts was observed and compared to a semi-classical Hamiltonian in the multi-atom regime.

1.3 Thesis Organization

This thesis covers two major topics. Chapter 2 focuses on the theory background of optical dipole trapping and its induced light shifts on ^{87}Rb atoms. Chapter 3 begins with the fundamentals of the cavity system, followed by introducing the Jaynes-Cummings Hamiltonian of a single-atom cavity QED system. Later in the same chapter, different methods of numerically simulating the multi-atom cavity system are compared for their respective efficiencies and accuracies. In Chapter 4, the construction of experiment chamber, detection system, laser setup, and laser detuning schemes are discussed. In Chapter 5, the technique of gated probing/cooling of individual atoms is introduced which enables long storage time and high repetition rate. Chapter 6 details the experimental results of the deterministic delivery, selective addressability, and the cavity field dynamics of the dual lattice cavity system. This thesis concludes providing future outlook for both experiments in Chapter 7. Finally, Appendix A includes a possible way to improve the atom transfer technique for the cavity QED experiment.

CHAPTER II

OPTICAL DIPOLE TRAP AND AC-STARK SHIFTS

Neutral atom cooling and trapping have become important techniques in modern atomic physics and quantum optics laboratories since the landmark demonstrations of optical dipole traps [68] and magneto-optical traps (MOTs) [69] almost 3 decades ago. The particular focus of this work is laser-cooled individual neutral atoms confined in optical dipole traps [23], which have important applications in quantum computation and information processing [35, 70–72], and in quantum simulators of many-body systems [73]. Optical dipole traps can be used to hold cold atoms with lifetimes exceeding 100 seconds [40], limited only by the background pressure and thus provide a promising alternative to trapped ion based scalable quantum information processing designs. However, one important issue with optically trapped atoms is that the optical trapping fields intrinsically shift the energy levels of the atoms, thereby altering the very energy levels in which the information is stored. Different light shifts are important for different applications. The average light shift of the ground states defines the trapping potential. Together with the average light shift of the excited states, they shift the optical transition energies which are important for laser cooling and coherent state manipulation of the atoms. On the other hand, the differential light shifts of the hyperfine clock transition is a major source of decoherence for qubits that utilize these states [74]. The differential light shifts within the excited state hyperfine manifold are several orders of magnitude larger than the those of the ground state and are essential for coherent state control within the hyperfine manifold. Spatial varying trapping field intensity causes differential light shifts for thermal atoms and are important for frequency metrology with optically trapped atoms.

For typical far-off resonant traps with the ∼1 mK depths, the state dependent excited state differential light shifts induced by the trap laser beam can easily exceed tens of MHz [36–39], which is larger than the typical excited state transition width. For certain transitions, it is possible to find trap laser wavelengths (so-called "magic wavelengths") that shift the ground and the excited states by the same amount so that the transition experiences no light shift [75, 76]. On the other hand, the differential light shifts within the ground state manifold are much smaller compared to those of the excited states, typically on the order of 100 kHz in a 1 mK trap [39]. For photon polarization and spin-wave qubits that employ the $m_F = 0 \leftrightarrow m_{F'} = 0$ clock transition between the hyperfine ground states, the differential light shifts cause dephasing and hence shorten the storage time. Cancellation of the differential light shifts of the clock transition with the quadratic Zeeman shifts has been proposed for circularly and elliptically polarized optical traps [74, 77, 78]. These techniques are employed in the experiments where extreme precision and coherence between states are needed such as frequency metrology [79–82] and quantum information processing [83, 84].

In this chapter, we present the relevant theoretical background of neutral atom dipole traps and the determination of induced AC-Stark shifts for the relevant energy states. We will later discuss temperature measurements of the individually trapped atoms. The temperature measurements are used to quantify the thermal motion of the atoms in the optical dipole traps, which in turn alter the light shifts and other properties of the atomic spectrum. In the last section, discussion on linewidth broadening due to the thermal motion of the atoms will be introduced.

2.1 Optical Dipole Trap

In this section, we present a classical model of an optical dipole trap for a polarizable object [85]. The model is applicable to any neutral, polarizable object placed in the light field, including atoms [68], molecules and mesoscopic objects such as viruses,

bacteria [86] and dielectric glass beads.

The optical dipole force acting on a polarizable object derives from the interaction between the light field gradient and the induced electric dipole moment. The time averaged potential energy of the polarizable object in the external field is given by

$$U = -\frac{1}{2}\langle \vec{p} \cdot \vec{E} \rangle = -\mathrm{Re}(\alpha)\left|\vec{E}\right|^2 = -\frac{1}{2\epsilon_0 c}\mathrm{Re}(\alpha) I, \tag{2.1}$$

where $\vec{p} = \alpha \vec{E}$ is the dipole moment of the polarized object, α is the frequency dependent complex polarizability, I is the intensity of the light, and the angular brackets denote the time average over the oscillating light field. The dipole force acting on the object is,

$$F(\vec{r}) = -\boldsymbol{\nabla} U = \frac{1}{2\epsilon_0 c}\mathrm{Re}(\alpha)\boldsymbol{\nabla} I(\vec{r}). \tag{2.2}$$

For a neutral atom, it is possible to use the Lorentz's model of a classical oscillator to estimate the polarizability of the neutral atom. This model considers the electron bound to the atom with a spring with spring constant k_{spring} such that the natural oscillation frequency ω_0 of the system is,

$$\omega_0 = \sqrt{\frac{k_{spring}}{m_e}}, \tag{2.3}$$

where m_e is the mass of the electron. For an atom in the external electric field oscillating at a frequency ω_0, the equation of motion of the electron can be written as,

$$\ddot{x} + \Gamma_\omega \dot{x} + {\omega_0}^2 x = -\frac{eE}{m_e} e^{-i\omega t}. \tag{2.4}$$

The damping force in Eq. 2.4 is given by Larmor's formula for an accelerating charged particle [87, 88],

$$\Gamma_\omega = \frac{e^2\omega^2}{6\pi\epsilon_0 m_e c^3} \tag{2.5}$$

By solving the equation of motion and using $\vec{p} = \alpha\vec{E}$, the frequency dependent polarizability can be obtained,

$$\alpha(\omega) = \frac{e^2}{m_e}\frac{1}{\omega_0^2 - \omega^2 - i\omega\Gamma_\omega}, \tag{2.6}$$

Defining the classical on-resonant damping rate $\Gamma \equiv (\frac{\omega_0}{\omega})^2\Gamma_\omega$, Eq. 2.6 can be expressed as,

$$\alpha(\omega) = 6\pi\epsilon_0 c^3 \frac{\frac{\Gamma}{\omega_0^2}}{\omega_0^2 - \omega^2 - i\frac{\omega^3}{\omega_0^2}\Gamma}. \tag{2.7}$$

Substituting into Eq. 2.1, the dipole potential takes the following form

$$U(\vec{r}) = -\frac{3\pi c^2}{2{\omega_0}^3}\Big(\frac{\Gamma}{\omega_0 - \omega} - \frac{\Gamma}{\omega_0 + \omega}\Big)I(\vec{r}). \tag{2.8}$$

For laser frequencies red-detuned with respect to the atomic transition ($\omega < \omega_0$), the dipole potential is less than zero; hence, the atoms will be attracted towards the intensity maximum of the beam. For laser frequencies blue-detuned to the atomic transition ($\omega > \omega_0$), the dipole potential is greater than zero; thus, the atoms are pushed away from the beam. Although it is possible to trap atoms with either detuning, blue-detuned traps generally require more complicated experimental setups [89].

2.2 Single Focus Trap

The simplest way to construct an optical dipole trap using a red-detuned laser is to focus a collimated Gaussian beam. The spatial intensity profile of a Gaussian beam with a minimum waist w_0 located at z=0 is

$$I(r, z) = \frac{2P}{\pi w(z)^2}\exp\Big(-\frac{2r^2}{w(z)^2}\Big), \tag{2.9}$$

$$w(z) = w_0\sqrt{1 + \Big(\frac{\lambda}{\pi w_0^2}\Big)^2 z^2}, \tag{2.10}$$

where P is the power of the trap laser and $w(z)$ is the beam waist as a function of the propagation direction. Substituting into Eq. 2.8, we obtain the trap depth of a single focus trap,

$$U(r,z) = U_0 \frac{w_0^2}{w(z)^2} \exp\Big(- \frac{2r^2}{w(z)^2} \Big), \tag{2.11}$$

$$U_0 = -\frac{3Pc^2}{w_0^2 \omega_0^3} \Big(\frac{\Gamma}{\omega_0 - \omega} - \frac{\Gamma}{\omega_0 + \omega} \Big). \tag{2.12}$$

2.3 1D Optical Lattice

A 1D optical lattice can be constructed by overlapping two counter-propagating beams with the same polarization. Consider the total electric field of two plane waves with angular frequency $\omega_1 = \omega$ and $\omega_2 = \omega + \delta$ traveling in the opposite direction,

$$\begin{aligned} \mathbf{E}(z,t) &= \mathbf{E}_1(z,t) + \mathbf{E}_2(z,t) \\ &= E_0 \hat{\boldsymbol{\epsilon}} e^{i(kz - \omega t)} + E_0 \hat{\boldsymbol{\epsilon}} e^{i(-kz - \omega t - \delta t)} \\ &= 2E_0 \hat{\boldsymbol{\epsilon}} e^{-i\omega t} \cos\Big(kz - \frac{\delta t}{2} \Big), \end{aligned} \tag{2.13}$$

where $k = 2\pi/\lambda$ is the wave number, $\hat{\boldsymbol{\epsilon}}$ is the unit polarization vector, and E_0 is the electric field amplitude. The intensity of these two overlapping plane waves carries a time-dependent factor, $\cos^2(kz - \frac{\delta t}{2})$. For $\delta = 0$, the result is a standing wave with a $\cos^2(kz)$ spatial intensity variation. For $\delta \neq 0$, a walking wave is created with translational velocity $v = \delta\lambda/4\pi$. Note that the factor of 2 in the above equation corresponds to a factor of 4 in the intensity and hence the 1D lattice trap made with a retro-reflected beam is $4\times$ deeper than the corresponding single focus trap.

In the experiments described in this thesis, a 1D optical lattice is created by overlapping two counter-propagating and focused Gaussian beams with the foci at the same position as shown in Figure 1. Similar to Eq. 2.9, the intensity profile of this 1D optical lattice can be expressed as,

$$I(r,z) = \frac{8P}{\pi w(z)^2} \cos^2\Big(kz - \frac{\delta t}{2} \Big) \exp\Big(- \frac{2r^2}{w(z)^2} \Big). \tag{2.14}$$

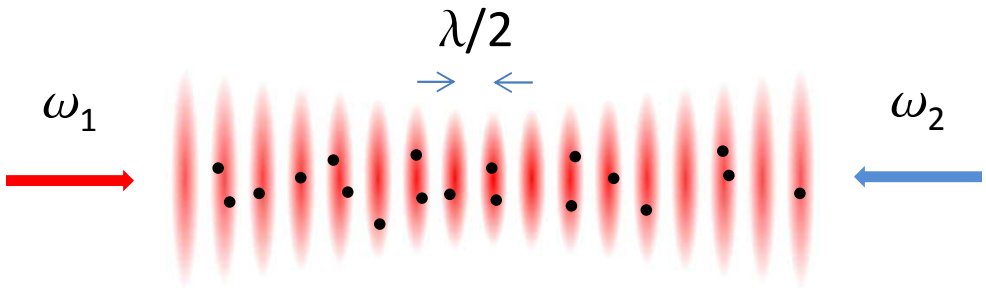

Figure 1: Illustrative diagram of a 1D optical lattice created by two counter-propagating and focused Gaussian beams.

The trapping potential is given by,

$$U(r,z) = 4U_0 \frac{w_0^2}{w(z)^2} \cos^2\Big(kz - \frac{\delta t}{2}\Big) \exp\Big(-\frac{2r^2}{w(z)^2}\Big), \tag{2.15}$$

where U_0 is defined in Eq. 2.12.

2.4 Time Dependent Perturbation Theory Approach

The semi-classical theory discussed in Section 2.1 works well for determining the trapping potential (i.e., the ground state light shift) in an optical dipole trap, within the two-level atom approximation. This simple model neglects the dipole interactions between trapping field and the multi-level structures of the atom. Therefore, it fails to describe the differential light shifts of the excited states and ground states. In order to calculate the energy shifts for individual sublevels within the hyperfine state manifold, the multi-level structure of the atom and the dipole moments of various transitions have to be considered. Since the energy shifts are small compared to the energy differences between levels, we can use perturbation theory.

Conventional spectroscopic notation labeling scheme for the atomic eigenstates will be used throughout the thesis:

$$n^{2S+1}L_J, \tag{2.16}$$

where n is the principal quantum number, S is the electron spin, L is the orbital angular momentum, and J is the total angular momentum not including nuclear

spin. Including nuclear spin, the total angular momentum of the atom is given by

$$\mathbf{F} = \mathbf{J} + \mathbf{I_n}, \tag{2.17}$$

where $\mathbf{I_n}$ is the nuclear spin operator.

Dirac notation, $|F, m_F\rangle$, is used to label the hyperfine states and the hyperfine sublevels of the atom, where F is the total angular momentum of the atom and m_F is the projection of F on the quantization axis.

2.4.1 System Formulation

The Hamiltonian H for an atom interacting with an oscillating electromagnetic field can be written as,

$$H = H_0 + V(t), \tag{2.18}$$

$$V(t) = V_+(\vec{r})e^{i\omega t} + V_-(\vec{r})e^{-i\omega t}. \tag{2.19}$$

where H_0 is the time independent Hamiltonian of the atom and $V(t)$ represents the interaction between the atom and the oscillating electromagnetic wave in the dipole approximation. The unperturbed Hamiltonian has energy eigenvalues E_n and energy eigenstates $|n\rangle$ defined as,

$$H_0 \left|n\right\rangle = E_n \left|n\right\rangle. \tag{2.20}$$

An arbitrary state $|\alpha\rangle$ can be expressed as,

$$\left|\alpha\right\rangle = \sum_n c_n \left|n\right\rangle. \tag{2.21}$$

In the interaction picture, the state ket $|\alpha(t)\rangle_I$ and the operator for the observable V_I are defined as

$$\left|\alpha(t)\right\rangle_I = \exp\Big(\frac{iH_0t}{\hbar}\Big) \left|\alpha(t)\right\rangle_S, \tag{2.22}$$

$$V_I = \exp\Big(\frac{iH_0t}{\hbar}\Big)V\exp\Big(\frac{-iH_0t}{\hbar}\Big). \tag{2.23}$$

The time evolution of state $|\alpha(t)\rangle_I$ is characterized by the following equation,

$$i\hbar\frac{\partial}{\partial t}|\alpha(t)\rangle_I = V_I\,|\alpha(t)\rangle_I\,, \tag{2.24}$$

which can be derived by taking the time derivative of Eq. 2.22.

In order to obtain the differential equation for $c_n(t)$, we multiply both sides of Eq. 2.24 by $\langle n|$,

$$i\hbar\frac{\partial}{\partial t}\langle n|\alpha(t)\rangle_I \;=\; \sum_m \langle n|\,V_I\,|m\rangle\,\langle m|\alpha(t)\rangle_I. \tag{2.25}$$

Substituting

$$\langle n|\exp\Big(\frac{iH_0t}{\hbar}\Big)V(t)\exp\Big(\frac{-iH_0t}{\hbar}\Big)\,|m\rangle = \langle n|\,V(t)\,|m\rangle\exp\Big(\frac{i(E_n-E_m)t}{\hbar}\Big)$$

and

$$c_n(t) = \langle n|\alpha(t)\rangle_I$$

into Eq. 2.25, we get

$$\begin{aligned} i\hbar\frac{dc_n(t)}{dt} &= \sum_m \langle n|\,V(t)\,|m\rangle\exp\Big(\frac{i(E_n-E_m)t}{\hbar}\Big)c_m(t), \\ &= \sum_m \langle n|\,V(t)\,|m\rangle\,e^{i\omega_{nm}t}c_m(t), \end{aligned} \tag{2.26}$$

with

$$\omega_{nm} \equiv \frac{E_n - E_m}{\hbar} = -\omega_{mn} \tag{2.27}$$

By putting Eq. 2.26 into integral form, we obtain the iterative solution in the following form,

$$c_n(t) = c_n^{(0)} + c_n^{(1} + c_n^{(2)} + \cdots\,. \tag{2.28}$$

Therefore, the state of the atom in the external perturbation can be evaluated to designated accuracy by obtaining the corresponding iterative solution for $c_n(t)$.

2.4.2 Floquet Formalism

To derive the light shifted energies for different atomic states, we apply the Floquet formalism [90–93] and calculate the first non-zero correction term to the energy. The resulting second order light shift takes the following form,

$$\Delta_n = \sum_l \{ \frac{|\langle n| V_+(\vec{r}) |l\rangle|^2}{\hbar(\omega_n - \omega_l + \omega)} + \frac{|\langle n| V_-(\vec{r}) |l\rangle|^2}{\hbar(\omega_n - \omega_l - \omega)} \}. \tag{2.29}$$

The form of $V_\pm(\vec{r})$ depends on the unit vector of the field polarization and the electric dipole moment operator $\boldsymbol{\mu}$,

$$V_+(\vec{r}) = -\frac{E_0}{2}(\hat{\boldsymbol{\epsilon}}^* \cdot \boldsymbol{\mu}), \quad V_-(\vec{r}) = -\frac{E_0}{2}(\hat{\boldsymbol{\epsilon}} \cdot \boldsymbol{\mu}), \tag{2.30}$$

where $\boldsymbol{\mu}$ is a Hermitian operator and the transition dipole moment for $|n\rangle \to |l\rangle$ is given by $\langle n| \boldsymbol{\mu} |l\rangle$. E_0 is the amplitude of the electric field, which is related to the time averaged Poynting vector $\langle S \rangle$ by

$$\langle \mathbf{S} \rangle = \frac{1}{2\mu_0 c} E_0^2 \hat{\mathbf{k}}, \tag{2.31}$$

and $\hat{\boldsymbol{\epsilon}}$ is the complex unit polarization vector which satisfies

$$\begin{aligned} \hat{\boldsymbol{\epsilon}}^* \cdot \hat{\boldsymbol{\epsilon}} &= 1, \\ \hat{\boldsymbol{\epsilon}} \cdot \hat{\mathbf{k}} &= 1, \\ \hat{\boldsymbol{\epsilon}}^* \times \hat{\boldsymbol{\epsilon}} &= i\mathcal{P}\hat{\mathbf{k}}. \end{aligned} \tag{2.32}$$

$\hat{\mathbf{k}}$ is the unit wave vector and $\mathcal{P}$ is the degree of circular polarization. $\mathcal{P} = 0$, 1, and -1 correspond to linearly, right circularly, and left circularly polarized light, respectively. The discussion of the above light shift calculation can therefore be applied to electromagnetic wave with arbitrary polarization and propagation direction. In the following section, we will begin with the special case where the trap beam is linearly polarized, one of most common optical trap configurations used in the lab.

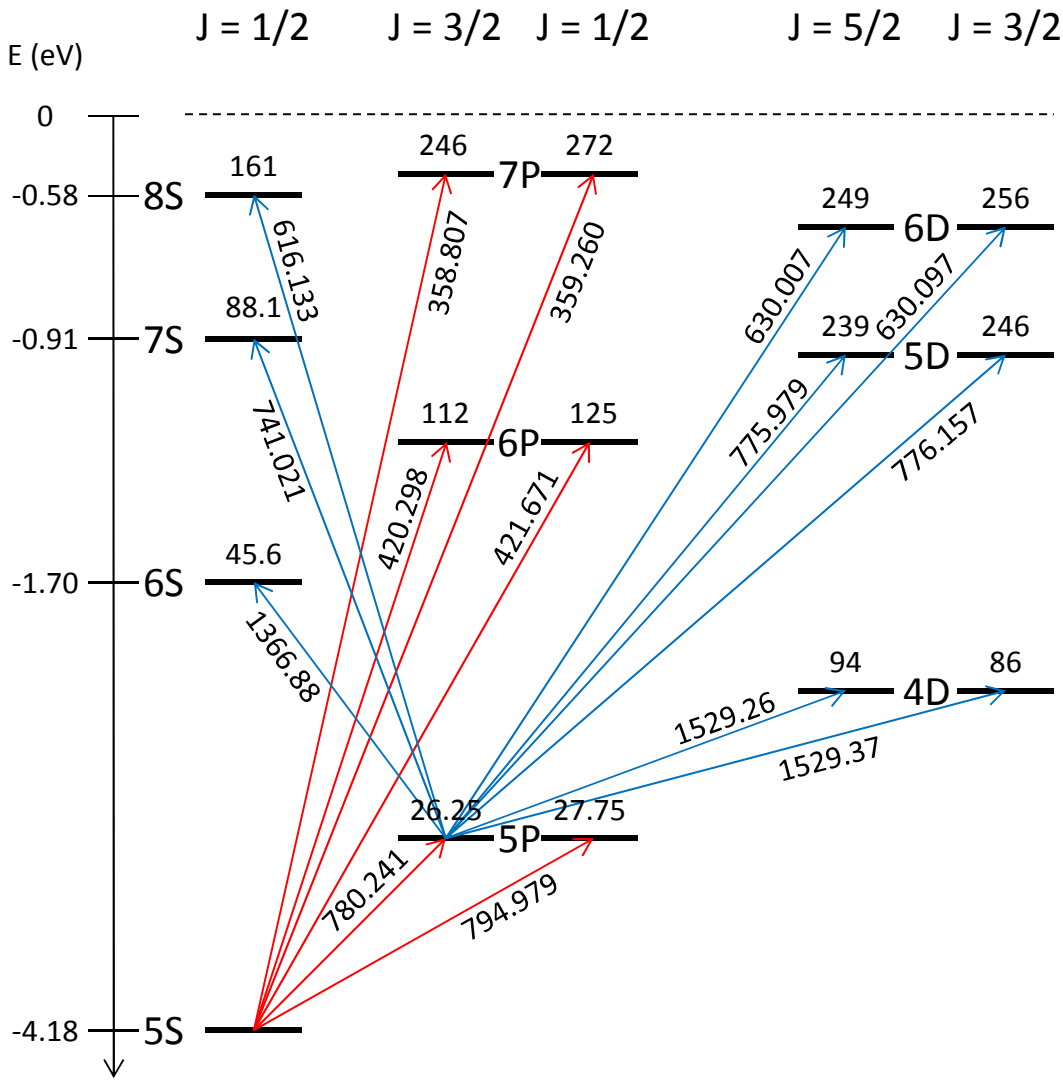

Figure 2: Grotrian diagram of the major dipole-allowed transitions to the $5S_{1/2}$, $|F = 2, m_F\rangle$ and $5P_{3/2}$, $|F' = 3, m_{F'}\rangle$ states. The excited states lifetimes are labeled on top of the states and are in the unit of nanoseconds. The wavelengths for each transition are in the unit of nanometers. The vertical axis is the energy of the electronic state and is not drawn to scale.

2.5 Linearly Polarized Optical Dipole Trap

In this section, we focus on the case of a linearly polarized dipole trap laser, polarized along the direction of the quantization axis. We will calculate the trapping potential as well as the energy shifts of the $5P_{3/2}$, $|F' = 3, m_{F'}\rangle$ excited states. The interaction potential $V_{\pm}(\vec{r})$ in this case can be written,

$$V_{+}(\vec{r}) = V_{-}(\vec{r}) = -\frac{E_0}{2} e r_0, \tag{2.33}$$

and Eq. 2.29 can be expressed in terms of the relevant quantum number and the specified geometry as follows

$$\Delta_{F,m_F} = \frac{E_0^2}{4\hbar} \sum_{F',m_{F'}} \left\{ \frac{|\langle F, m_F| \, e r_0 \, |F', m_{F'}\rangle|^2}{\omega_F - \omega_{F'} + \omega} + \frac{|\langle F, m_F| \, e r_0 \, |F', m_{F'}\rangle|^2}{\omega_F - \omega_{F'} - \omega} \right\}. \tag{2.34}$$

Note that the quantum numbers n, J, and L are omitted in the above equation for simplicity. The summation is carried over all the dipole allowed transitions from the unprimed state. The quantization axis of the system is chosen to be the z-axis, and $r_{0,\pm1}$ are the components of the irreducible rank-one tensor in the spherical basis: $r_0 = z$, $r_{\pm1} = \mp(x \pm iy)/\sqrt{2}$. The matrix elements $\langle F, m_F| \, e r_q \, |F', m_{F'}\rangle$ can be written as the product of the reduced matrix element, the Clebsch-Gordan coefficient, and the Wigner 6-j symbol by using the Wigner-Eckart theorem [94, 95]

$$\begin{aligned}
\langle F, m_F| \, e r_q \, |F', m_{F'}\rangle =& \langle F \| e\vec{r} \| F' \rangle \langle F, m_F | F', 1, m_{F'}, q \rangle \\
=& \langle F \| e\vec{r} \| F' \rangle (-1)^{F'-1+m_F} \sqrt{2F+1} \begin{pmatrix} F' & 1 & F \\ m_{F'} & q & -m_F \end{pmatrix}_{3j} \\
=& \langle n, L, J \| e\vec{r} \| n', L', J' \rangle (-1)^{2F'+J+I_n+m_F} \\
& \sqrt{(2F+1)(2F'+1)(2J+1)} \\
& \begin{pmatrix} F' & 1 & F \\ m_{F'} & q & -m_F \end{pmatrix}_{3j} \begin{Bmatrix} J & J' & 1 \\ F' & F & I_n \end{Bmatrix}_{6j}.
\end{aligned} \tag{2.35}$$

The reduced matrix element $\langle n, L, J \| e\vec{r} \| n', L', J' \rangle$ is the transition dipole moment (for simplicity, $\langle J \| e\vec{r} \| J' \rangle$ will be used instead), which can be calculated given the lifetime of the particular transition $\tau_{J'J}$ [96]

$$\frac{1}{\tau_{J'J}} = A_{J'J} = \frac{\omega_{FF'}^3}{3\pi\epsilon_0\hbar c^3} \frac{2J+1}{2J'+1} \left| \langle J \| e\vec{r} \| J' \rangle \right|^2 . \tag{2.36}$$

$A_{J'J}$ is the transition rate, also known as the Einstein A coefficient. The total lifetime of the excited state $\tau_{J'}$ is given by

$$\tau_{J'} = (\sum_J 1/\tau_{J'J})^{-1} = (\sum_{J'} A_{J'J})^{-1}. \tag{2.37}$$

The summation is carried over all decay channels to the lower lying states. Eq. 2.36 has another form which is commonly used in literature, [97]

$$A_{J'J}(s^{-1}) = \frac{2.02613 \times 10^{18}}{\lambda^3} \frac{2J+1}{2J'+1} \left| \langle J \| e\vec{r} \| J' \rangle \right|^2 . \tag{2.38}$$

Eq. 2.36 is in SI units whereas in Eq. 2.38 λ is in Å and $\langle J \| e\vec{r} \| J' \rangle$ is in atomic units. The reduced matrix elements have the following normalization convention [95],

$$\sum_{m_{J'}} \left| \langle J, m_J | \, e\vec{r} \, | J', m_{J'} \rangle \right|^2 = \sum_{m_{J'}, q} \left| \langle J, m_J | \, e r_q \, | J', m_{J'} \rangle \right|^2 = \left| \langle J \| e\vec{r} \| J' \rangle \right|^2 \tag{2.39}$$

Note that $(2J+1) \left| \langle J \| e\vec{r} \| J' \rangle \right|^2 = (2J'+1) \left| \langle J' \| e\vec{r} \| J \rangle \right|^2$, but the equalities in Eq. 2.36 and Eq. 2.38 do not hold if we switch J and J' for the case that $J \neq J'$. The only way to get around this is to enforce that J' be the orbital angular momentum of the excited state.

Together with Eq. 2.35 and 2.36, Eq. 2.34 can be rewritten in the following form,

$$\begin{aligned} \Delta_{F,m_F} = & \frac{3\pi I c^2}{2} \sum_{F', M_{F'}} \frac{A_{J'J}}{\omega_{FF'}^3} \left(\frac{1}{\omega_{FF'} + \omega} - \frac{1}{\omega_{FF'} - \omega} \right) \\ & (2F+1)(2F'+1)(2J'+1) \\ & \begin{pmatrix} F' & 1 & F \\ m_{F'} & 0 & -m_F \end{pmatrix}_{3j}^2 \begin{Bmatrix} J & J' & 1 \\ F' & F & I_n \end{Bmatrix}_{6j}^2 , \end{aligned} \tag{2.40}$$

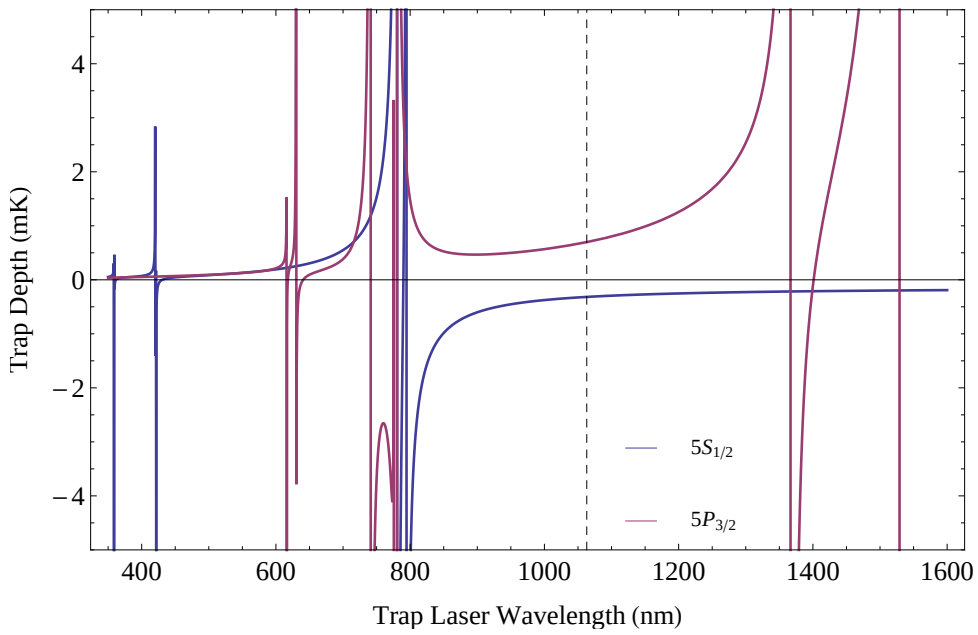

Figure 3: AC-Stark shifts of the $5S_{1/2}$, $|F = 2, m_F = 0\rangle$ (blue) and the $5P_{3/2}$, $|F' = 3, m_{F'} = 0\rangle$ (purple) states. The dashed line represents the trap laser wavelength used in the experiment.

where I is the intensity of the dipole trap laser. The $(-1)^{2(2F'+J+I_n+m_F)}$ drops out due to the fact that $2 \times (2F' + J + I_n + m_F)$ is always an even number. Again, the summation is carried over all dipole allowed transitions from the $|F, m_F\rangle$ state.

Figure 2 is the Grotrian diagram showing the major dipole-allowed transitions for calculating the light shifts of the $5S_{1/2}, |F = 2, m_F\rangle$ and the $5P_{3/2}, |F' = 3, m_{F'}\rangle$ states [97–105]. Table 1 is a list of transitions with respective wavelength and the electric dipole moments used for our calculation.

The $5S_{1/2}$, $|F = 2, m_F = 0\rangle$ and the $5P_{3/2}$, $|F' = 3, m_{F'} = 0\rangle$ states shifts in mK units as a function of trap laser wavelength are plotted in Figure 3. The dipole trap laser used in the experiment has a wavelength at 1064 nm, which is labeled with dashed line in the figure. At this wavelength, the $5S_{1/2}$, $|F = 2, m_F = 0\rangle$ ground state is lowered and defines the trapping potential whereas the $5P_{3/2}$, $|F' = 3, m_{F'} = 0\rangle$ excited state is shifted upward. For a trapping potential on the order of mK, the $5S_{1/2}$, $|F = 2, m_F\rangle \rightarrow 5P_{3/2}$, $|F' = 3, m_{F'}\rangle$ transition is blue-detuned with respect to

Table 1: Transitions used for light shifts calculation, the corresponding wavelength in vacuum λ and the electric dipole moment d=$\langle n, L, J \| e\vec{r} \| n', L', J' \rangle$.

Transition	λ (Å)[a]	d (ea_0)
$5S_{1/2} - 5P_{1/2}$	7949.8	2.99[a]
$5S_{1/2} - 5P_{3/2}$	7802.4	4.23[a]
$5S_{1/2} - 6P_{1/2}$	4216.7	0.24[a]
$5S_{1/2} - 6P_{3/2}$	4203.0	0.36[a]
$5S_{1/2} - 7P_{1/2}$	3592.6	0.08[a]
$5S_{1/2} - 7P_{3/2}$	7588.1	0.13[a]
$5P_{3/2} - 6S_{1/2}$	13668.8	3.02[b]
$5P_{3/2} - 7S_{1/2}$	7410.2	0.67[b]
$5P_{3/2} - 8S_{1/2}$	6161.3	0.35[b]
$5P_{3/2} - 4D_{3/2}$	15292.6	1.81[b]
$5P_{3/2} - 4D_{5/2}$	15293.7	5.44[b]
$5P_{3/2} - 5D_{3/2}$	7761.6	0.33[b]
$5P_{3/2} - 5D_{5/2}$	7759.8	0.99[b]
$5P_{3/2} - 6D_{3/2}$	6301.0	0.28[a]
$5P_{3/2} - 6D_{5/2}$	6300.1	0.83[a]

[a] Ref. [76]
[b] Ref. [98]

the bare atomic resonance by tens of MHz. Note that 1 mK is equivalent to 20.8 MHz (2.837×10^{10}Hz/K).

Figure 4 shows the AC-Stark shifts for each Zeeman levels of the $5S_{1/2}$, $|F = 2, m_F\rangle$ and the $5P_{3/2}$, $|F' = 3, m_{F'}\rangle$ states for typical trapping conditions in our experiment. The ground states are lowered nearly homogeneously (differences within 100 kHz), indicating that atoms in different m_F ground states experience the same trapping potential. On the other hand, the excited states shifts are state dependent to first order, which breaks the degeneracy of the levels. In this case, the excited states energy levels are symmetric with respect to the $m_{F'} = 0$ state and the energy difference is quadratic in $m_{F'}$. A more detailed and generalized discussion on the $m_{F'}$ dependence light shifts in terms of scalar, vector, and tensor polarizabilities will be introduced in the later section.

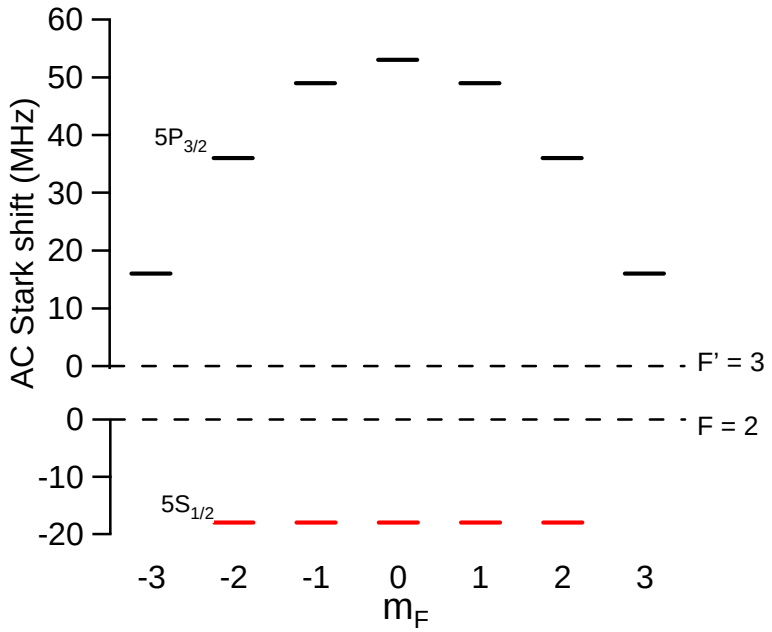

Figure 4: AC-Stark shifts for the $5S_{1/2}$, $|F=2, m_F\rangle$ and the $5P_{3/2}$, $|F'=3, m_{F'}\rangle$ states in optical dipole trap linearly polarized along the quantization axis. The intensity of the dipole trap laser is 5.7×10^9 W/m^2. The resulting ground states shifts are -18 MHz which correspond to a trapping potential of 0.88 mK.

2.6 Generalized Polarizability Approach

In this section, a generalized theory of the second order light shift with arbitrary trap laser propagation direction and polarization will be introduced. This approach is particularly useful in identifying the "magic wavelength" and other trap beam conditions that create identical light shifts for the ground and excited state [75, 76], which has great importance for the atomic clocks based on optical transitions with optically trapped atoms [79].

To begin with, let us rewrite the second order light shift in Eq. 2.29 with the explicit form of $V_{\pm}(\vec{r})$ as shown in Eq. 2.30,

$$\begin{aligned}\Delta_n &= \frac{E_0^2}{4}\sum_l \Big\{ \frac{|\langle n|\,\hat{\boldsymbol{\epsilon}}^*\cdot\boldsymbol{\mu}\,|l\rangle|^2}{E_n - E_l + \hbar\omega} + \frac{|\langle n|\,\hat{\boldsymbol{\epsilon}}\cdot\boldsymbol{\mu}\,|l\rangle|^2}{E_n - E_l - \hbar\omega} \Big\} \\ &= \frac{E_0^2}{4}\sum_l \langle n| \Big\{ \frac{(\hat{\boldsymbol{\epsilon}}\cdot\boldsymbol{\mu})^\dagger\,|l\rangle\,\langle l|\,(\hat{\boldsymbol{\epsilon}}\cdot\boldsymbol{\mu})}{E_n - E_l + \hbar\omega} + \frac{(\hat{\boldsymbol{\epsilon}}\cdot\boldsymbol{\mu})\,|l\rangle\,\langle l|\,(\hat{\boldsymbol{\epsilon}}\cdot\boldsymbol{\mu})^\dagger}{E_n - E_l - \hbar\omega} \Big\} |n\rangle \end{aligned} \tag{2.41}$$

By defining the resolvent operator $\hat{R}_{E_n}$ with $\hat{H}_0$ being the Hamiltonian of the unperturbed atom [92, 106]

$$\hat{R}_{E_n}(\omega) \equiv \sum_l \frac{|l\rangle \langle l|}{E_n - E_l + \hbar\omega} = \sum_l \frac{1}{E_n - \hat{H}_0 + \hbar\omega}, \tag{2.42}$$

the second order light shift can be written as,

$$\begin{aligned}\Delta_n &= \frac{E_0^2}{4} \langle n| \left\{ (\hat{\boldsymbol{\epsilon}}\cdot\boldsymbol{\mu})^\dagger \hat{R}_{E_n}(\omega)(\hat{\boldsymbol{\epsilon}}\cdot\boldsymbol{\mu}) + (\hat{\boldsymbol{\epsilon}}\cdot\boldsymbol{\mu})\hat{R}_{E_n}(-\omega)(\hat{\boldsymbol{\epsilon}}\cdot\boldsymbol{\mu})^\dagger \right\} |n\rangle \\ &\equiv \frac{E_0^2}{4} \langle n| \hat{O}(\omega) |n\rangle . \end{aligned} \tag{2.43}$$

Note that $\hat{\boldsymbol{\epsilon}}$ and $\boldsymbol{\mu}$ are irreducible rank-one spherical tensors, and they commute with each other as well as with the scalar operator $\hat{R}_{E_n}$. Hence the operator $\hat{O}$ can be reordered and written as the sum of irreducible tensor products of rank-κ [92, 107, 108],

$$\begin{aligned}\hat{O} =& \sum_{\kappa=0}^{2} \Big\{ (-1)^\kappa (\hat{\boldsymbol{\epsilon}}^* \otimes \hat{\boldsymbol{\epsilon}})^{(\kappa)} \cdot (\boldsymbol{\mu} \otimes R_{E_n}(\omega)\boldsymbol{\mu})^{(\kappa)} \\ &+ (\hat{\boldsymbol{\epsilon}}^* \otimes \hat{\boldsymbol{\epsilon}})^{(\kappa)} \cdot (\boldsymbol{\mu} \otimes R_{E_n}(-\omega)\boldsymbol{\mu})^{(\kappa)} \Big\} \\ =& \sum_{\kappa=0}^{2} \sum_q (-1)^q (\hat{\boldsymbol{\epsilon}}^* \otimes \hat{\boldsymbol{\epsilon}})^\kappa_{-q} \\ &\Big\{ (-1)^\kappa (\boldsymbol{\mu} \otimes R_{E_n}(\omega)\boldsymbol{\mu})^\kappa_q + (\boldsymbol{\mu} \otimes R_{E_n}(-\omega)\boldsymbol{\mu})^\kappa_q \Big\}, \end{aligned} \tag{2.44}$$

where $(\cdots)^{(\kappa)}$ denotes spherical tensor of rank-κ and κ =0, 1, 2. Therefore, the light shift Δ_n can also be decomposed into the scalar ($\kappa = 0$), vector ($\kappa = 1$), and tensor ($\kappa = 2$) light shifts. The second equality holds by utilizing the following generalized tensor scalar product identity,

$$T^{(\kappa)} \cdot U^{(\kappa)} = \sum_q (-1)^q T^\kappa_q U^\kappa_{-q}. \tag{2.45}$$

By explicitly writing down the relevant quantum numbers of the atomic state $|n\rangle$

Eq. 2.43 can be expressed as,

$$\begin{aligned}\Delta_{F,m_F} =&\frac{E_0^2}{4}\langle F,m_F|\,\hat{O}(\omega)\,|F,m_F\rangle\\ =&\frac{E_0^2}{4}\sum_{\kappa=0}^{2}\sum_{q}(-1)^q(\hat{\boldsymbol{\epsilon}}^*\otimes\hat{\boldsymbol{\epsilon}})^{\kappa}_{-q}\\ &\langle F,m_F|\left\{(-1)^{\kappa}(\boldsymbol{\mu}\otimes R_{E_n}(\omega)\boldsymbol{\mu})^{\kappa}_q+(\boldsymbol{\mu}\otimes R_{E_n}(-\omega)\boldsymbol{\mu})^{\kappa}_q\right\}|F,m_F\rangle\,. \end{aligned}\tag{2.46}$$

The second equality holds because $(\hat{\boldsymbol{\epsilon}}^*\otimes\hat{\boldsymbol{\epsilon}})^{\kappa}_q$ is the spherical tensor operator of the trap laser and it does not act on the atomic states. By applying the Wigner-Eckart theorem to the matrix element $\langle F,m_F|\,\hat{O}(\omega)\,|F,m_F\rangle$ in Eq. 2.46, we get

$$\begin{aligned}&\langle F,m_F|\,\hat{O}(\omega)\,|F,m_F\rangle\\ =&\sum_{\kappa=0}^{2}\sum_{q}(-1)^{\kappa+q}(\hat{\boldsymbol{\epsilon}}^*\otimes\hat{\boldsymbol{\epsilon}})^{\kappa}_{-q}(-1)^{F-m_F}\sqrt{2F+1}\begin{pmatrix}F&\kappa&F\\-m_F&q&m_F\end{pmatrix}_{3j}\\ &\langle F\|\left\{(\boldsymbol{\mu}\otimes R_{E_n}(\omega)\boldsymbol{\mu})^{(\kappa)}+(-1)^{\kappa}(\boldsymbol{\mu}\otimes R_{E_n}(-\omega)\boldsymbol{\mu})^{(\kappa)}\right\}\|F\rangle. \end{aligned}\tag{2.47}$$

Note that the Wigner 3-j symbols in Eq. 2.47 are nonzero only if $q=0$ by the selection rule $-m_F+q+m_F=0$. The reduced polarizability is defined in the following way,

$$\begin{aligned}\alpha_F^{(\kappa)}(\omega)\equiv&\sqrt{2F+1}\langle F\|\left\{(\boldsymbol{\mu}\otimes R_{E_n}(\omega)\boldsymbol{\mu})^{(\kappa)}\right.\\ &\left.+(-1)^{\kappa}(\boldsymbol{\mu}\otimes R_{E_n}(-\omega)\boldsymbol{\mu})^{(\kappa)}\right\}\|F\rangle\\ =&\sqrt{2\kappa+1}\sqrt{2F+1}(-1)^{(2F+\kappa)}\\ &\sum_{F'}\begin{Bmatrix}F&\kappa&F\\1&F'&1\end{Bmatrix}_{6j}\langle F\|\boldsymbol{\mu}\|F'\rangle\langle F'\|\boldsymbol{\mu}\|F\rangle\\ &\left\{\frac{1}{E_F-E_{F'}+\hbar\omega}+(-1)^{\kappa}\frac{1}{E_F-E_{F'}-\hbar\omega}\right\}. \end{aligned}\tag{2.48}$$

The summation is carried over all dipole allowed transition from the $|F,m_F\rangle$ state. The light shift can now be expressed in terms of the reduced polarizability,

$$\Delta_{F,m_F}=\frac{E_0^2}{4}\sum_{\kappa=0}^{2}(-1)^{\kappa}(\hat{\boldsymbol{\epsilon}}^*\otimes\hat{\boldsymbol{\epsilon}})^{\kappa}_0(-1)^{F-m_F}\begin{pmatrix}F&\kappa&F\\-m_F&0&m_F\end{pmatrix}_{3j}\alpha_F^{(\kappa)}(\omega).\tag{2.49}$$

The rank-κ tensor products of the unit polarization vector can also be expressed explicitly [92, 107, 108],

$$
\begin{aligned}
(\hat{\boldsymbol{\epsilon}}^* \otimes \hat{\boldsymbol{\epsilon}})_0^0 &= -\frac{1}{\sqrt{3}}(\hat{\boldsymbol{\epsilon}}^* \cdot \hat{\boldsymbol{\epsilon}}) = -\frac{1}{\sqrt{3}}, \\
(\hat{\boldsymbol{\epsilon}}^* \otimes \hat{\boldsymbol{\epsilon}})_0^1 &= \frac{i}{\sqrt{2}}(\hat{\boldsymbol{\epsilon}}^* \times \hat{\boldsymbol{\epsilon}})_0 = \frac{i}{\sqrt{2}}(\hat{\boldsymbol{\epsilon}}^* \times \hat{\boldsymbol{\epsilon}}) \cdot \hat{\boldsymbol{r}}_0 = -\frac{1}{\sqrt{2}}\mathcal{P}\hat{\mathbf{k}} \cdot \hat{\boldsymbol{r}}_0, \\
(\hat{\boldsymbol{\epsilon}}^* \otimes \hat{\boldsymbol{\epsilon}})_0^2 &= \frac{1}{\sqrt{6}}\{3(\hat{\boldsymbol{\epsilon}}^* \cdot \hat{\boldsymbol{r}}_0)(\hat{\boldsymbol{\epsilon}} \cdot \hat{\boldsymbol{r}}_0) - (\hat{\boldsymbol{\epsilon}}^* \cdot \hat{\boldsymbol{\epsilon}})\} = \frac{1}{\sqrt{6}}\{3|\hat{\boldsymbol{\epsilon}} \cdot \hat{\boldsymbol{r}}_0|^2 - 1\}.
\end{aligned} \tag{2.50}
$$

We have used the identities of the unit polarization vector as shown in Eq. 2.32.

In the literature, the scalar $\alpha_F^s(\omega)$, vector $\alpha_F^v(\omega)$, and tensor $\alpha_F^t(\omega)$ polarizabilities are used instead of the reduced polarizabilities [76, 106, 109]. They are related to the reduced polarizabilites by

$$
\begin{aligned}
\alpha_F^s(\omega) &= \frac{1}{\sqrt{3(2F+1)}}\alpha_F^{(0)}(\omega), \\
\alpha_F^v(\omega) &= -\frac{2F}{\sqrt{(F+1)(2F+1)}}\alpha_F^{(1)}(\omega), \\
\alpha_F^t(\omega) &= -\frac{2F(2F-1)}{\sqrt{3(2F+3)(F+1)(2F+1)}}\alpha_F^{(2)}(\omega)
\end{aligned} \tag{2.51}
$$

By evaluating and using the explicit form of the Wigner-3j symbols in Eq. 2.49 [110, 111], the second order light shift can be expressed in terms of $\alpha_F^s(\omega)$, $\alpha_F^v(\omega)$, and $\alpha_F^t(\omega)$

$$
\begin{aligned}
\Delta_{F,m_F} = -\frac{E_0^2}{4}\big\{&\alpha_F^s(\omega) + \alpha_F^v(\omega)\frac{m_F}{2F}\mathcal{P}\hat{\mathbf{k}} \cdot \hat{\boldsymbol{r}}_0 \\
&+ \alpha_F^t(\omega)\frac{3|\hat{\boldsymbol{\epsilon}} \cdot \hat{\boldsymbol{r}}_0|^2 - 1}{2}\frac{3m_F^2 - F(F+1)}{F(2F-1)}\big\}.
\end{aligned} \tag{2.52}
$$

In the laboratory, the quantization axis is typically defined by a bias magnetic field along $\hat{\boldsymbol{r}}_0$. For the case considered in Section 2.5, the linearly polarized trap laser beam propagates perpendicular to the quantization axis, making the m_F linear dependent term (the term proportional to $\alpha_F^v(\omega)$) vanishes. The resulting light shifts for the $5P_{3/2}$ states are quadratic in m_F. Note that this remaining dependence on the

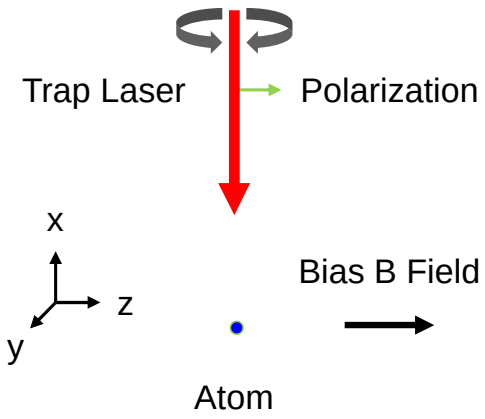

Figure 5: The quantization axis, trap laser polarization, and its propagation direction used in Section 2.5. In order to eliminate the state dependent excited states light shifts, rotate the trap laser polarization by 54.7° as shown by the gray arrows.

m_F state can be eliminated by satisfying :

$$3|\hat{\boldsymbol{\epsilon}} \cdot \hat{\boldsymbol{r}}_0|^2 - 1 = 0.$$

Therefore, we can eliminate the quadratic light shifts of the excited states by rotating the trap laser polarization 54.7° as shown in Figure 5 in either direction.

2.7 Temperature Measurements of Single Atoms in The Dipole Traps

Fluorescent detection of optically trapped individual atoms usually heats up the atoms and is responsible for loss of atoms from the trap. Therefore, it is important to measure the temperature of the atoms and quantify the heating induced by the detection process. The standard technique for measuring the temperature of ultracold neutral atoms is to measure the expansion rate of a cloud of atoms released from the trap. This so-called time-of-flight technique compares the spatial density profile of the atomic cloud to that obtained from a classical Maxwell-Boltzmann distribution of the atom velocity (at least for thermal atoms well above quantum degeneracy). This method works well on samples with large numbers of atoms, where it is easy to obtain the velocity distribution of the cloud from a single image. For small clouds

and single atoms, the same technique can work in principle, but in practice it is often impractical to achieve enough signal-to-noise in the images to obtain the distribution.

In 2008, Tuchendler *et al.* demonstrated that the energy distribution of single atoms in optical dipole traps could be successfully measured using the drop and recapture technique [112] originally used in the first optical molasses experiments [68]. In this technique, the trap is quickly pulsed off for a short amount of time, and the fraction of atoms that are recaptured is measured as a function of the time that the trap was off. Upon turning the trap back on, the atom will be recaptured if the sum of the kinetic energy and the potential energy at the final position due to the optical dipole trap is less than zero. For a given trap off time, atoms at higher temperature will be less likely to be recaptured. On the other hand, the recapture probability will fall monotonically with increasing trap off time for atoms at a given temperature. In order to extract a temperature of the atoms, it is necessary to compare the measurements to numerical simulations. Below, we discuss the simulations we performed.

In the simulations, the initial kinetic energy of the atom at the bottom of the trap is randomly generated according to the Maxwell-Boltzmann distribution of a certain temperature T. A random unit vector is assigned to each atom to determine the direction of motion after the trap is switched off for an amount of time t. The motion of the atom is determined by numerical integration of the classical equations using the initial velocity $v = (v_x, v_y, v_z)$ and the small effects of gravity. When the trap is turned back on, the atom will be recaptured if the total energy is less than zero and the counter of recapture events will be increased by one. The above process is repeated 10^5 times at each trap off time and the accumulated recapture rate is plotted with 1 μs increments of the trap off time. Finally, the experimental data are fitted to the simulation curves with 5 μK increments.

Figure 6 shows the results of the Monte-Carlo simulation for single atoms in a

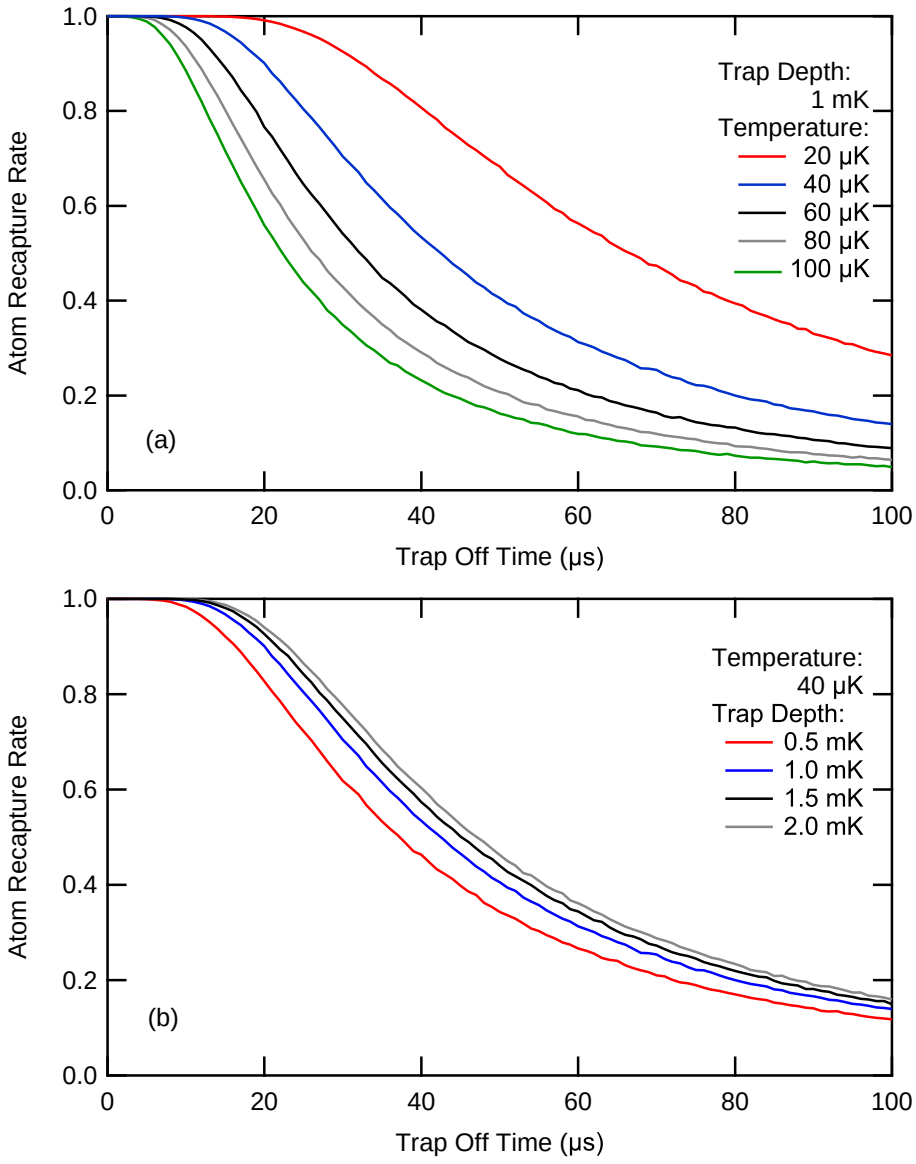

Figure 6: (a) A plot for atom recapture rate vs trap off time in a 1 mK single focus trap with various temperature. (b) Atom recapture rate vs trap off time with 40 μK temperature in various trapping potential.

1064 nm single focus trap with 2.5 μm minimum waist. The simulation is done with Mathematica, and the time it takes is linearly dependent to the number of total trials. For the results presented in this figure, there are 10^5 trials at each of the 101 trap off times and it takes 500 seconds to complete each curve. The fluctuation of the recapture rates can be reduced by increasing the number of trials at each point, which also increases the total simulation time. It is seen from the figure that the temperature of the atom has a greater effect on recapture probability than the trapping potential. In the experiment, we can determine the trap depth to within 10% by the trap frequency measurements; therefore, the atom temperature obtained by this method should be accurate within ± 5 μK.

Although the above discussion is based on single atoms in single focus traps, this method works for any number of atoms in any type of trap. The particular advantage for our application is that it is easier to measure one atom in a trap than to measure the location of one free-falling atom. The disadvantage is that this method is indirect and relies on comparison to the results of simulations. We will also apply this method to low numbers of atoms in 1D optical lattice. Instead of counting the single atom successful recapture events, fluorescent images of the atoms have to be taken before and after switching off the trap to determine the atom recapture rate. Figure 7 shows the results of the simulation for atoms in a 1064 nm 1D optical lattice with a 13 μm minimum waist. The insets show the recapture rates with trap off time less than 20 μs, showing fast decays in the first 5 μs. This is caused by the high asymmetry of the trap geometry, quantified by the trap frequencies in the radial and axial direction. A qualitative approach is to compare the spatial confinements in each axis. In the radial direction, the confinement is characterized by the minimum trap beam diameter (26 μm). On the other hand, the confinement in the longitudinal direction of a 1D optical lattice is defined by the half wavelength of the trap laser, which is 0.532 μm. The dramatic difference between the confinements in these two directions makes it much

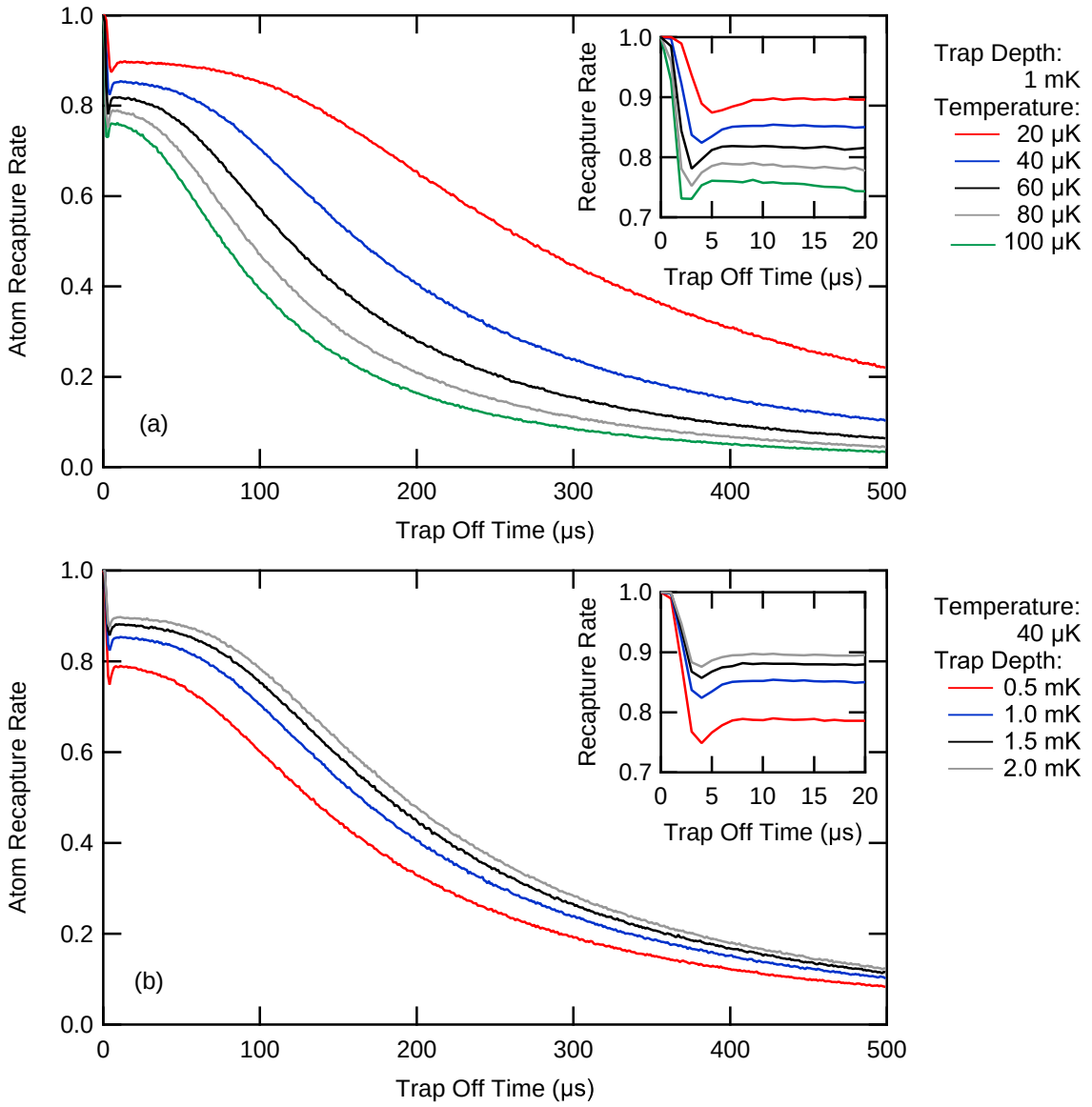

Figure 7: (a) A plot for atom recapture rate vs trap off time in a 1 mK 1D optical lattice with various temperature. (b) Atom recapture rate vs trap off time with 40 μK temperature in various trapping potential.

easier for the atom to escape from the longitudinal direction. For comparison, the spatial confinements of the single focus trap is the minimum beam diameter (5.0 μm) in the radial direction and the Rayleigh length ($\pi {w_0}^2/\lambda = 13$ μm) in the longitudinal direction.

2.8 Linewidth Broadening Induced by Spatial Varying Light Shifts

The large AC-Stark shifts in optical dipole traps, together with the thermal motion of the atoms in the confining potential can lead to significant broadening of the optical transitions. These need to be considered in addition to the usual transition linewidth broadening mechanisms including power broadening and Doppler broadening. Detailed discussions on these latter topics can be found in [113–115]. Power broadening becomes noticeable when the probe laser intensity is comparable to the saturation intensity of the transition. Doppler broadening stems from the Doppler effect of the thermal motion of the atoms, which is given by [115]

$$\nu_{FWHM} = \sqrt{\frac{8k_B T \ln 2}{mc^2}}\nu_0, \tag{2.53}$$

For laser cooled atoms at $\sim$100 μK, the Doppler broadening of the ^{87}Rb D_2 transition is on the order of 300 kHz, which is much smaller than the natural linewidth $\gamma = 6.07$ MHz and can be ignored in our experiment. In the remainder of this section, we will discuss transition linewidth broadening originating from the thermal motion of the trapped atoms with spatial dependent light shift and estimate the order of magnitude of this broadening.

Figure 8 shows the spatial profile of the light shifts for the ground and excited states in general. The horizontal red line represents the average energy of the atoms interacting with a thermal reservoir at temperature T, which characterizes the motion of the trapped atoms as well as the distance an atom can travel from the center of the trap. It is readily seen that the induced light shift of the ^{87}Rb D_2 transition depends

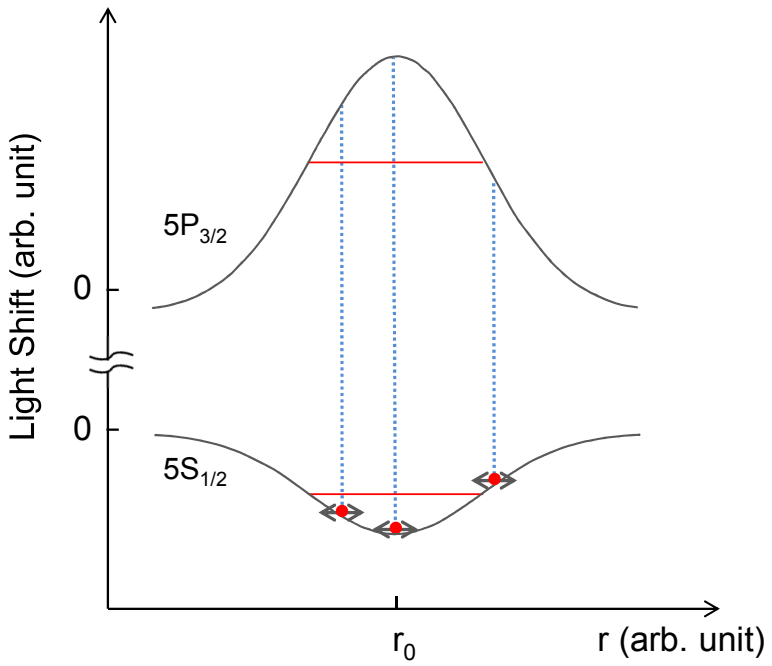

Figure 8: Dipole trap induced light shifts of the ground and excited states as a function of radial distance from the center of the trap. The red dots represent atoms in the optical dipole trap and the blue dotted line shows the light shifts of the ^{87}Rb D_2 transition at the position of the atoms.

on the position of the atom. As the atom moves away from the center of the trap, the light shift becomes smaller. The thermal motion of the atom in the trap will explore different light shifts of the transition, which will lead to a broadening of the transition determined by the motional energy distribution of the trapped atom.

To quantify this broadening, consider the Maxwell-Boltzmann distribution function of the energy,

$$f(E) = 2\sqrt{\frac{E}{\pi}}(k_B T)^{-3/2}\exp\Big(\frac{-E}{k_B T}\Big). \tag{2.54}$$

The full width half max (FWHM) of this distribution function can be obtained numerically [116],

$$f(E)_{FWHM} \simeq 2.02 \times k_B T. \tag{2.55}$$

The linewidth of the thermal atoms in the dipole optical trap becomes linearly dependent to the temperature of the atoms. Figure 4 shows that for the $|F = 2, m_F = 0\rangle$

to $|F' = 3, m_{F'} = 0\rangle$ transition, the conversion between light shift and trapping potential is $\sim$71 MHz/880 μK. Therefore, for typical laser-cooled atoms at 100 μK, the FWHM of the energy distribution is $k_B \times 202$ μK, which corresponds to a linewidth broadening of 16 MHz.

CHAPTER III

CAVITY QED WITH ^{87}RB

The interaction between light and matter is responsible for all large-scale phenomena that we see every day. While the interaction between large number of photons and atoms is easy to observe, the interaction between an isolated single photon and single atom cannot be detected easily. This is due to the small interaction probability between an atom and a single photon combined with the low detection efficiency of a single photon emitted by an atom in free space. Placing an atom in an optical cavity enhances the interaction compared to the bare atom and provides a directed output signal for increased detection efficiency [45].

In this chapter, we will provide an theory overview of cavity quantum electrodynamics and introduce the relevant parameters of a atom-cavity system, as they have been extensively discussed in [117–119]. The Jaynes-Cummings model will also be introduced to illustrate the atom-cavity system. Finally, numerical calculations of the quantum mechanical and the semi-classical model with more than one atom are compared for the purpose of using the semi-classical model in systems with twenty atoms or so. The results will be applied to simulate the cavity field dynamics presented in Chapter 6.

3.1 Cavity QED Parameters

For most purposes, an atom-cavity system can be characterized by three parameters: the atom-cavity coupling rate g, the cavity loss rate κ, and the atom decay rate $\gamma_\perp$. They are responsible for three distinctive processes as shown in Figure 9. The cavity loss rate represents the rate that a cavity photon is removed from the system, either through transmission or absorption. The atom-cavity coupling rate represents

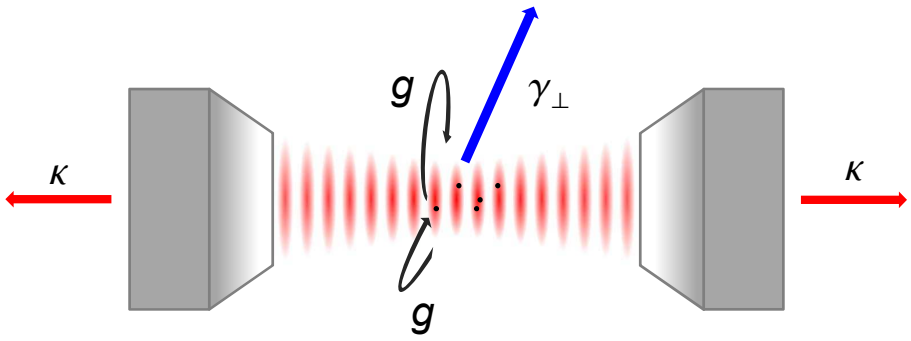

Figure 9: The three process characterized by the cavity loss rate κ, the atom-cavity coupling rate g, and the atom decay rate $\gamma_\perp$. The black dots represent the atoms and the red ellipses represent the wave envelopes of the cavity field standing wave.

the rate at which an atom in the excited state emits a photon into the cavity mode through stimulated emission or an atom in the ground state absorbs a photon in the cavity mode. Finally, the atom decay rate $\gamma_\perp$ represents the rate that the atom emits a photon into the mode other that the cavity mode. In the following sections, we will discuss these processes in more details.

3.1.1 Cavity Loss Rate

An optical cavity is constructed with two mirrors with high reflectivity. The finesse of the cavity $\mathcal{F}$ is defined as,

$$\mathcal{F} = \frac{2\pi}{losses}, \tag{3.1}$$

where *losses* is the total transmission and absorption losses from both cavity mirrors. For example, if each mirror has transmission of 10 ppm and absorption of 20 ppm, the total losses is 60 ppm.

The free spectral range ν_{FSR}, the frequency spacing between adjacent longitudinal modes, is given by

$$\nu_{FSR} = \frac{c}{2L}, \tag{3.2}$$

where c is the speed of light and L is the length of the cavity.

The cavity loss rate κ is related to the finesse and the free spectral range by,

$$\kappa = \frac{\nu_{FSR}}{2\mathcal{F}}. \tag{3.3}$$

The cavity mirrors that we use in the experiment have the same radius of curvature (R = 2.5 cm), a total transmission loss of 108 parts per million (ppm), and the cavity length is 0.5 mm. Considering only the transmission loss, the finesse of our cavity and the cavity loss rate is

$$\begin{aligned} \mathcal{F} &= 58000 \\ \frac{\kappa}{2\pi} &= 5.2 \text{ MHz}. \end{aligned}$$

3.1.2 Atom-Cavity Coupling Rate

For an atom in the cavity mode, g is the cavity enhanced stimulated photon emission rate into the cavity mode. It is proportional to the electric field $\mathbf{E}(\vec{r})$ at the position of the atom, which is defined as [44]

$$g(\vec{r}) \equiv g_0\psi(\vec{r}) = \frac{\boldsymbol{\mu} \cdot \mathbf{E}(\vec{r})}{\hbar}, \tag{3.4}$$

where g_0 is the maximum atom-cavity coupling rate, $\boldsymbol{\mu}$ is the transition dipole moment and $\psi(\vec{r})$ is the spatially dependent part of the TEM_{00} mode of the electric field ($\psi(\vec{r}) \leq 1$).

$$\psi(\vec{r}) = \cos(kx)\exp\Big(-\frac{x^2+y^2}{{w_0}^2}\Big), \tag{3.5}$$

w_0 is the minimum waist of the cavity mode.

The magnitude of the electric field can be obtained by considering the energy of a single photon in the cavity as the integral of energy of electro-magnetic field over the cavity,

$$\hbar\omega = \int \Big(\frac{\epsilon_0}{2}\left|\mathbf{E}(\vec{r})\right|^2 + \frac{1}{2\mu_0}\left|\mathbf{B}(\vec{r})\right|^2\Big)d^3\vec{r} = \int \epsilon_0 \left|\mathbf{E}(\vec{r})\right|^2 d^3\vec{r} = 2\epsilon_0 E_0 V_M, \tag{3.6}$$

The mode volume V_M of the electric field can be expressed as,

$$V_M = \int |\psi(\vec{r})|^2 \, d^3\vec{r} = \frac{\pi}{4} {w_0}^2 L, \tag{3.7}$$

The atom-cavity coupling rate g_0 can be expressed as,

$$g_0 = |\boldsymbol{\mu}| \sqrt{\frac{\omega}{2\epsilon_0 \hbar V_M}}. \tag{3.8}$$

For our experiment, $|\boldsymbol{\mu}| = 2.53{\times}10^{-29}$ C·m [95] and $\frac{g_0}{2\pi} = 9.3$ MHz.

3.1.3 Atom Decay Rate

The natural decay rate γ of the ^{87}Rb from the $5P_{3/2}$ state to the $5S_{1/2}$ state in free space is (2π) 6.07 MHz [95]. The excited state life time of the atom τ is related to the decay rate by $\tau = \gamma^{-1} = 26$ ns.

For an atom in the cavity system, the relevant quantity is $\gamma_\perp$, the atomic dipole decay rate into modes other than the cavity mode [120]. When the atomic decay is solely radiative, $\gamma_\parallel = 2\gamma_\perp = \gamma$. $\gamma_\parallel$ is the decay rate of atomic inversion and the last equality holds because the solid angle subtended by the cavity mode is small ($\sim 10^{-5}$).

3.1.4 Other Derived Quantities

There are three quantities derived from κ, g_0, and $\gamma_\perp$ that can be used to characterize a atom-cavity system. The saturation photon number n_0, the critical atom number N_0, and the single atom cooperativity C_1 [44, 121],

$$n_0 \equiv \frac{\gamma_\perp \gamma_\parallel}{4{g_0}^2} = \frac{{\gamma_\perp}^2}{8{g_0}^2} \tag{3.9}$$

$$N_0 \equiv \frac{2\gamma_\perp \kappa}{{g_0}^2} \equiv {C_1}^{-1}. \tag{3.10}$$

The single atom cooperativity is used to quantify the coupling strength between the atom and the cavity photons. When $C_1 \gg 1$, the system is in strong coupling regime, $C_1 \sim 1$ corresponds to intermediate coupling regime, and $C_1 \ll 1$ is weak coupling regime. For our experiment, $n_0 = 0.013$, $N_0 = 0.36$, and $C_1 = 2.8$.

3.2 Single Atom Cavity QED

The interaction between a two-level atom (excited state: $|e\rangle$, ground state: $|g\rangle$) and a single mode of electromagnetic field containing n photons $|n\rangle$ can be described by Jaynes-Cummings model. The Hamiltonian of this system can be written as

$$H = \frac{1}{2}\hbar\omega_0\hat{\sigma}_z + \hbar\omega_c\hat{a}^\dagger\hat{a} + \hbar g_0(\hat{\sigma}_+\hat{a} + \hat{\sigma}_-\hat{a}^\dagger), \tag{3.11}$$

where ω_0 is the resonant frequency of the atomic transition, ω_c is the frequency of the cavity, $\hat{\sigma}_z = |e\rangle\langle e| - |g\rangle\langle g|$ is the atomic inversion operator for this two level atom, $\hat{\sigma}_+$ and $\hat{\sigma}_-$ are the raising and lowering operator for the atom, $\hat{a}^\dagger$ and $\hat{a}$ are the creation and annihilation operator for the cavity photons. An atom-cavity system with n cavity photons can be solved exactly [46]. With the cavity frequency tuned to the atom resonant frequency, the eigenvalues are

$$\begin{aligned} E_{n+} &= \hbar n\omega + \sqrt{n}\hbar g_0 \\ E_{n-} &= \hbar n\omega - \sqrt{n}\hbar g_0, \end{aligned} \tag{3.12}$$

and the corresponding eigenstates are

$$\begin{aligned} |\phi_{n+}\rangle &= \frac{1}{\sqrt{2}}(|n-1, e\rangle + |n, g\rangle) \\ |\phi_{n-}\rangle &= \frac{1}{\sqrt{2}}(|n-1, e\rangle - |n, g\rangle). \end{aligned} \tag{3.13}$$

Figure 10 shows the energy diagram of a bare atom, cavity photon Fock state, and a atom-cavity system, respectively.

The above discussion has neglected the natural decay of the atoms from the excited state as well as the dissipation of cavity photons from the system. To incorporate these effects, we can use a Master equation to solve for the time evolution of the system, and the observables can be obtained by taking the expectation values of the collapse operators. To understand how it works, we'll go through the single-atom-cavity problem again, now with atomic relaxation and cavity dissipation.

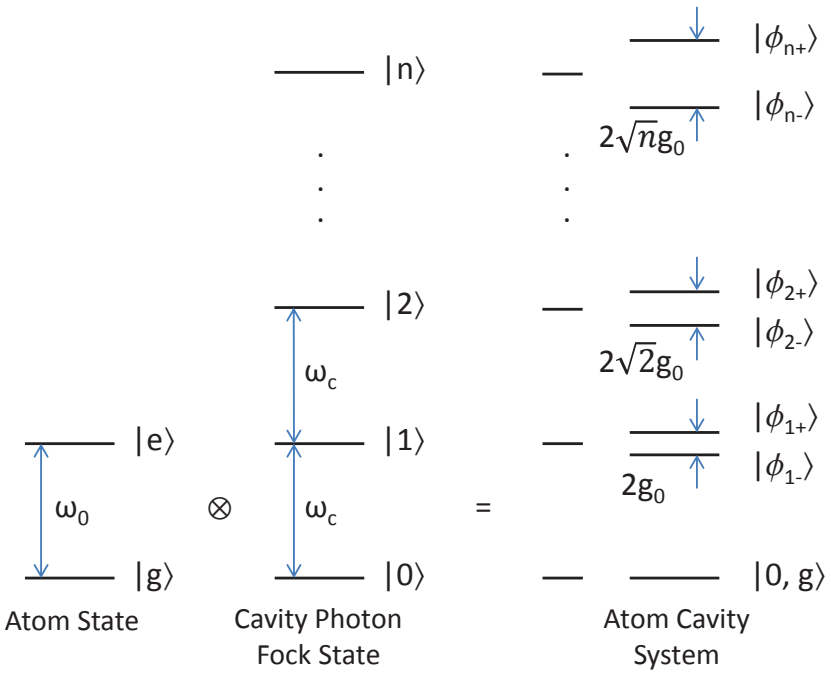

Figure 10: Energy diagram of a bare atom, cavity photon Fock state, and a atom-cavity system. The atomic transition frequency is ω_0, the cavity frequency ω_c is tuned resonant to the atomic transition. In the atom-cavity system, the splitting between the new eigenstates is $2\sqrt{n}g_0$.

In the interaction picture, the Hamiltonian of the system with an atom driven by an external laser from the side can be expressed as

$$H = (\omega_0 - \omega_L)\hat{\sigma}_+\hat{\sigma}_- + (\omega_c - \omega_L)\hat{a}^\dagger\hat{a} + ig_0(\hat{\sigma}_-\hat{a}^\dagger - \hat{\sigma}_+\hat{a}) + \Omega(\hat{\sigma}_+ + \hat{\sigma}_-), \qquad (3.14)$$

where ω_L is the frequency of the external probing laser, Ω is the Rabi frequency of the probe laser. For simplicity, $\hbar$ is omitted in this expression. From Eq. 3.14 it can be seen that the frequency difference is important, not the absolute frequency. To make it easier for comparing these parameters as those used in the experiment, we will use the resonant frequency of the bare atom ω_r as reference. $\Delta_0 \equiv \omega_0 - \omega_r$ will be the atom frequency shift (due to AC-Stark shift), $\Delta_L \equiv \omega_L - \omega_r$ will be the laser frequency detuning, and $\Delta_c \equiv \omega_c - \omega_r$ will be the cavity frequency detuning from the bare atomic resonant frequency, respectively. The Liouville equation of the density

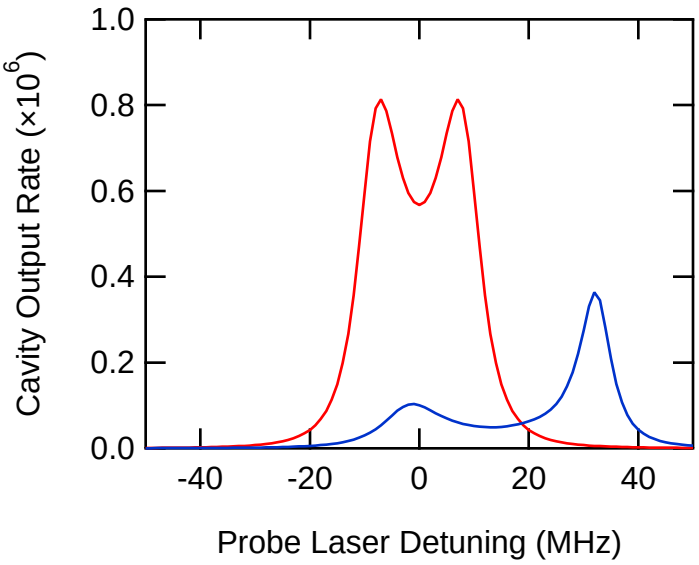

Figure 11: Cavity photon output rate of a single-atom-cavity system driven by an external laser from the side. The cavity QED parameters of the system are $\frac{1}{2\pi}(g_0, \kappa, \gamma_\perp) = (9.3, 7.0, 3.0)$ MHz. The Rabi frequency of the external probe laser is 2.1 MHz and the cavity frequency detuning is 0. The red curve represents an atom experience no AC-Stark shift, the blue curve represents an atom in the optical dipole trap that shifts the atomic resonance 30 MHz to the blue.

matrix ρ takes the following form [42, 43],

$$\dot{\rho} = \hat{\mathcal{L}}\rho = -i[\hat{H}, \rho] + \sum_{k=1}^{2}(\hat{C}_k\rho\hat{C}_k^\dagger - \frac{1}{2}\hat{C}_k^\dagger\hat{C}_k\rho - \frac{1}{2}\rho\hat{C}_k^\dagger\hat{C}_k), \tag{3.15}$$

$\hat{C}_1 = \sqrt{2\kappa}\hat{a}$ and $\hat{C}_2 = \sqrt{\gamma_\perp}\hat{\sigma}_-$ are the collapse operators for the cavity photons and the atom, respectively.

When the system reaches steady state ρ_s, the above equation becomes,

$$\hat{\mathcal{L}}\rho\Big|_{\rho=\rho_s} = 0. \tag{3.16}$$

For weak excitation, the steady state density matrix ρ_s can be solved by truncating the Hilbert space assuming a maximum cavity occupation number of $5 \sim 10$ photons and diagonalizing the matrix numerically [122, 123]. The cavity output spectrum can be obtained by taking the expectation value of the of $\hat{C}_1$ of the steady state density matrix.

Figure 11 shows the spectrum of a single atom in the cavity driven by an external

laser from the side. For a bare atom that experiences no light shift, the spectrum is represented by the red curve, which is symmetric and the vacuum Rabi splitting has a magnitude of $2g_0$. The blue curve shows an atom in the optical dipole trap with +30 MHz of AC-Stark shift of the ground to excited state transition. The spectrum becomes asymmetric and has a much lower output signal level.

3.3 Many-Atom Cavity QED

In principle, it is straightforward to go from a single-atom-cavity system to a multi-atom-cavity system. For every additional atom added to the system, the corresponding terms of $\hat{\sigma}_+$ and $\hat{\sigma}_-$ are put into the Hamiltonian,

$$\begin{aligned} H &= (\Delta_0 - \Delta_L)\sum_j \hat{\sigma_j}_+\hat{\sigma_j}_- + (\Delta_c - \Delta_L)\hat{a}^\dagger\hat{a} \\ &+ ig_0\sum_j(\hat{\sigma_j}_-\hat{a}^\dagger - \hat{\sigma_j}_+\hat{a}) + \sum_j \Omega_j(\hat{\sigma}_+ + \hat{\sigma}_-). \end{aligned} \tag{3.17}$$

With a multi-atom-cavity system, it is possible to use the cavity-assisted interaction between these atoms for quantum information processing. For this purpose, coherent state control for the individual atoms in the cavity is desired and can be achieved by applying independent laser beams on the each atom from the side of the cavity.

In the experiment, we constructed a system with two independently controllable 1D optical lattices, each of them has its dedicated external probe laser. Hence the following discussion will be focused on a multi-atom-cavity system with two independently controlled ensembles.

To calculate the cavity output spectrum of a multi-atom-cavity system, we started with the same Matlab program "Computational Toolbox for Quantum Optics" [123] used in Section 3.2. Unfortunately, this program is not optimized to efficiently calculate a cavity system with many atoms. The calculation time and the required memory grow exponentially as the number of atoms in the system, which makes its impractical

to go beyond 5 atoms with current desktop PCs. In order to increase the maximum number of atoms we can simulate, a Monte-Carlo method is employed, as discussed in the next section.

3.3.1 Monte-Carlo Method for Multi-Atom Cavity QED System

For the Monte-Carlo method, we let the system evolve for a specific time instead of solving the steady state density matrix. Dissipation of the cavity photons comes from the randomly occurred quantum jumps during the system evolution. The result of the calculation is obtained by taking the expectation value of the corresponding operator and averaging over many randomly generated systems. The advantage of using the Monte-Carlo method over using the master equation to solve the steady state solution is that, the former stores the state of the system in the computer memory and the latter stores the entire density matrix. For an atom-cavity system with N atoms and N_{photon} cavity photons, the state vector of the system has a dimension of $2^N \times N_{photon}$ and the density matrix has a dimension of $2^{2N} \times N_{photon}^2$. Therefore, the Monte-Carlo method allows us to simulate a system with more atoms.

We use the "Quantum Toolbox in Python" (QuTiP) [124] to calculate the evolution of the system using the Monte-Carlo method. The documentation and the example scripts can be found in [125]. Using this method, there are two parameters to be considered independently, the number of systems to be averaged over n_{sample}, and the evolution time for each system t_{evo}. The bigger these two quantities are, the more precise the results of the simulation are for estimating the steady state solution. The time for calculation scales linearly as the product of n_{sample} and t_{evo}, hence it is important to empirically optimize these two quantities for low number of atoms before simulating systems with large number of atoms.

In Figure 12, we compare the spectrum of a single-atom-cavity system using

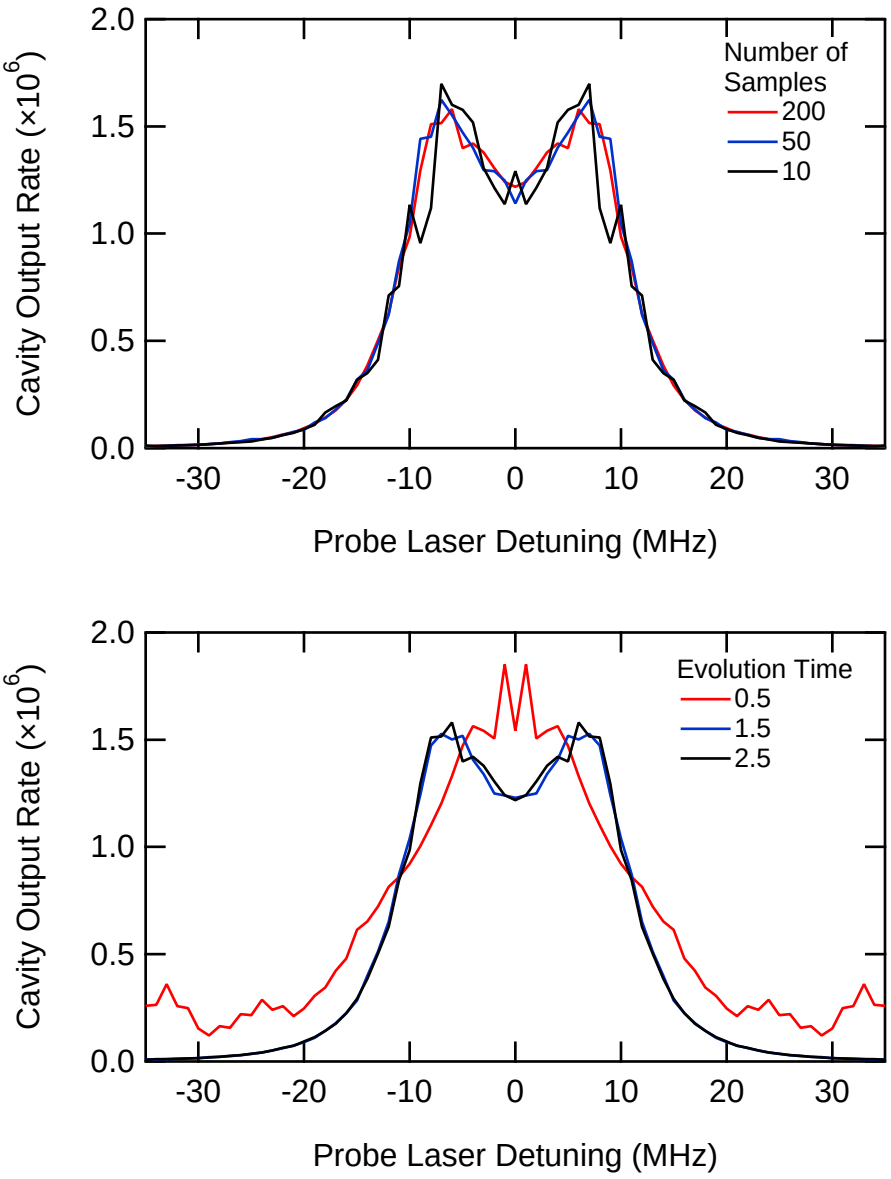

Figure 12: In the top figure, the evolution time is set to 2.5. In the bottom figure, the number of samples is set to 200. The cavity QED parameters in the Hamiltonian are expressed in the unit of MHz, hence the evolution time is in the unit of μs. The cavity QED parameters of the system are $\frac{1}{2\pi}(g_0, \kappa, \gamma_\perp) = (9.3, 7.0, 3.0)$ MHz. The Rabi frequency of the external probe laser is 3.4 MHz and the cavity frequency detuning is 0.

Monte-Carlo method with different n_{sample} and t_{evo}. For simplicity, we ignored AC-Stark shift, so the resulting spectrum is symmetric with respect to the probe laser detuning similar to the red curve shown in Figure 11. In Figure 12, we calculate the solution for positive probe detuning and generate the other half by symmetry argument.

In the top of Figure 12, we can see that averaging over 200 samples provides a reasonably smooth spectrum for $t_{evo} = 2.5$ μs. In the bottom of Figure 12, it is seen that the system at $t_{evo} = 0.5$ μs is still far from the steady state and the spectrum starts converging at $t_{evo} = 1.5$ μs, hence, we choose $t_{evo} = 2.5$ μs and $n_{sample} = 200$.

In Figure 13 we use the Monte-Carlo method with $n_{sample} = 200$ and $t_{evo} = 2.5$ μs to calculate the spectrum of a few multi-atom-cavity systems ((b) and (d)) and compare them with those obtained by the matrix diagonalization method described in Section 3.2 ((a) and (c)). In Figure 13(a) and 13(b), the system consists of a cavity and 1 (red curve), 2 (blue curve), 3 (black curve), 4 (gray curve) atoms all driven directly by the external probe laser. Again, the AC-Stark shift is ignored for simplicity at this point. The peak detuning of the spectrum scales roughly as $\sqrt{N}g_0$ and the peak height scales linearly as N where N is the total number of atoms in the system.

In Figure 13(c) and 13(d), the system is slightly different, only the first atom is directly driven by the external probe laser and the other atoms are indirectly driven by the cavity photons. The peak detuning of the spectrum also scales as $\sqrt{N}g_0$ and the peak height scales inversely as the N. The absorption of the cavity photons by the indirectly driven atoms gives rise to higher chance of losing the cavity photons through spontaneous emission, resulting in lower cavity output signal.

In both cases, the simulation results of the Monte-Carlo method agree well with the one that calculates the steady state density matrix. The question is, how far can we go within reasonable amount of time? For $N = 15$, $n_{sample} = 200$, and

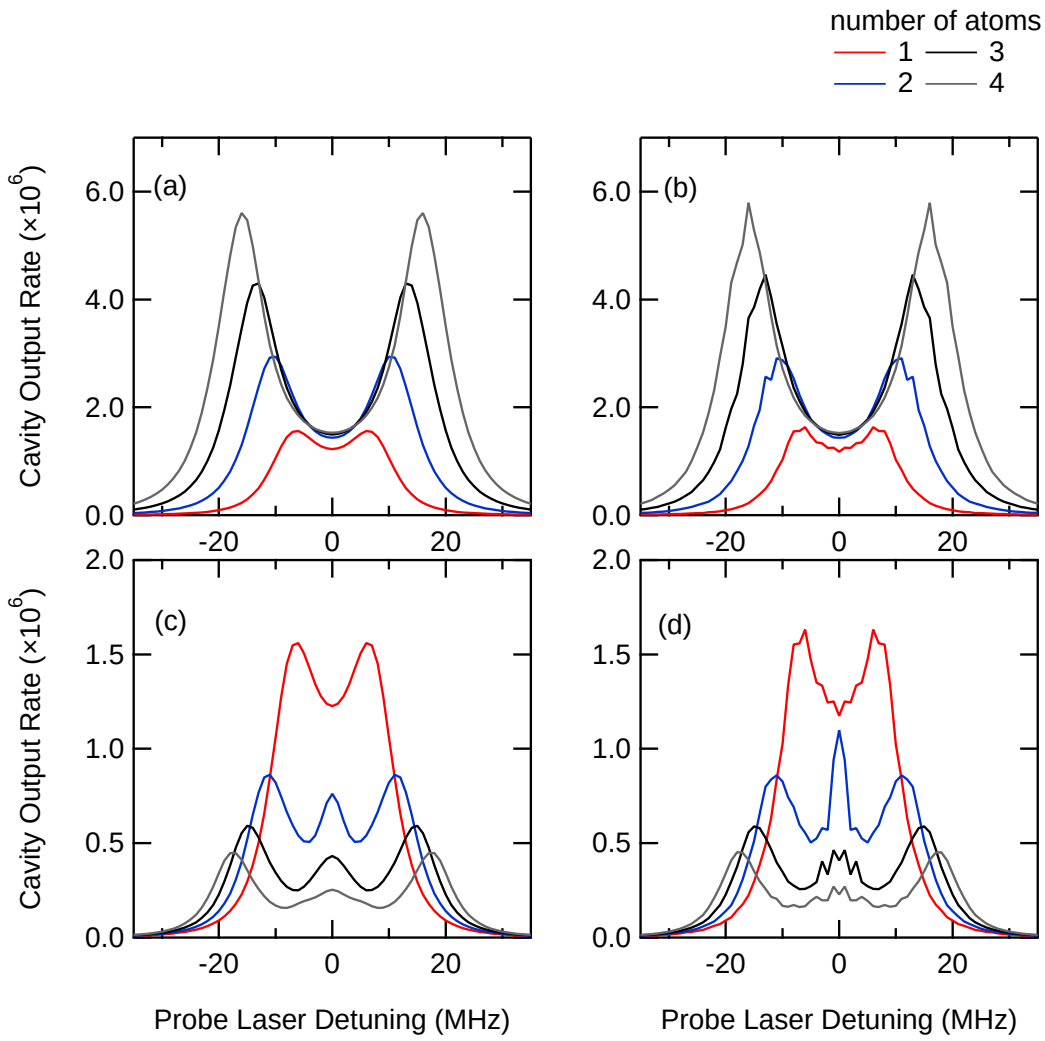

Figure 13: Comparison between the method used in Section 3.2 and the Monte-Carlo method. The cavity QED parameters of the system used in the calculation are $\frac{1}{2\pi}(g_0, \kappa, \gamma_\perp) = (9.3, 7.0, 3.0)$ MHz. The Rabi frequency of the external probe laser is 3.4 MHz and the cavity frequency detuning is 0. In (a) and (b), all atoms are directly driven by the external probe laser. Whereas in (c) and (d), only the first atom is directly driven by the external probe laser and the other atoms are excited by the cavity photons.

t_{evo} = 2.5 μs, it takes about 900 hours (>1 month) to finish the calculation for a spectrum with 30 points on a single processor. By using multi-core processors, the code can be written to calculate different part of the spectrum and executed simultaneously. By simultaneously running six simulations on two computers, the total time for completing the calculation for $N = 1$ to $N = 15$ can be reduced to two weeks. Though the total number of atoms is still less than what we have in the experiment (∼30), it still provides valuable insight and assists us to develop a semi-classical models for the system.

3.3.2 Semi-Classical Model for Multi-Atom Cavity QED

In this section, we construct a semi-classical Hamiltonian that fulfills the criteria set by the full quantum Hamiltonian at low number of atoms, and determine in what limit this semi-classical Hamiltonian yields spectra close to the correct one.

It was shown in the early works of the multi-atom-cavity systems that the atom-cavity interaction in a system with N atoms can be collectively enhanced by a factor of $\sqrt{N}$ [51, 121, 126, 127]. Figure 13 also indicates that the spectrum of a system with N atoms and atom-cavity coupling rate g_0 resembles the spectrum of a system with one atom and atom-cavity coupling rate $\sqrt{N}g_0$. Therefore, we will use $\sqrt{N}g_0$ as the atom-cavity coupling rate for the semi-classical Hamiltonian. The other criterion is that the peak height should scale roughly linearly as N. The scaling is reproduced by multiplying the external excitation by a factor of $\sqrt{N}$, and the semi-classical Hamiltonian takes the following form,

$$\begin{aligned} H_{sc} &= (\Delta_0 - \Delta_L)\hat{\sigma}_+\hat{\sigma}_- + (\Delta_c - \Delta_L)\hat{a}^\dagger\hat{a} \\ &+ i\sqrt{N}g_0(\hat{\sigma}_-\hat{a}^\dagger - \hat{\sigma}_+\hat{a}) + \sqrt{N}\Omega(\hat{\sigma}_+ + \hat{\sigma}_-). \end{aligned} \tag{3.18}$$

For a system with atoms distributed in two independently controllable optical conveyor belts, the semi-classical Hamiltonian can be written as,

$$H_{sc} = (\Delta_0 - \Delta_L)(\hat{\sigma}_{1+}\hat{\sigma}_{1-} + \hat{\sigma}_{2+}\hat{\sigma}_{2-}) + (\Delta_c - \Delta_L)\hat{a}^\dagger\hat{a}$$

$$+ \quad i\sqrt{N_1}g_0(\hat{\sigma}_{1-}\hat{a}^\dagger - \hat{\sigma}_{1+}\hat{a}) + i\sqrt{N_2}g_0(\hat{\sigma}_{2-}\hat{a}^\dagger - \hat{\sigma}_{2+}\hat{a})$$

$$+ \quad \sqrt{N_1}\Omega_1(\hat{\sigma}_{1+} + \hat{\sigma}_{1-}) + \sqrt{N_2}\Omega_2(\hat{\sigma}_{2+} + \hat{\sigma}_{2-}). \tag{3.19}$$

N_1 and N_2 are the number of atoms in the corresponding optical dipole traps (L1 and L2), Ω_1 and Ω_2 are the Rabi frequencies of the respective external probe lasers.

In Figure 14, we compare the results of using Monte-Carlo method (red curve) and those obtained from semi-classical Hamiltonian (blue curve). In these four cases, the cavity QED parameters and the external probe laser intensities are the same, and the differences are the number of atoms in each optical dipole trap. It is readily seen that the semi-classical results in Figure 14(a) and 14(c) do not exactly reproduce the results of the Monte-Carlo method. In Figure 14(b) the semi-classical results have the basic shape and intensity. In Figure 14(d), the results from two different methods are basically the same. It is noteworthy that the lower the cavity output signal is, the better these two methods agree with each other.

In the low excitation limit, $\langle\hat{a}^\dagger\hat{a}\rangle \ll n_0$, the semi-classical Hamiltonian seems to describe the system to a good approximation. n_0 is the cavity photon saturation number defined in Eq. 3.9, and $\langle\hat{a}^\dagger\hat{a}\rangle$ is the average cavity photon number which is related to the cavity output signal by,

$$\text{cavity output signal} = 2\kappa\langle\hat{a}^\dagger\hat{a}\rangle. \tag{3.20}$$

For example, the peak value of the cavity output signal in Figure 14(d) is 0.2 $\times 10^6$, corresponds to an average of 0.0023 cavity photon number, which is smaller than the saturation photon number $n_0 = 0.013$ for the system. On the other hand, the maximum average cavity photon number for the system in Figure 14(b) is 0.045, hence the semi-classical Hamiltonian does not work well in this case.

In order to apply this method to our cavity system with two optical conveyor belts, the AC-Stark shift has to be taken into account and added to the Hamiltonian. The optical dipole traps used in this experiment operate with trapping potential about

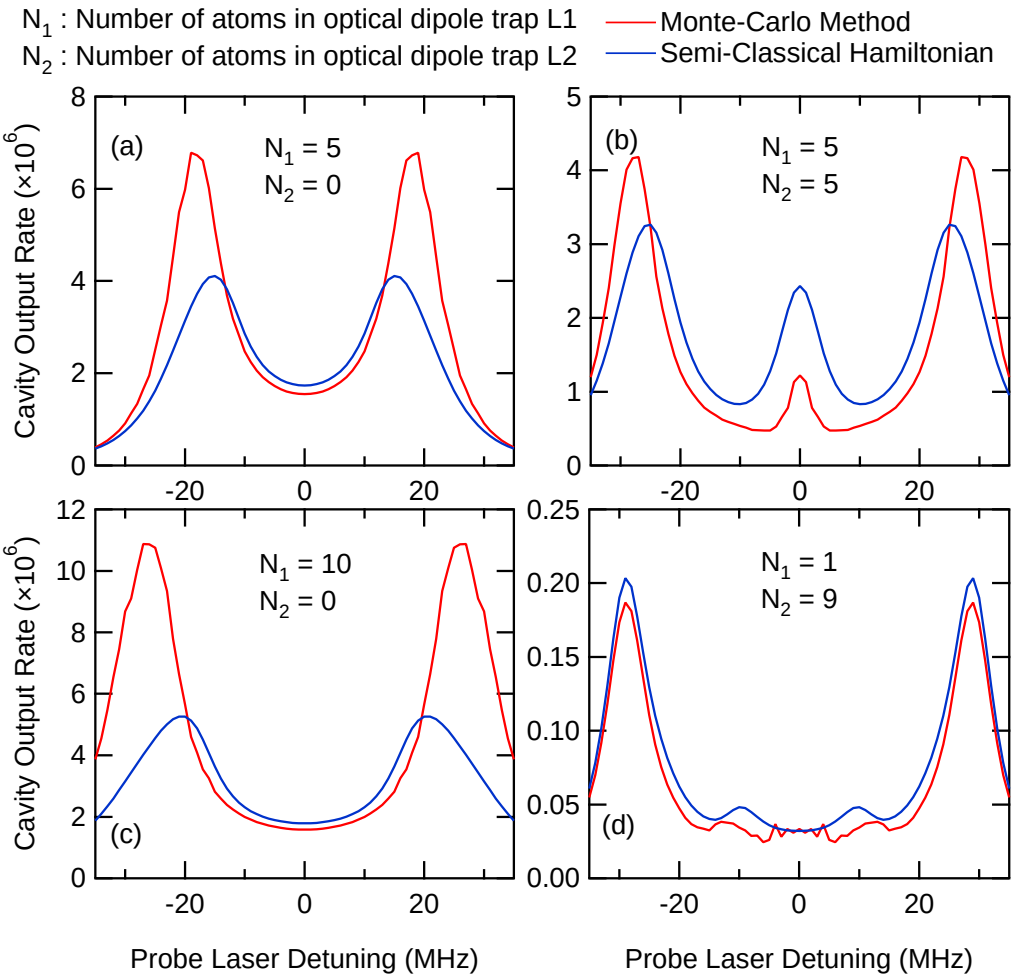

Figure 14: Comparison between the Monte-Carlo method and the semi-classical Hamiltonian. The cavity QED parameters of the system used in the calculation are $\frac{1}{2\pi}(g_0, \kappa, \gamma_\perp) = (9.3, 7.0, 3.0)$ MHz. $\frac{\Omega_1}{2\pi} = 3.4$ MHz, $\frac{\Omega_2}{2\pi} = 0$ and the cavity frequency detuning is 0. It is seen that these two methods agrees well in (d) and the low signal parts of (a), (b), and (c). Suggesting the semi-classical Hamiltonian is accurate for the low excitation case.

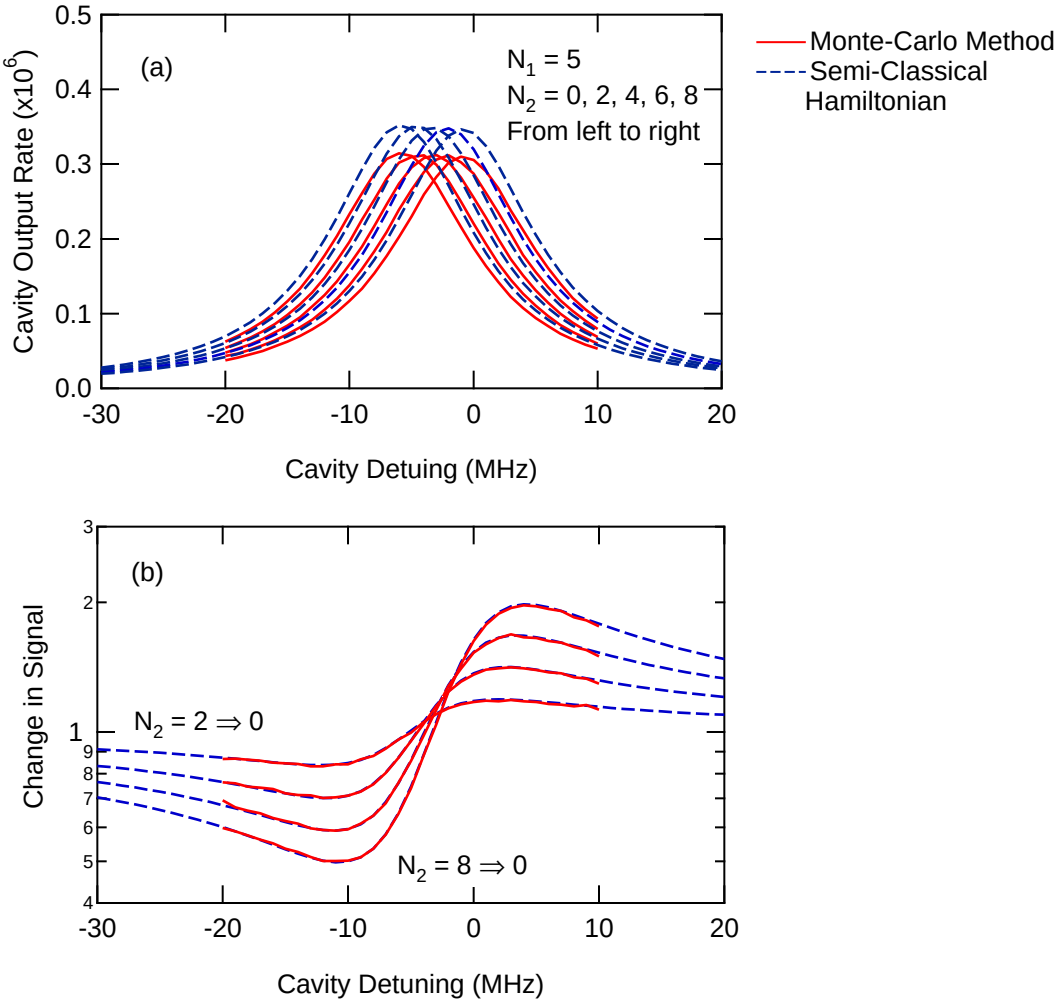

Figure 15: Calculation for a cavity system with two optical conveyor belts. There are 5 atoms in the optical dipole trap directly driven by the external probe laser, and 0, 2, 4, 6, 8 atoms in other trap indirectly driven by the cavity photons. The cavity QED parameters of the system used in the calculation are $\frac{1}{2\pi}(g_0, \kappa, \gamma_\perp) = (9.3, 7.0, 3.0)$ MHz. $\frac{\Omega_1}{2\pi} = 3.4$ MHz, $\frac{\Omega_2}{2\pi} = 0$, the probe laser frequency detuning is -8.9 MHz, and the AC-Stark shift is 130 MHz. (a) Spectrum of the cavity output signal with different number of atoms in L2 using Monte-Carlo simulation and the semi-classical Hamiltonian. (b) The ratio of signal with atoms in L2 to signal without atoms in L2, giving a idea of the dynamics of the cavity output signal as the atoms in L2 are lost from the trap.

2 mK, creating AC-Stark shift about 130 MHz.

The probe laser frequency is -8.9 MHz detuned from the bare atomic resonance in the experiment, and we repeat the experiment with different cavity detuning. Figure 15(a) shows the calculation of the system with up to 13 atoms in the cavity using Monte-Carlo method and the semi-classical Hamiltonian. The system is still in the low excitation limit, hence, the semi-classical Hamiltonian works well. In order to compare the result of the calculation to the experimental data, the ratio of the cavity output signal with a given number of atoms to that without atoms in L2 is plotted in Figure 15(b). It is shown that the results of calculation from these two methods agree very well with each other, therefore we have confirmed that the semi-classical Hamiltonian can be used to describe systems with large number of atoms.

In Chapter 6, we will use the semi-classical model and extend the discussion to about 25 atoms in the cavity, which is beyond the capability of the Monte-Carlo method, and use it to explain the results of the experiment.

CHAPTER IV

EXPERIMENTAL APPARATUS

In the preceding chapter, the theoretical background for the experiments has been discussed. This chapter focuses on the design and important technical details for the single atom experiment and the cavity QED experiment.

4.1 Vacuum System

In order to reduce the collision rate between the trapped atoms and the background particles for maximizing the trap lifetime, the experiment takes place in a evacuated chamber. The vacuum system is maintained at a pressure of 10^{-11} torr. The chamber is constructed mostly with standard stainless steel conflat parts, and a custom made rectangular uncoated quartz cell from Allen Scientific Glass is attached to the chamber with a 2.75" CF flange. The inner cross section of the cell is 1"$\times$1", which allows the use of high numerical aperture imaging lens mounted outside the vacuum system. Figure 16 is a diagram of the vacuum system.

Various pumps are used to bring the pressure of the system to the level of 10^{-11} torr. For initial evacuation, the chamber is connected to a pumping station via a valve. In the pumping station, a roughing pump brings the pressure to 10^{-3} torr, a turbo pump brings the pressure further down to 10^{-9} torr, and a residual gas analyzer (RGA) is used for the purpose of leak checking and monitoring the partial pressure from hydrogen, carbon dioxide, nitrogen, oxygen and water vapor. During the turbo pumping stage, the temperature of the system is brought up to 400° Celsius (100° Celsius if there is a cavity in the chamber) for two weeks. This significantly reduces the water vapor in the system as well as the outgassing of the material used for the cavity.

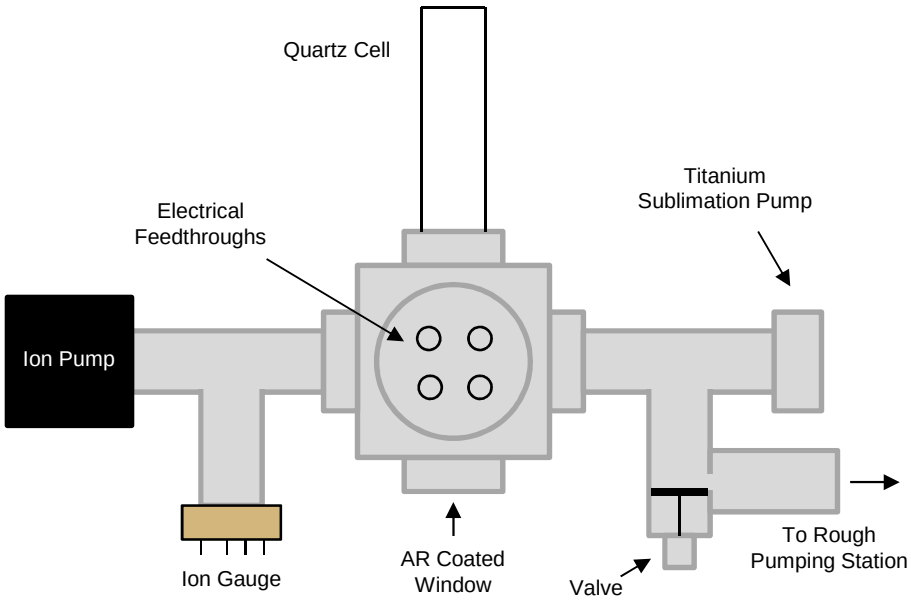

Figure 16: An illustrative diagram of the vacuum system used in the cavity experiment and the single atom experiment.

After the bake out, each filament of the titanium sublimation (Ti-sub) pump is fired several times to bring down the hydrogen partial pressure. At this point, the main chamber is disconnected from the pumping station. The ion pump and the ion gauge on the chamber are turned on after the valve is sealed. The pressure of the system gradually goes down to 10^{-11} torr in a few days. The ion gauge is mostly used for diagnostic purposes after this point and remains off for the rest of the time.

The atom source is provided by a rubidium getter from SAES Getters, which is mounted on an electrical feedthrough. Running current through the getter heats the getter and causes the rubidium atoms to dissociate and release in the chamber. The typical electrical current used ranges from 1.5 A to 4 A.

Running current through the getter temporarily raises the background pressure and the number of rubidium atoms in the chamber. Part of the rubidium atoms ended up coated on the walls of the chamber and the quartz cell. These atoms can be reused by shining a blue light emitting diode (LED) to temporarily raise the vapor pressure of the rubidium. The blue light causes the rubidium to desorb from the quartz cell

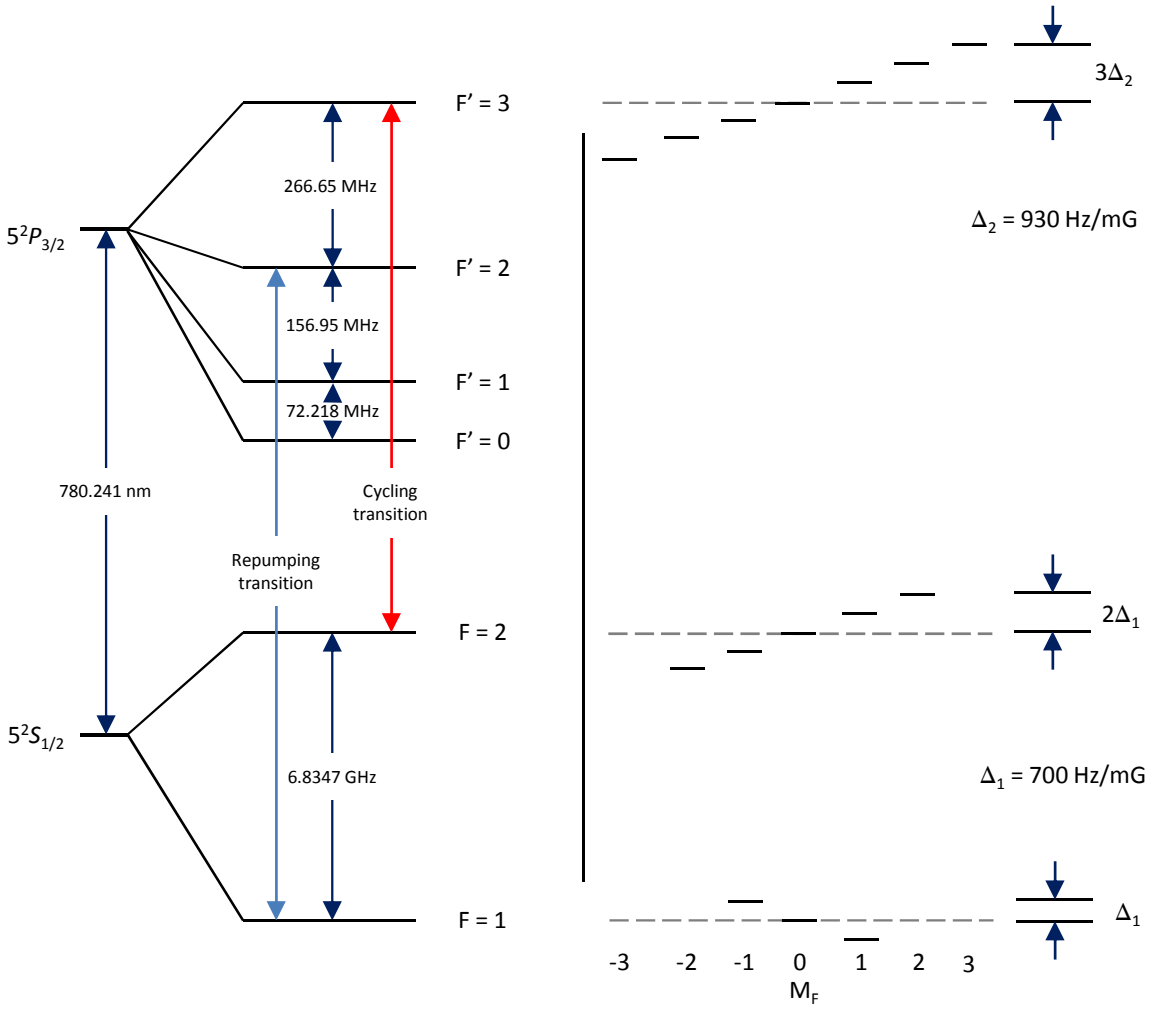

Figure 17: (Left) Energy level diagram for the ^{87}Rb D2 line. (Right) Level structure of the ^{87}Rb $5S_{1/2}$, $F = 1$ and $F = 2$ ground states and the $5P_{3/2}$, $F = 3$ excited state sublevels in a weak magnetic field.

walls. This phenomenon is known as light-induced atom desorption (LIAD) [128], which provides a highly controllable source for this experiment and keep the pressure low for the rest of the time. This technique provides an on-demand atom source for the single atom experiment, and the rubidium getter has not been used for about three years. In the cavity QED experiment on the other hand, the getter is fired once a week for about 30 minutes.

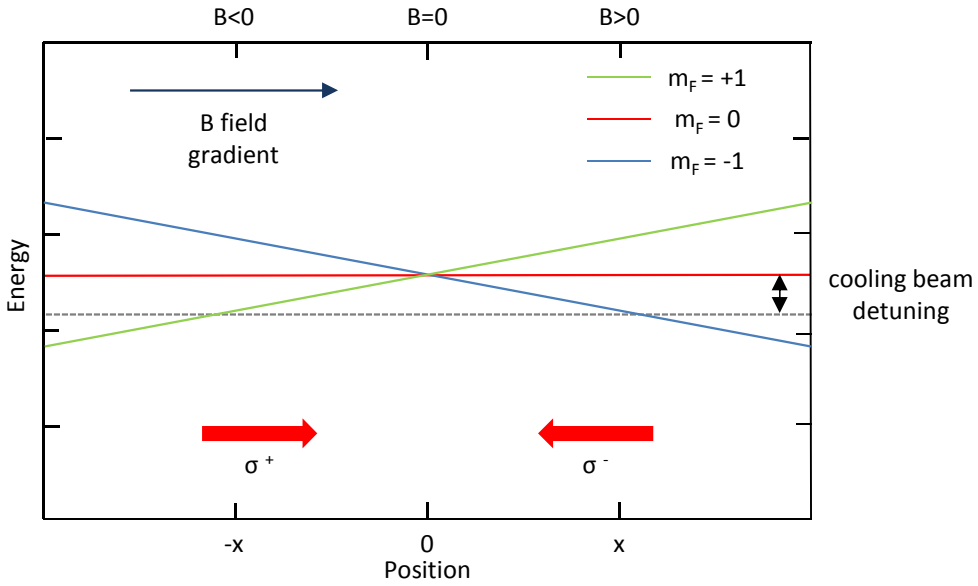

Figure 18: Spatial dependent Zeeman shifts of the F'=1 excited states. The cooling beam is red detuned from the F=0 $\rightarrow$ F'=1 transition shown as gray dashed line. The σ^+ and σ^- cooling beams direction are shown by the red arrows.

4.2 Magneto-Optical Trap

Two essential elements are needed in the making of a magneto-optical trap (MOT): the lasers for optical molasses and repumping and a magnetic field gradient. Figure 17 shows the level diagram of the ^{87}Rb D2 line and the transitions used for laser cooling.

In order to explain how magneto-optical trap works, let us consider an atom with total angular momentum F=0 ground state and F'=1 excited state. With the presence of external magnetic field gradient, the spatial dependent Zeeman shifts of the excited states are shown in Figure 18. The energy shift Δ is given by

$$\Delta = \mu m_F B, \tag{4.1}$$

where μ is the magnetic dipole moment of the electron and B is the magnetic field at the position of the atom. For an atom at x, the energy of the $|F = 1, m_F = -1\rangle$ state is decreased. Hence the atom is more likely to absorb the σ^- light than the σ^+ light and pushed towards the origin. For an atom at $-x$, it is the opposite. This directional and position dependent radiation pressure cools the atoms and confines

them at the origin.

4.2.1 Optical Molasses and Cooling Laser

The MOT lasers consist of two laser systems frequency stabilized near two transitions of the ^{87}Rb D2 lines. Each system comprises an external cavity diode laser (ECDL) as the master laser and injection-locked slave lasers. The diffraction grating of the master laser is mounted in Littrow configuration [129]. All lasers are temperature stabilized with thermo-electric coolers (TEC) and housed in insulating boxes. The TEC is controlled by homemade proportional-integral (PI) circuit based on a design from Hulet's group [130]. The laser diodes used are manufactured by Sharp (GH0781JA2C), which have free running wavelength centered at 784 nm and 120 mW maximum output power. The output wavelength of the ECDL can be coarsely tuned to 780 nm by slightly changing the angle of the grating and fine-tuned to ^{87}Rb D2 lines by changing the temperature and current for the diode.

The trap master laser is locked to the $F = 2 \rightarrow F' = 3, F' = 1$ crossover signal of the ^{87}Rb D2 transition FM spectroscopy, it is -211.8 MHz from the $F = 2 \rightarrow F' = 3$ cycling transition. The laser locking scheme introduces 55 MHz detuning and a double-pass acousto-optic modulator (AOM) further detunes the frequency by 2×100 MHz to 2×140 MHz before injecting to the trap slave laser. The injection locked slave laser is sent through a -110 MHz AOM for fast switching control before fiber coupling and delivered to the experiment. The available detuning range of the trapping laser is -50 MHz to 15 MHz. The injection locked probe slave laser is set up in another independently controlled double-pass AOM configuration centered at 200 MHz, this allows a detuning range much further to the higher frequency to explore the AC-Stark shifted atoms in the optical dipole trap.

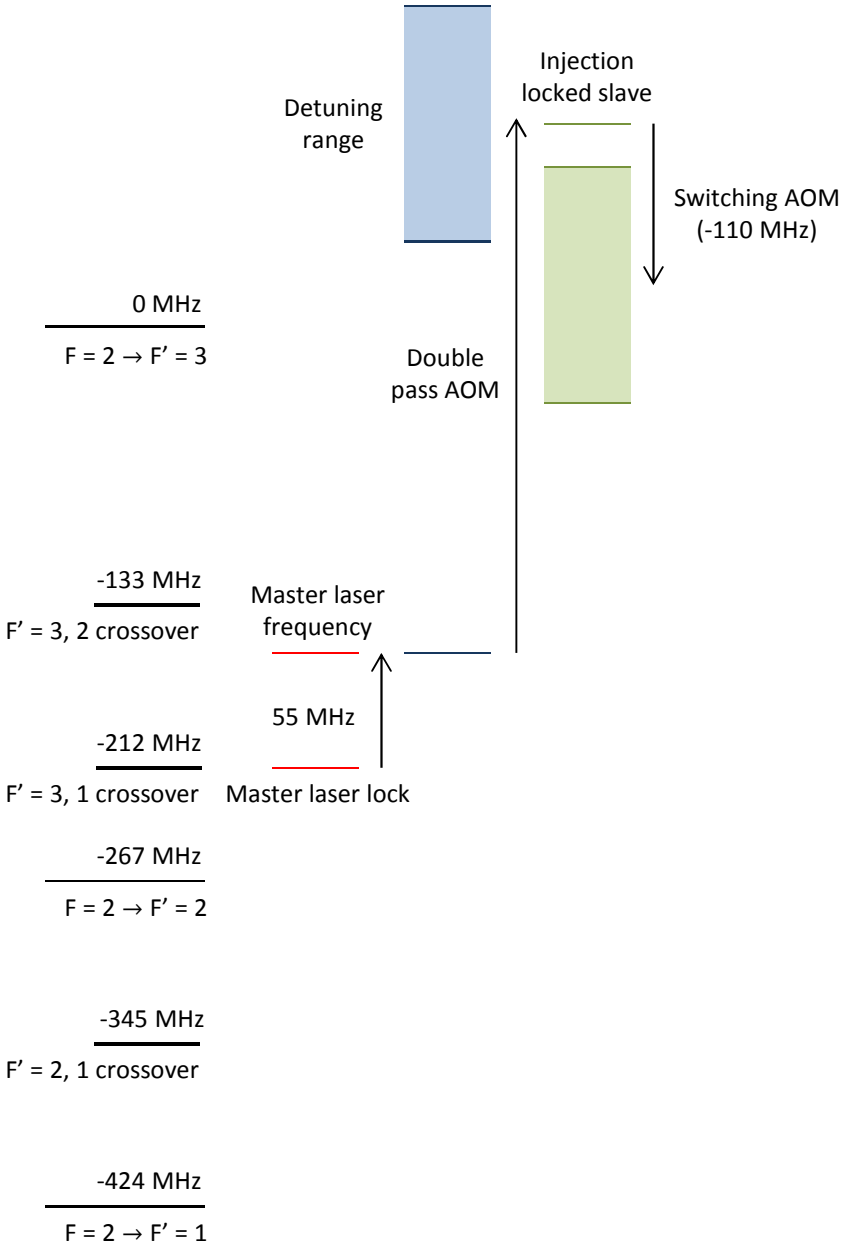

Figure 19: Laser detuning scheme for the master laser and its injection locked slave lasers.

4.2.2 Magnetic Field Gradient and MOT Coils

The magnetic field gradient is generated by two coils arranged in an anti-Helmholtz configuration. The coils are made out of 0.25" diameter copper refrigerator tubing that is wrapped in Kapton tape for electrical insulation. Two different pair of coils are used in single atom and cavity QED experiment. In the single atom experiment, each coil is tightly binded in 5 layers of 8 turns with 2.5" inner diameter. The coils are placed on either side of the quartz cell with 1.5" separation, and it gives a 1.25 $\frac{G/cm}{A}$ current to magnetic field gradient conversion. A maximum magnetic field gradient of 400 G/cm is generated, and it is current limited (320 A) by a 15 kW Electronic Measurement Inc. power supply.

As for the cavity QED experiment, each coil is binded in 3 layers of 4 turns with 2.5" inner diameter. The separation between the coils is 2.75", which gives a 0.56 $\frac{G/cm}{A}$ current to magnetic field gradient conversion. A maximum magnetic field gradient of 280 G/cm is generated, and it is voltage limited (15 V) by the power supply. One of the coils is mounted on a three dimensional translation stage, to allow for fine adjustments of the MOT position with respect to the cavity by a few millimeters in each direction.

The typical magnetic field gradient field required to create a single atom MOT is around 250 G/cm. For loading large number of atoms into the optical dipole trap, the magnetic field gradient is set to 100 G/cm. The ohmic heat load is carried away by running filtered tap water through the copper tube.

4.3 Photon Detection and Imaging System

A diagram of the detection system for the single atom experiment is shown in Figure 20. A high numerical aperture microscope objective (Mitutoyo Corp. Plan Apo NIR Infinity-Corrected 20X) is used to collect the fluorescence from the trapped atoms. A 50/50 beamsplitter is used to send half of the light to an Andor iXon

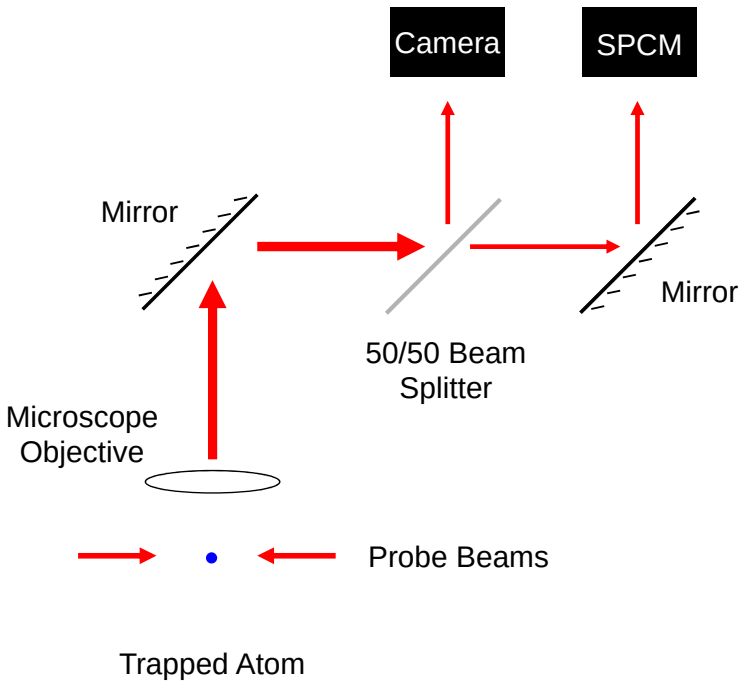

Figure 20: Illustrative diagram of the detection system for the single atom experiment.

EMCCD camera, and the other half to a avalanche photodiode (Perkin Elmer Single Photon Counting Module AQR-14). The camera is used to determine the loading of single atoms in the optical dipole trap. After the single photon counting module is implemented in the system, the camera is mostly used for diagnostic purposes.

4.4 Optical Dipole Traps

Optical dipole traps are used to hold or transport cold atoms initially prepared in the MOT. Various trap designs are used for different purposes, which will be introduced in the following sections. The dipole trap laser is a 20 W fiber laser from IPG Photonics. It is a externally seeded fiber amplifier (Seeding laser: YAR-20k-1064-LP-SF, amplifier: YAR-20-LP-SF) which puts out a single-mode, linearly polarized beam centered at 1064 nm.

4.4.1 Single Focus Trap

The setup of the single focus trap is relatively simple and thus provides a testbed for the loading of cold atoms from the MOT before moving on to other trap designs or for diagnostic purposes. The trap laser beam is initially beam-shaped to a 500 μm beam waist, expanded by 19$\times$ telescope, and finally focused by a 2" diameter achromatic lens with 350 mm focal length. The focused beam has a minimum waist of 18 μm, and with $\sim$3 W of optical power, a trapping potential of 1 mK can be achieved.

4.4.2 1D Optical Lattice

Starting from the single focus trap, the 1D optical lattice can be made by re-collimating the beam on the other side of the chamber and retro-reflecting the beam back on itself. The alignment of the retro-reflecting beam is critical. By using a fiber coupled trap beam, the alignment can be done by fiber coupling the retro-reflected beam back into the incoming fiber. The 1D optical lattice provides multiple trapping sites compared to the single focus trap [25]. Though the loading position is randomized, each trapping site is well defined by the trap beam waist and the standing wave antinodes.

4.4.3 Optical Conveyor

In the cavity QED experiment, cold atoms are initially prepared in the MOT and transported to the cavity several millimeters away. The optical conveyor is constructed with two counter propagating beams. Both beams are the first order diffracted beams of a 40 MHz AOM (IntraAction AOM-402AF4). By detuning the frequency of one beam, the wave envelopes move at the speed v which is proportional to the frequency difference between these two beams.

$$v = \frac{\lambda \Delta\nu}{2}. \tag{4.2}$$

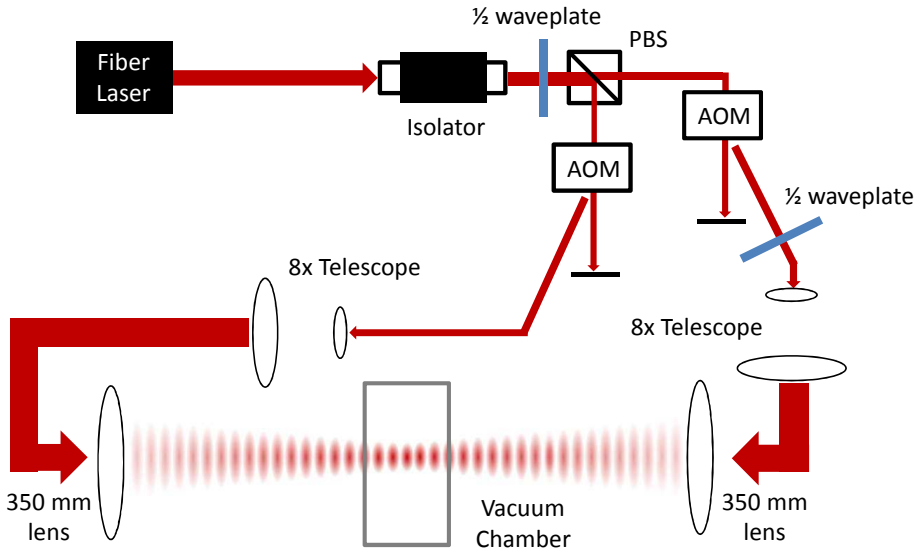

Figure 21: A schematic of the optical conveyor setup used in the cavity experiment. For simplicity, mirrors are not shown in this diagram.

λ is the wavelength of the trap beam, $\Delta\nu$ is the frequency difference between the counter propagating beams. Typically, a 5 kHz frequency difference is applied, yielding a 2.67 mm/s lattice speed. Figure 21 shows the diagram of the optical conveyor setup.

4.4.4 Single Focus Traps with The Imaging System

In the last few sections, several trap designs have been introduced. They share one common feature, the space required is large due to the use of several long focal length optics. For the 1D optical lattice and the optical conveyor, the beam alignment is critical and hence the performance of the trap is very sensitive to the misalignment. For the above reasons, a simple, compact, and robust trap design is desirable. In this section, we will focus on the development of a new trap design for the single atom experiment that fulfills these requirements.

The microscope objective used in our detection system has a much higher numerical aperture (Mitutoyo Corp. Plan Apo NIR Infinity-Corrected 20×, NA = 0.4)

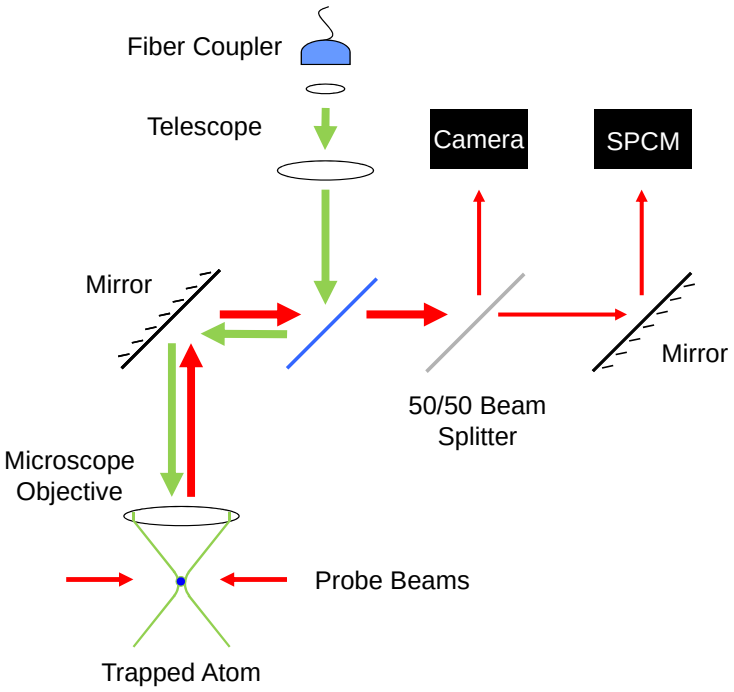

Figure 22: The dichroic beam splitter is used to integrate the single focus trap with the detection system. The reflection efficiency of the 1064 nm light is 99% and the transmission efficiency of the 780 nm light is 95%.

compared to the focusing lens used to create optical dipole trap in the previous sections (f = 350 mm, 2" diameter, NA = 0.07), which enables us to focus the trap laser beam to a minimum waist of several microns. The optical power required to achieve the same trapping potential is much less, and these super tight focus traps typically operate in collisional blockade regime [24, 131], making it an ideal candidate for single atom experiments. In our previous work [41, 132], the loading of single atoms in the 1D optical lattice is completely random and requires automated post processing to select the single atom events. This new trapping scheme can greatly increase the success rate of obtaining single atom events and therefore the overall repetition rate of the experiment.

A IntraAction AOM (AOM-402AF4) is used to control the power of the trap beam. The 40 MHz modulation frequency is generated by a function generator (HP E4430B) and sent to a voltage variable attenuator (Mini-Circuits ZX73-2500). Then the signal

is sent to an amplifier (Delta RF Technology Inc. LA-10-2-512-40) before going to the AOM. The first order diffracted beam from the AOM is fiber coupled and sent to a 4× telescope. The expanded beam has a beam diameter of ∼5 mm and passes through the rear aperture (12 mm diameter) of the microscope objective without getting clipped. The trap laser is combined with the detection system through a 1064 nm/780 nm dichroic beam splitter as shown in Figure 22. The combined detection and trapping system is tested by using the camera to take an image of a pinhole with 50 μm diameter. The image shows that each camera pixel corresponds to 2.5 μm by 2.5 μm at the detection region. In order to make sure the 1064 nm trap laser beam is focused on the focal plane of the detection system, the collimation of the 4× telescope is adjusted. The minimum trap beam diameter is determined to be around 5 μm by comparing to the pinhole diameter.

For a 1064 nm single focus trap with 5 μm beam diameter, the optical power required to create 1 mK trapping potential is around 90 mW. The transmission efficiency of the 1064 nm light through the microscope objective is 75% and 85% through other optics in the detection system. The power control AOM has a deflection efficiency around 70% and the fiber coupling efficiency is 75%. The total efficiency η_{total} of the power delivered to the trap is,

$$\eta_{total} = 75\% \times 85\% \times 70\% \times 75\% = 33\%.$$

With this efficiency, 1 W laser can produce trapping potential more than 3 mK, which is substantially greater than the other trap setups previously used with the same optical power. In the dual lattices cavity experiment, it requires a total of 7 W optical power (losses included) to create a single conveyor with 2 mK trapping potential, and it is limited by the maximum output power of the fiber laser. In the retro-reflection 1D lattice setup of the single atom experiment, it is limited by to the maximum optical power we can apply before damaging the fiber tip, which is about 2.5 W for the continuous running case with 75% fiber coupling efficiency.

To conclude, this tightly focused single focus trap has several advantages compared to some previous trapping schemes used in the single atom experiment:

1. Simple and robust design that utilizes the high numerical aperture lens for trapping and imaging.

2. The tightly focused trap operates in the collisional blockade regime that works as a well-localized source for single atoms.

3. The optical power required to achieve the same trapping potential is much less compared to previous trap designs.

For these reasons, most of the experimental work in Chapter 5 is performed with this new trap design, with some comparisons made to the earlier measurements, performed in the 1D optical lattice.

CHAPTER V

CHARACTERIZING OPTICAL DIPOLE TRAPS WITH SINGLY TRAPPED ^{87}RB

In this chapter, we will present the measurements of the AC-Stark shifted $F = 2 \rightarrow F' = 3$ transitions of the singly trapped ^{87}Rb atoms in the far-off-resonant optical dipole trap (FORT) and demonstrate $m_{F'}$ state dependent light shifts with different polarization of the probe. The temperature of the atoms in the FORT is measured in order to characterize the heating due to probing the atoms. The main motivation of our study is to quantify the state dependent light shift so that it can be used to improve the optical pumping scheme for future quantum information protocols.

Various techniques have been used to measure the AC-Stark shift for optically trapped neutral atoms. For instance, a destructive imaging technique was performed with cesium atoms to measure the differential light shift of the D2 transition [37], where a strong, unidirectional, and near resonant beam is applied to kick the atom out of the trap for different frequency detunings. In other experiments, the transmission spectra of singly trapped ^{87}Rb atoms were obtained and showed a polarization dependent light shift difference of 20 MHz between the $|F = 2, m_F = \pm 2\rangle \rightarrow |F' = 3, m_{F'} = \pm 3\rangle$ transitions in a circularly polarized FORT at 980 nm [39]. Shifts of higher level states were measured using Rydberg excitation spectrum of the ^{85}Rb $5P \rightarrow 50S$ transition in the FORT at 1064 nm [36]. Finally, measurements of the AC-Stark shift for the ^{87}Rb $14D_{5/2}$ Rydberg state was determined by a photoionization spectrum [38].

In our experiment, the measurements of state dependent AC-Stark shift are obtained from emission spectrum with singly trapped ^{87}Rb atoms in optical dipole traps

operating at 1064 nm. A gated probing/cooling technique is utilized to reduce the chance that atoms are heated out of the trap by probing and eliminate the scattering from the cooling beams. Continuous observation of single atoms with trap lifetime over 100 seconds and a signal to noise ratio of 25 has been observed.

5.1 Experimental Setup

The schematic of the experiment is illustrated in Figure 23. The MOT has a six-beam configuration, one pair of the optical molasses beams are along the z-axis (magnetic field gradient direction) and the other two pairs lie on the x-y plane. For each molasses beam, the intensity is 2 mW·cm^{-2} and the beam diameter is 1 mm. To create a single atom MOT, field gradient of 250 G/cm is required. On the other hand, to load large numbers of atoms, the field gradient is set to ∼80 G/cm.

Two different traps are used in this experiment, a single focus trap and a 1D optical lattice. For the single focus trap, a high numerical aperture microscope objective (Mitutoyo Corp. Plan Apo NIR Infinity-Corrected 20×, NA = 0.4) is used to create a tightly focused beam for the optical dipole trap and to collect the fluorescent signal from the trapped atoms. For the 1D optical lattice, the trap beam comes into the vacuum chamber along the y-axis with a minimum waist of 18 μm near the MOT and is retro-reflected by a mirror on the other side of the chamber. Cold samples of ^{87}Rb atoms are initially prepared in a MOT. During the loading stage, the MOT beams are -11 MHz detuned from the $F = 2 \rightarrow F' = 3$ cycling transition. Once the magnetic field gradient is turned off, the MOT beams are further red-detuned to -23 MHz for optimal cooling and the atoms are transferred to the optical dipole trap. The trap beam comes from a ytterbium fiber laser operating at 1064 nm. In order to define the quantization axis for the atoms, the magnetic field is zeroed to less than 10 mG using microwave spectroscopy [133, 134], then a bias magnetic field of ∼500 mG is applied along the y-axis or z-axis.

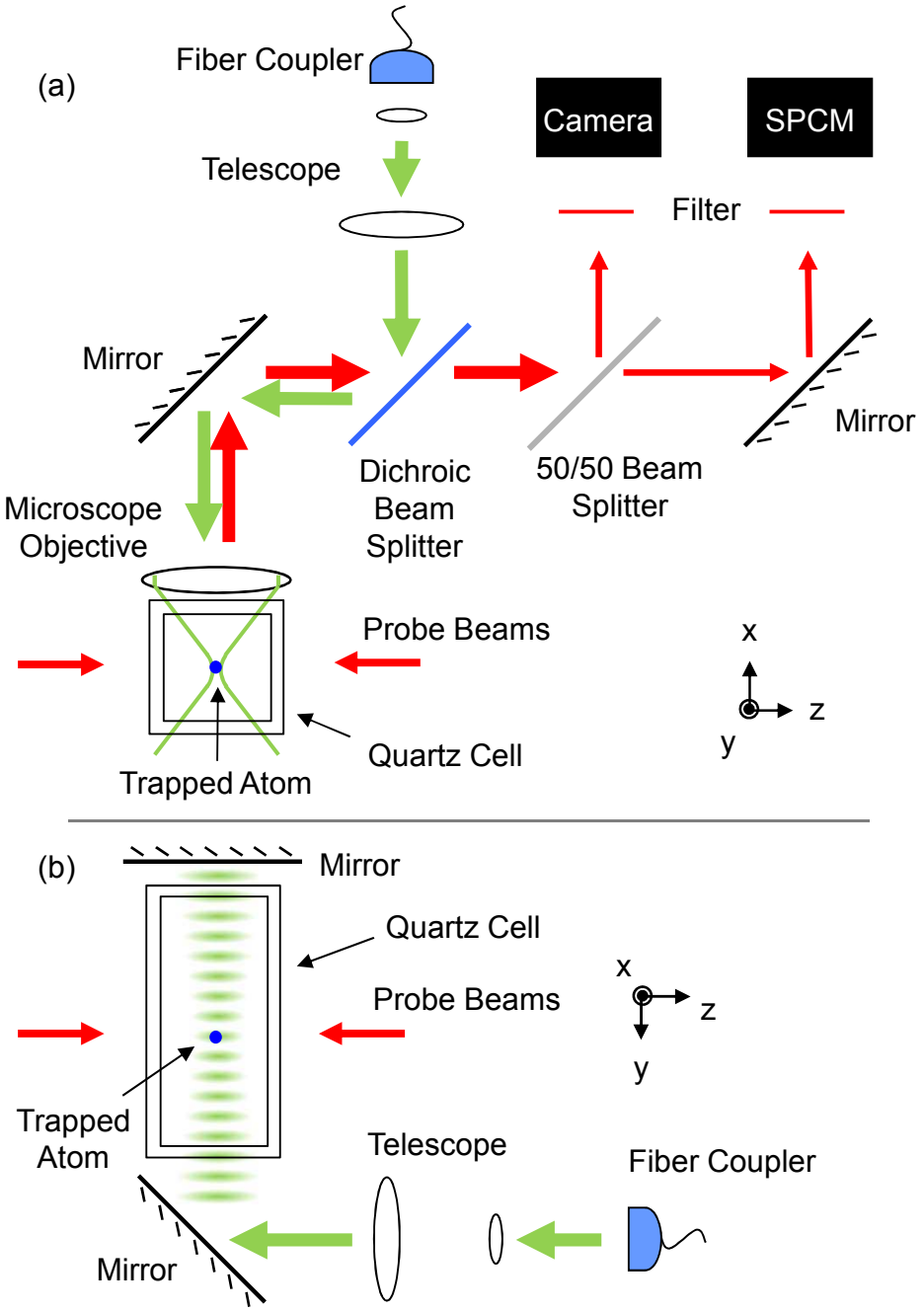

Figure 23: Schematic for the single focus trap and the 1D optical lattice. (a) Single focus trap setup (side view). The long working distance microscope objective is mounted outside the quartz cell. The 780 nm (red) and 1064 nm beam (green) paths are combined with a dichroic beam splitter (CVI Laser Optics SWP-45-RU1064-TU780-PW-2025-C). (b) 1D optical lattice setup (top view), the detection system is not shown for simplicity. In both trapping scheme, the fluorescent signal is collected by the microscope objective, sent to a 50/50 beam splitter, half of the light is sent to a EMCCD camera and the other half is sent to the single photon counting module (SPCM).

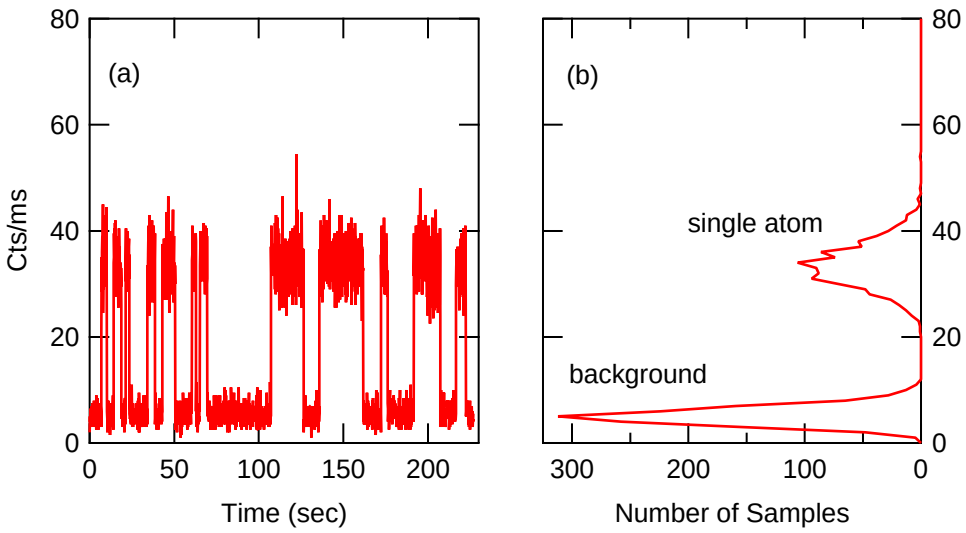

Figure 24: (a) The fluorescent signal of the atoms in the single focus trap when the FORT is continuously being loaded for over 200 seconds. The probe laser is 63.2 MHz blue detuned from the bare resonance and the probe intensity is $\simeq 2I_{sat}$. (b) Histogram of the signal. In this measurement, the gated probing/cooling technique is employed, which will be introduced in Section 5.3.

In order to determine the total photon collection efficiency η for the single photon counting module (SPCM), we measured the transmission efficiencies of the optics in the detection system and the quantum efficiency of the SPCM (PerkinElmer SPCM-AQR-14). The microscope objective has a transmission efficiency of 75%, the line filter has a 95% transmission efficiency, the beamsplitter sends 50% of the light to the SPCM, the SPCM has a measured quantum efficiency of 35% at 780 nm, and 92% transmission efficiency through other optics.

$$\eta = \left(\frac{\mathrm{NA}}{2}\right)^2 \times 75\% \times 95\% \times 50\% \times 35\% \times 92\% = 0.45\%$$

The total photon collection efficiency η of the detection system is 0.45%. In the following sections, we will discuss the loading of single atoms into the FORT and the trap frequency measurements for each trap, respectively.

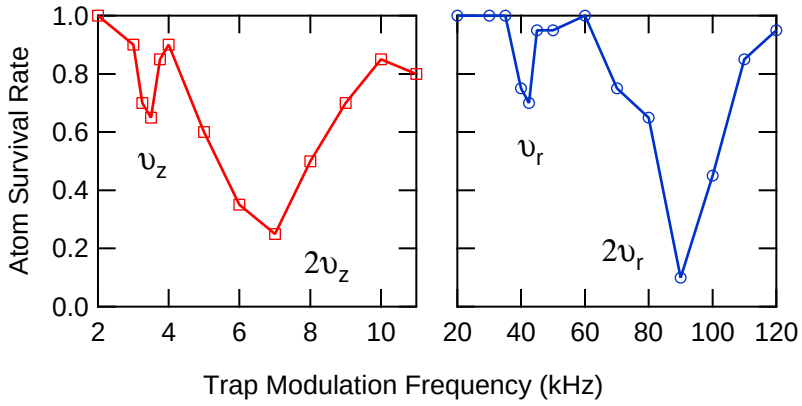

Figure 25: Trap frequency measurements of the single focus trap with parametric excitation. Single atom survival rates are plotted vs the modulation frequencies applied to the trap laser intensity.

5.1.1 Single Focus Trap

The tightly focused single focus trap operates in the collisional blockade regime where light-assisted collisions result in a high two-body loss rate [135]; it ensures that only one atom is loaded each time [24, 131]. Figure 24 shows the loading dynamics of this single focus trap. The probe laser is -3 MHz detuned from the shifted resonance at $\sim$+66 MHz so that the amount of photons scattered by atoms not in the single focus trap is negligible. It is evident that there is a maximum of one atom loaded in the single focus trap. The detection technique used here will be introduced in Section 5.3.

The trapping potential is determined by using parametric excitation to measure the radial and longitudinal trap frequencies [136–138]. Parametric heating leads to a high loss rate of the atoms at modulation frequencies $2\nu/n$ for $n = 1, 2, 3, \ldots$, with the strongest loss at $n = 1$ [136]. The trap laser intensity is modulated at a controlled frequency by an acousto-optic modulator (AOM) before fiber coupled and sent to the experiment chamber. After a single atom is loaded in the trap, the modulation frequency is applied to the AOM for 500 ms before measuring the survival probability of a single atom in the trap. The optimal modulation depth and time for parametric

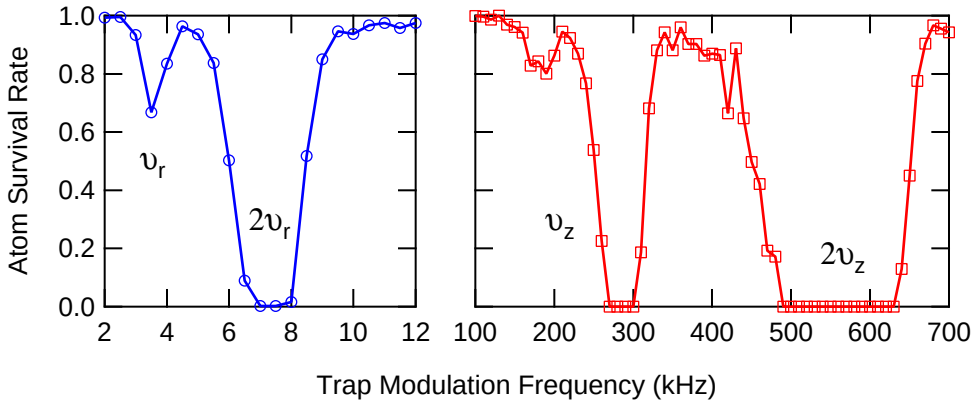

Figure 26: Trap frequency measurements of the 1D optical lattice with parametric excitation. Single atom survival rates are plotted vs the modulation frequencies applied to the trap laser intensity.

heating are determined empirically, typically less than 10% and 1 second, respectively. The procedure is repeated 20 times at each modulation frequency and the resulting survival rate versus modulation frequency graph is plotted in Figure 25. Since there is only one atom loaded at a time, individual successful survival events for single atoms are used instead of the total fluorescent signal from the atoms. With 70 mW trap laser power, the measured trap frequencies of the FORT are $(\nu_r,\ \nu_z) = (42.5,\ 3.5)$ kHz, which corresponds to $\simeq$2.5 μm minimum beam waist and $k_B\times$0.88 mK trapping potential (equivalent to $h\times$18 MHz).

5.1.2 1D Optical Lattice

The trapping potential of the 1D optical lattice is also determined with the trap frequency measurement. The results are shown in Figure 26. The initial trap loading is followed by image acquisition with 1 second exposure time, then the modulation source is turned on for 500 ms before the second image is taken. Finally the trap laser is switched off and a background reference image is taken. There are 50 atoms initially loaded into the 1D optical lattice on average. This procedure is repeated 20 times at each modulation frequency and the results are normalized to unity. With 1.4 W trap laser power, the measured trap frequencies of the FORT are $(\nu_r,\ \nu_z) =$

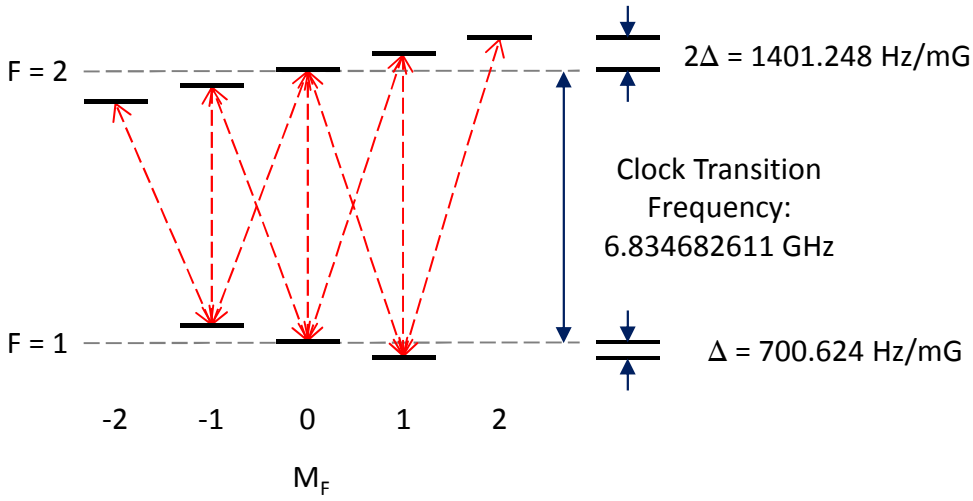

Figure 27: Level structure of the ^{87}Rb $5S_{1/2}$, $F = 1$ and $F = 2$ ground states sublevels in a weak magnetic field.

(3.8, 280) kHz, which corresponds to $\simeq$18 μm minimum beam waist and $k_B \times 1.1$ mK trapping potential. The sub-micron confinement in the longitudinal direction makes the single trapping site highly anisotropic, with the longitudinal trap frequency nearly two orders of magnitude larger than the radial trap frequency.

5.2 Microwave Spectroscopy - Zeroing The Magnetic Field

In order to zero the magnetic field, we utilize microwave spectroscopy of the ^{87}Rb $5S_{1/2}$, $F = 1$ and $F = 2$ ground states sublevels. In the weak magnetic field limit, where the interaction is much weaker than the hyperfine coupling, the Zeeman splitting between the adjacent hyperfine sublevels is linear with the magnetic field (700.624 Hz/mG). Figure 27 shows the level structure of the hyperfine ground states under a weak magnetic field. For atoms randomly distributed in the ground state manifolds, the resonances of the microwave spectroscopy occur at 2Δ, Δ, 0, $-\Delta$, and -2Δ detuning from the clock transition frequency (6.834682611 GHz).

In order to generate the microwave at the clock transition frequency, a 3.417 GHz signal is generated by a function generator (HP E4422B), which is phase-locked to a 10 MHz reference (EndRun Technologies Prælcis Gfr). The signal is sent to a RF switch

before sending to the frequency doubler. The signal then passes through a isolator to prevent feed-back from the amplifier. Finally, the signal is sent to a amplifier (ALGA Microwave ALPA-647240-50-01) before connecting to a cylindrical copper horn [137].

In the experiment, a fluorescent image of the atoms is taken with 1 s exposure time after the initial trap loading to determine the number of atom in the 1D optical lattice. The atoms are then prepared in the $F = 1$ ground state before applying the microwave pulse tuned to the $|F = 1, m_F = 0\rangle \rightarrow |F = 2, m_F = 0\rangle$ clock transition. Then a resonant, unidirectional laser is applied to kick the atoms in the $F = 2$ states out of the trap. Finally, an fluorescent image of the remaining atoms is taken with 1 second exposure time to determine the atom survival rate.

Figure 28(a) shows the process of determining the π-pulse length that maximizes the coherent transfer of atoms from the $F = 1$ state to the $F = 2$ state. The experiment is repeated ten times at each microwave pulse length and there are on average twenty atoms loaded in the lattice at each run. The red dashed line at 54% represents the atom survival rate without applying microwave pulse, 46% of the atoms are lost during the two fluorescent image acquisition process which is due to the trap lifetime and the loss from the detection process. It can be inferred from the figure that the π-pulse length is 150 μs which corresponds to a 6.7 kHz linewidth. The atoms are initially randomly distributed among the m_F states of the $F = 1$ manifold, which means that typically only one third of the atoms will be affected by the microwave pulse. Therefore, an oscillation contrast of 33% should be observed instead of 10%. The disagreement possibly comes from the loss of atoms in the first image acquisition process or because the atom kick-out beam does not work efficiently. The former causes the number of atoms in the $|F = 1, m_F = 0\rangle$ state becomes less than 1/3 of the original number of atoms, the latter further reduces observed contrast. The loss of atoms due to data acquisition can be improved by reducing the exposure time, but it will increase the number of experimental runs to achieve the same signal to noise

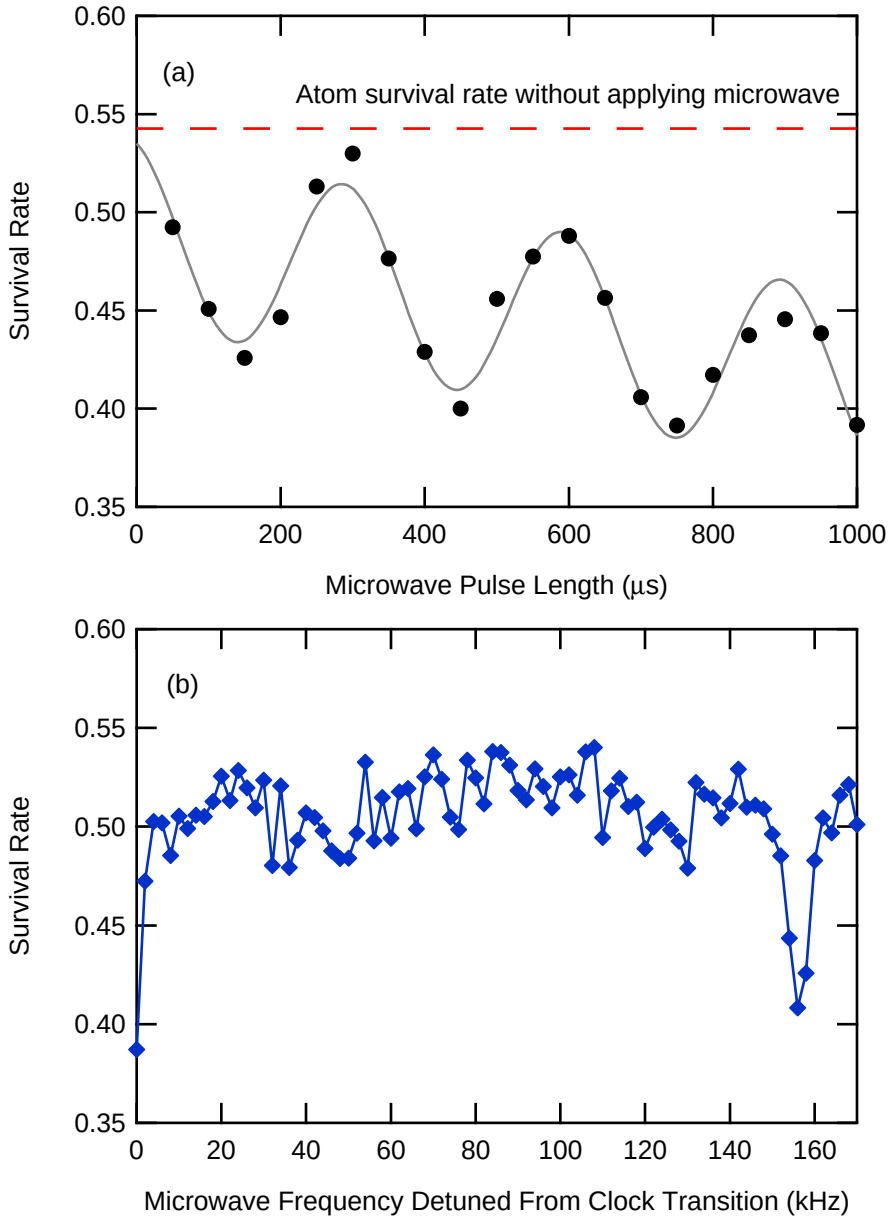

Figure 28: (a) The process of determining the π-pulse length that inverts the population. (b) Microwave spectroscopy that shows the first resonance at Δ detuning.

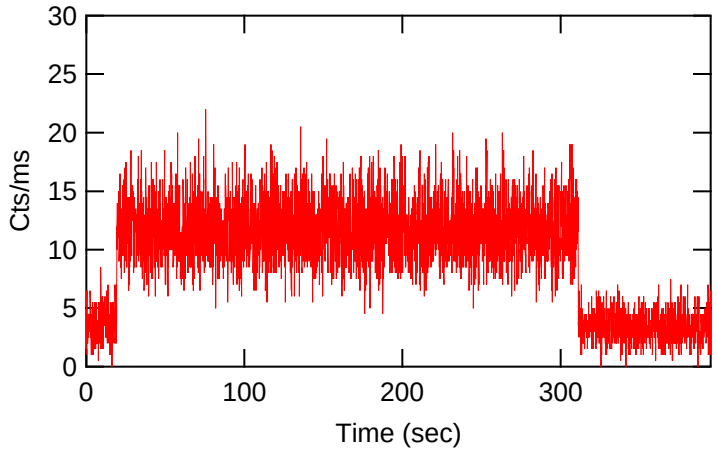

Figure 29: An example of long trap lifetime of the single focus trap. The probe laser detuning is 49.2 MHz and the intensity is $\simeq I_{sat}$.

ratio. For the purpose of measuring and zeroing the magnetic field, a 10% drop in the atom survival rate is more than enough to determine the microwave spectrum.

Having determined the π-pulse duration, the experiment is now repeated at different microwave frequencies with 2 kHz steps. The frequency step has to be smaller than the linewidth of the microwave pulse to ensure the coverage of the desired signal. The microwave π-pulse at the clock frequency coherently drives the atoms from the $|F = 1, m_F = 0\rangle$ state to the $|F = 2, m_F = 0\rangle$ state. At microwave frequency Δ ($\Delta > 0$) detuned from the clock frequency, the $|F = 1, m_F = 0\rangle \rightarrow |F = 2, m_F = 1\rangle$ and the $|F = 1, m_F = 1\rangle \rightarrow |F = 2, m_F = 0\rangle$ transitions are driven as shown in Figure 27. Figure 28(b) shows a scan that covers the first peak at 156 kHz, which corresponds to a field of 233 mG. The experiment is repeated near the previous frequency detuning after slightly adjusting the current of the bias coils one axis at a time. The background magnetic field can be canceled to within $\sim$10 mG, limited by the linewidth of the π-pulse and AC background fields in the lab. After zeroing the magnetic field, the quantization axis is then defined by applying current to the desired pair of bias coils. Finally, microwave spectroscopy is done one more time to determine the strength of the magnetic field.

5.3 Gated Probing/Cooling Technique

In our system, the MOT beams scattering off the quartz cell walls is the major source of background for atom detection. It makes the detection of single atoms difficult as the fluctuation of the background is comparable to the signal from single atoms. On the other hand, the MOT beams are required for sub-Doppler cooling in order to achieve trap lifetime over 100 seconds [132]. In this section, we will begin with the discussion of single atom detection with the camera and the SPCM and move on to the implementation of the gated probing/cooling technique. The latter has allowed us to continuously observe a single atom with a signal to noise ratio of 25 for over 100 seconds, which is ideal for studying the light shifted spectrum of the optically trapped single atoms.

In our detection system, each camera pixel corresponds to 2.5 μm by 2.5 μm in the trapping region. The atom position in the single focus trap is localized within 2 by 2 pixels. On the camera, the scattering of the MOT beams corresponds to 2.5×10^3 cts/s per pixel and 2.5×10^3 cts/s $\times$ $2^2 = 10^4$ cts/s over the region of interest with a fluctuation of 100 cts/s. For single atoms in the FORT excited by the MOT beams with a detuning of -70 MHz from the shifted resonance, the count rate is $\simeq$1000 cts/s on the camera, which corresponds to a signal to noise ratio of 10.

Though single atoms can be well distinguished on this system with the camera, a technique for detecting single atoms excited with arbitrary detuning with high repetition rate while keeping the same atom is preferred. To probe the atom near the shifted resonance, a pair of counter-propagating probe beams are set up along the z-axis as shown in Figure 23, which gives a maximum signal of $\sim$40 cts/ms on the SPCM. For comparison, the scattering of the MOT beams off the quartz cell walls greatly exceeds the fluorescent signal from single atoms, typically on the order of 1000 cts/ms, which gives a signal to noise ratio of $\sim$1. The signal to noise ratio can be improved by reducing the field of view of the SPCM (currently 50 μm by 50 μm)

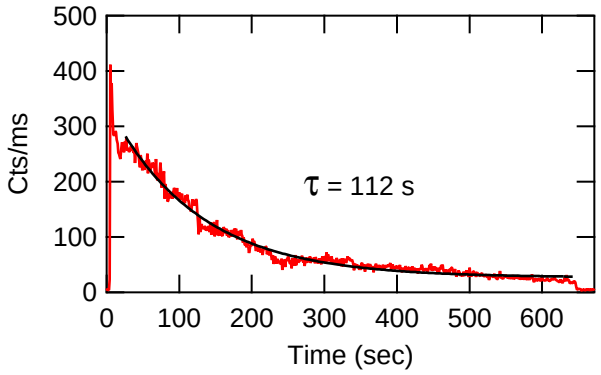

Figure 30: Population of trapped atoms in a 1D optical lattice. The trap lifetime is 112 s. Single atom count rate is 23.4 cts/ms so there are ∼10 atoms loaded in the trap in the beginning.

which increases the alignment difficulty of the imaging system. The more favorable method is to completely turn off the MOT beams during the probe stage.

In order to reduce the background scattering, a gated probing/cooling technique is employed. The MOT and the probe beams are switched on and off in an alternative manner such that the SPCM is on during the probing period and off during the cooling period. After each probing period, the atoms are sub-Doppler cooled by the MOT beams to the bottom of the trap, to suppress the possibility of losing atoms due to heating from the probe process. The total background scattering is typically less than 3 cts/ms for the probe power used in the experiment. The resulting signal to noise ratio is ∼25, which is a factor of 20 improvement. This technique enables us to perform operation with repetition rate up to 10 kHz and retains the high signal to noise ratio. Figure 29 shows the continuous observation of a single atom in the single focus trap for over 250 seconds with the gated probing/cooling technique. For every 100 μs, the atom is probed for 1 μs and cooled for 99 μs. Figure 30 shows the population of trapped atoms in the 1D optical lattice continuously observed with the same technique. It allows us to probe single atoms over a large detuning range with a lifetime over 60 seconds, which is well suited for measuring the AC-Stark shifted spectrum for the optically trapped atoms.

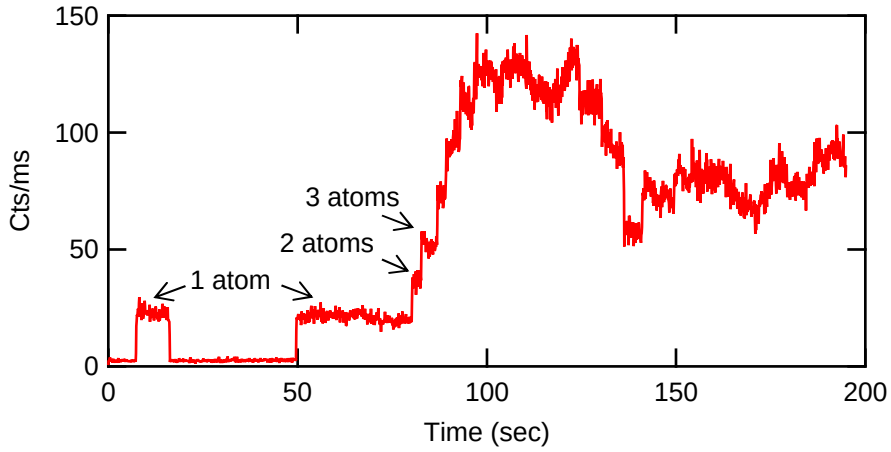

Figure 31: Fluorescent signal of atoms in the MOT using the gated probing/cooling technique. Single atom count rate is 18.5 ct/ms, which can be inferred from the discrete jumps in the signal.

5.4 Single Atoms in the MOT

The gated probing/cooling technique is first applied to study atoms in the MOT. Figure 31 shows the SPCM fluorescent signal of atoms in the MOT when it is being continuously loaded. The discrete jumps of the fluorescent signal can be used to determine the single atom count rate. The single atom count rate is 18.5 cts/ms and the background is 2.5 cts/ms. For this measurement, the probe beam power is 11.5 μW, the probe beam waist is 125 μm, and the probe detuning is -6.8 MHz from the bare atom resonance.

In Figure 32(a), the spectrum of single atom in the MOT is measured with different probe power. The magnetic field gradient is set to $\sim$250 G/cm to ensure only one atom can be loaded into the MOT. The experiment data are well fitted to the Lorentzian distribution centered near the atomic resonance. One possible source of the -2 MHz frequency shift in the spectra is the drift of the AOM modulation source (voltage control oscillator) in the probe laser setup and the laser locking setup as shown in Figure 19. Another potential source of this frequency shift is the Zeeman shift, in which case the atoms are not trapped at zero magnetic field region due to unbalanced MOT beams. The maximum count rates for 11.5 μW and 21.3 μW probe power are

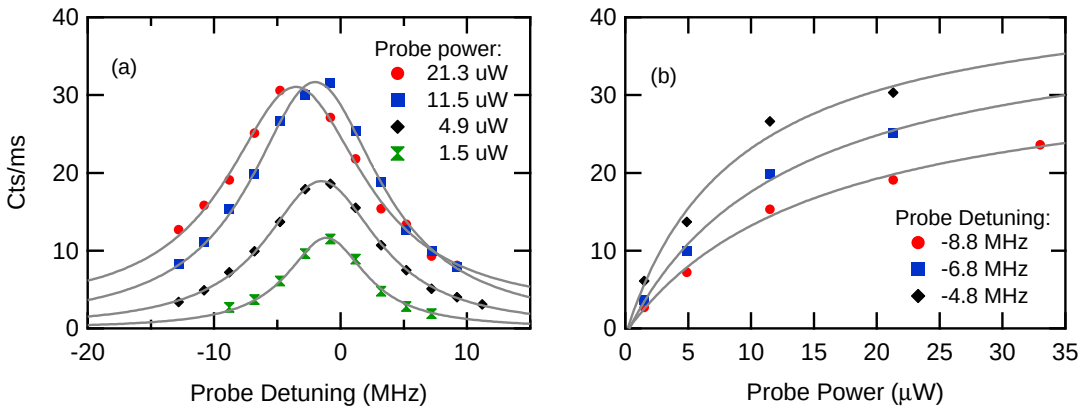

Figure 32: (a) Spectrum of single atoms in the MOT. The probe laser is detuned with respect to the resonance of the $5S_{1/2}$, $F = 2 \rightarrow 5P_{3/2}$, $F' = 3$ transition. (b) The single atom count rates are plotted vs the probe beam powers at different probe detunings.

very close, which indicates the atomic transition is nearly saturated. In Figure 32(b), a plot of the count rates of single atoms in the MOT versus the probe beam powers is presented, showing the saturation of the photon scattering rate. The data in Figure 32(a) are fitted to the Lorentzian distribution of the two-level system scattering rate. The data in Figure 32(b) are fitted to the photon scattering rate formula for a two-level atom [113],

$$R_{sc} = \frac{\gamma}{2}\frac{s}{2(1+s)},$$
$$s \equiv \frac{I/I_{sat}}{1+(2\delta/\gamma)^2}, \tag{5.1}$$

where s is the saturation parameter of the transition which is proportional to the probe laser intensity I, I_{sat} is the saturation intensity of the transition, γ is the decay rate of the excited state, and δ is the probe laser detuning from the transition.

5.5 Measurements of The Light Shifted Spectrum

With the demonstration of the gated probing/cooling technique with single atoms in the MOT, we're now ready to measure the light shifted spectrum of of single atoms in the optical dipole trap. Figure 33 shows the AC-Stark shift of the $5S_{1/2}$, $F = 2$

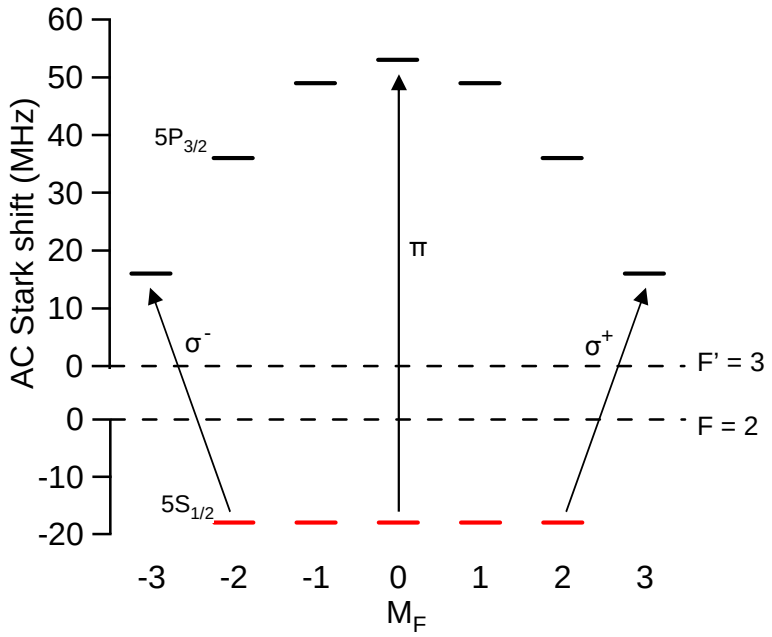

Figure 33: AC-Stark shift of the $5S_{1/2}$, $F = 2$ ground states and the $5P_{3/2}$, $F' = 3$ excited states. In the experiment, different polarization of light is used to quantify the quadratic light shifts of the excited states. The trapping potential used for this calculation is 0.88 mK. The trap beam is linearly polarized along the quantization axis, and the ground states are uniformly lowered by $h \times 18$ MHz.

ground states and the $5P_{3/2}$, $F' = 3$ excited states. As shown in the figure, different polarizations of probe can be used to quantify the splitting within the hyperfine manifold. When the atom is pumped by linearly polarized light, the steady state population is heavily weighted around $m_F = 0, \pm 1$ states [139]. On the other hand, when the atom is pumped by circularly polarized lights, the atom is driven to the respective stretched state at the steady state. Therefore, the spectrum of the atom pumped by linearly polarized light can be characterized by three transitions with relatively close shifted detuning, where as the atom pumped by circularly polarized light can be characterized mostly by the cycling transition.

In Figure 34, the AC-Stark shifted spectrum of single atoms are measured for different trap depths. In these measurements, both the trap beam and the probe beams are linearly polarized along the bias magnetic field direction (y-axis, shown in Figure 23). The atoms are initially loaded in the FORT with 0.88 mK trapping potential,

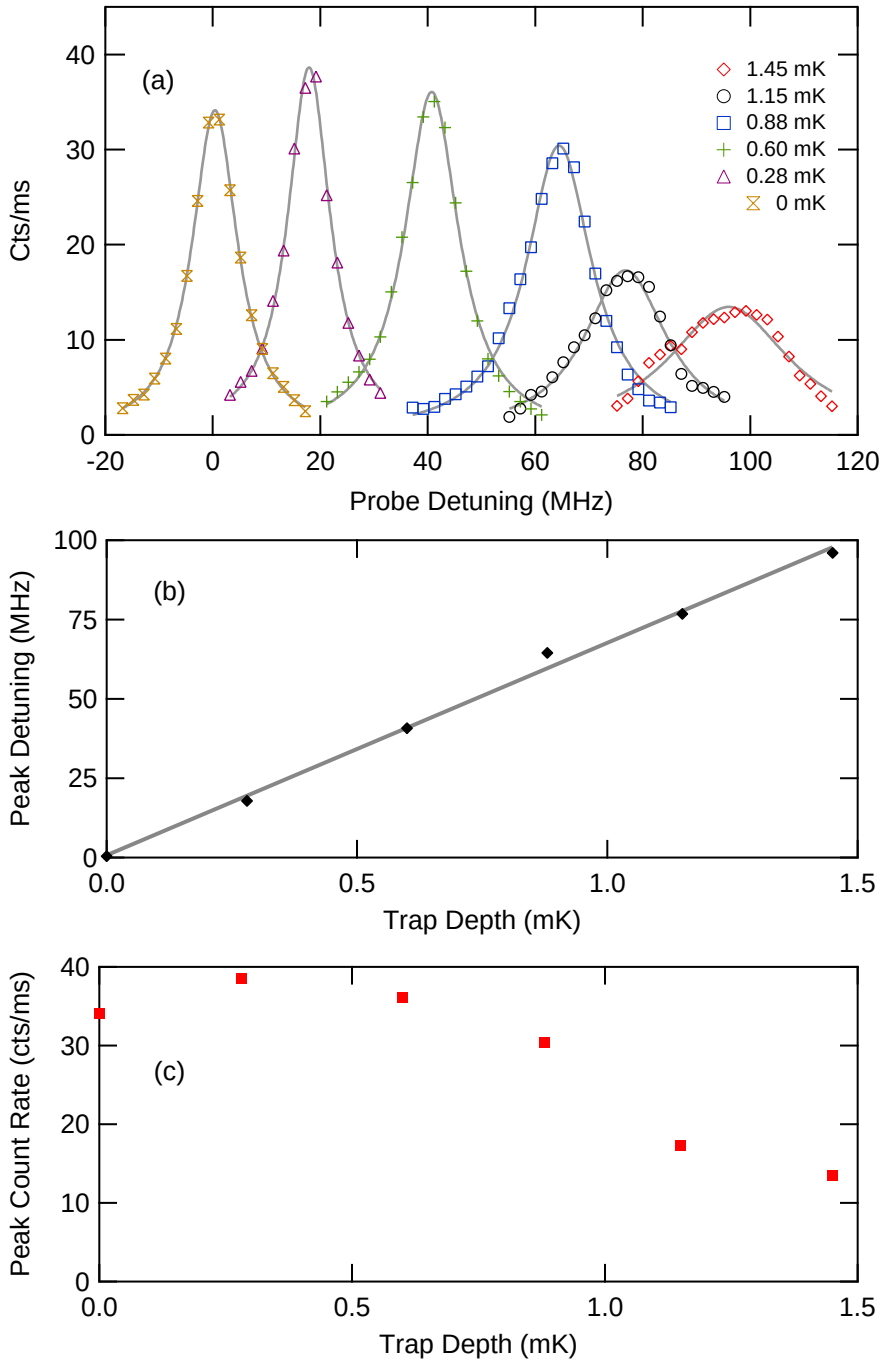

Figure 34: (a) Spectrum measurements of single atoms in different trapping potentials using gated probing/cooling technique. The probe intensity is $\simeq 2I_{sat}$. (b) Peak detuning vs trap depth, the slope is 67 ± 2 MHz/mK from line fitting. (c) Peak count rate vs trap depth.

then the trap laser power is increased/decreased to the final value for the measurements. In Figure 34(a), each data point is obtained by averaging over the fluorescent signal from one and the same atom for about 60 seconds. The gated probing/cooling technique is used for these measurements, with typical probing and cooling time set to be 1 μs and 99 μs, respectively. The resulting spectra fit well to the Lorentzian distribution centered near the respective $|F = 2, m_F = 0\rangle \rightarrow |F' = 3, m_{F'} = 0\rangle$ transitions. It suggests that the single atom population is heavily weighted on the $m_F = 0, \pm 1$ states after driven by the probe laser for 1 μs.

For the spectrum measurements of the untrapped single atoms (0 mK), the probing time is reduced to 500 ns to reduce the chance of losing the atom, and the trap beam power is switched off for 1 μs during the probing period. The AOM used for trap beam power control (IntraAction AOM-402AF4) has a measured optical rise and fall time (10% $\leftrightarrow$ 90%) of 200 ns. The probe laser, trap beam control, and the gating for the SPCM are triggered from two pulse generators (Stanford Research Systems DG535) for independent control. The spectrum for this measurement is fitted to a Lorentzian distribution centered at 0.4 MHz from the bare resonance, which is likely due to a small error of the probe laser frequency relative to the atomic transition.

Figure 34(b) is the plot of the peak detuning versus trap depth. The peak detuning is linearly dependent to the trap depth with a slope of 67 MHz/mK which compares well with the theoretical result of 80 MHz/mK presented in Chapter 2. Figure 34(c) is the plot of peak count rate versus trap depth, the drop in maximum count rate at high trap depth is due to the increase of linewidth broadening. The source of linewidth broadening was introduced in Section 2.8, and will be further discussed in Section 5.7.

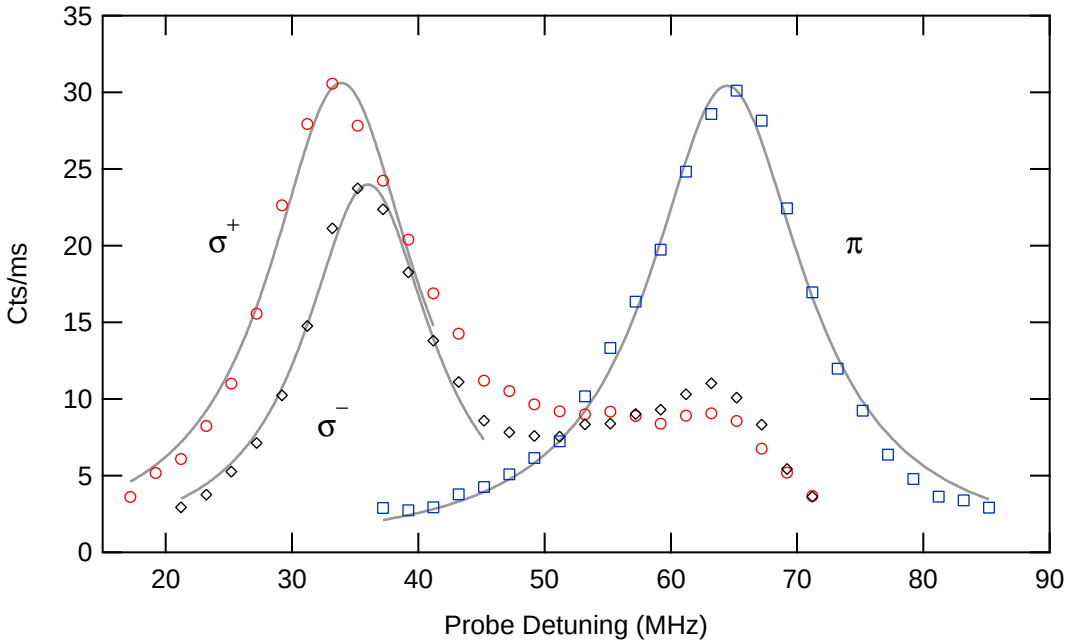

Figure 35: The spectrum of single atom with circularly and linearly polarized probe. The trapping potential is 0.88 mK for all these measurements.

5.6 Differential Light Shift within Zeeman Manifold

To demonstrate and quantify the m_F state dependent AC-Stark shift, we change the linearly polarized probe beams to left and right circularly polarized probe and compare the results with the same trapping potential. The trap beam polarization is rotated 90° and it is now along the probe beam propagation direction and bias magnetic field direction (z-axis, shown in Figure 23). Figure 35 shows the spectrum of single atoms in the single focus trap with different polarization of probe beams. The circularly polarized probes drive the atom to the stretched states, making the major peak centered at a much lower frequency. The calculation shown in Figure 33 indicates the difference is about 35 MHz for this trap depth, which agrees well with the data shown in Figure 35. The tails in the high frequency for the measurements with circularly polarized probes are possibly due to either imperfect alignment between the bias magnetic field and the probe beam propagation direction or imperfect polarization of the probe and trap beams. The Lorentzian fitting of the spectrum peaks are centered at

$(\sigma^+, \sigma^-, \pi) = (33.9\pm0.2, 36.0\pm0.1, 64.4\pm0.1)$ MHz with the same FWHM of 14 MHz. From the calculation, the $|F = 2, m_F = \pm2\rangle \leftrightarrow |F' = 3, m_{F'} = \pm3\rangle$ transitions are 34 MHz blue detuned from the bare resonant frequency and the $|F = 2, m_F = 0, \pm1, \pm2\rangle \leftrightarrow |F' = 3, m_{F'} = 0, \pm1, \pm2\rangle$ transitions are 71, 67, and 54 MHz blue detuned, respectively. For the $|F = 2, m_F = \pm2\rangle \leftrightarrow |F' = 3, m_{F'} = \pm3\rangle$ transitions, the measurements show good agreements with the calculation. On the other hand, the measurement with the linear polarized probe, the peak is about -5 MHz from the calculated $|F = 2, m_F = 0, \pm1\rangle \leftrightarrow |F' = 3, m_{F'} = 0, \pm1\rangle$ transitions. An explanation will be provided in the next section in which the temperature measurements of these single atoms are also presented.

The peak detunings for the σ^+ and σ^- probe beams are 2 MHz apart from each other. It is smaller than the natural linewidth but it is an indication that the trap laser is elliptically polarized and the trap beam propagation direction is not completely perpendicular to the quantization axis. It is shown in Eq. 2.52 that the light shift has a term linearly dependent to m_F and it is non-vanishing if both of these two requirements are not satisfied. Peak detunings separation of $\sim$20 MHz has been observed in a circularly polarized trap with 1.3 mK trapping potential [39].

5.7 Temperature Measurements and Linewidth Broadening

In Chapter 2, the discussion of the linewidth broadening due to the spatial varying light shifts has been introduced. This broadening is proportional to the temperature of the optically trapped atoms and provides an explanation for the linewidth broadening shown in Figure 34(a). In this section, temperature measurements of the single atoms in the optical dipole trap will be presented. In the experiment, single atoms are initially loaded in the trap, then the AOM controlled trap beam is switched off for a variable amount of time and turned back on. During the trap off period, the atom moves in a random direction with kinetic energy associated with the atom temperature

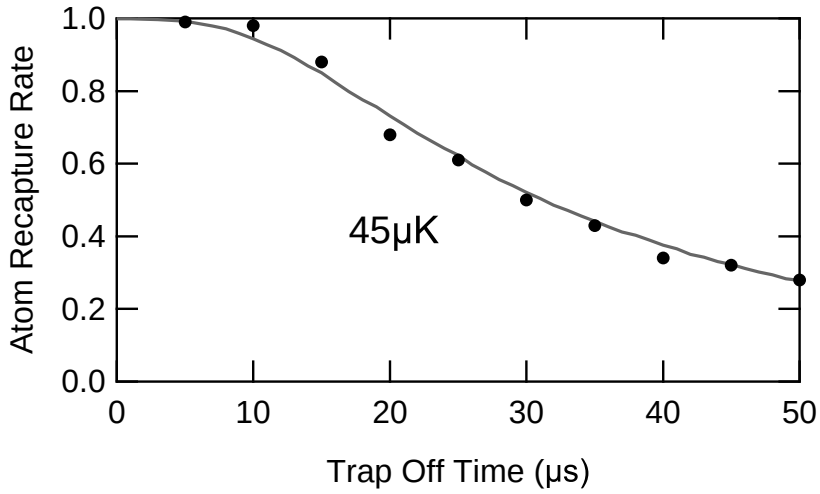

Figure 36: Temperature measurements of single atoms in the single focus trap with 0.35 mK trapping potential fitted to the Monte-Carlo simulation at 45 μK.

and its initial position from the center of the trap. If the total energy (kinetic and potential energy) of the atom is greater than zero when the trap is turned back on, the atom will escape from the trap. The successful rate of recapturing the atoms is determined by the trapping potential, the geometry of the trap and the kinetic energy of the atoms.

Figure 36 shows the results of the drop and recapture measurements in the single focus trap with 0.35 mK trapping potential. After successfully loading the single atom into the trap, the probe beams and the MOT cooling beams are switched off 10 ms before lowering the trap beam power. After the pre-programmed trap off time has passed, the probe beams and the MOT cooling beams are turned back on 10 ms after the trap beam to determine whether if the recapture is successful or not. The trap beam is controlled by an AOM with a measured 200 ns optical rise and fall time, which is much shorter compare to the inverse of the trap frequencies $(\nu_r^{-1}, \nu_z^{-1}) = (22.2, 286)$ μs for 0.88 mK trap depth. Each data point in Figure 36 is the average over 100 runs of the experiment. In this case, the recapture rate is determined by the successful recapture events of single atoms instead of the total fluorescent signal. The results are compared to a Monte-Carlo simulation which indicates a temperature

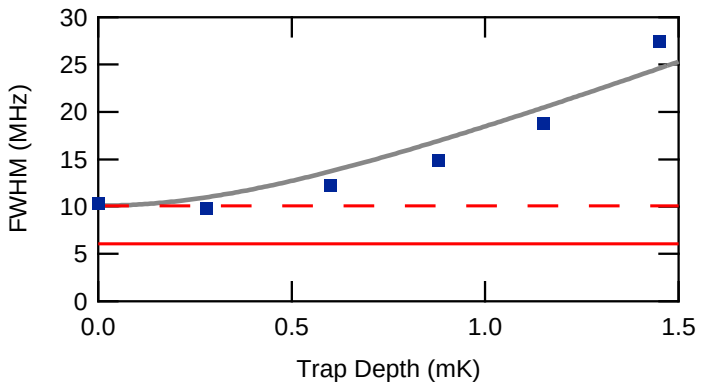

Figure 37: FWHM of the single-atom spectrum in different trap depths as shown in Figure 34(a). The red solid line is the natural linewidth of the ^{87}Rb $5S_{1/2} \leftrightarrow 5P_{3/2}$ transition and the red dashed line is the power broadened linewidth with probe intensity $I = 2I_{sat}$.

of 45 μK.

As shown in Figure 37, the transition linewidth broadens beyond the 6.07 MHz natural linewidth as the trapping potential increases. The linewidth is consistent with the power broadened linewidth at low trapping potential, which is 10.3 MHz for the probe intensity used in the experiment ($I = 2I_{sat}$). The increase of linewidth broadening is $\sim$15 MHz and cannot be explained by thermal Doppler broadening. A Doppler broadened linewidth of 10 MHz corresponds to thermal atoms with $\sim$100 mK in temperature, which is much larger than the trapping potential of the FORT. The source of this broadening stems from the spatial varying light shifts which is discussed in 2.8. As the atom moves in the trap, it experiences a range of light shifts. Using the energy distribution of the atoms determined from the temperature measurement, we can estimate the linewidth broadening of this effect. It also provides an explanation why our measured AC-Stark shifts are slightly smaller than predicted by the calculations. With the same temperature, the discrepancy between the measurement and the calculation of a specific transition is proportional to its own AC-Stark shift.

The FWHM of the Maxwell-Boltzmann energy distribution function $f(E)$ is given

in Eq. 2.55,

$$f(E)_{FWHM} = 2.02 \times k_B T.$$

Figure 33 shows that for the $|F = 2, m_F = 0\rangle \leftrightarrow |F' = 3, m_{F'} = 0\rangle$ transition, the shift for the transition is ∼71 MHz/880 μK. For atoms in 0.35 mK deep trap as shown in Figure 36, the temperature is 45 μK. The corresponding broadening is,

$$\text{linewidth broadening} = 2.02 \times 45\mu\text{K} \times \frac{71}{880}\frac{\text{MHz}}{\mu\text{K}} = 7.3 \text{ MHz}.$$

Along with the power broadened FWHM linewidth of 10.3 MHz, the final FWHM linewidth is about 12 MHz. As the trapping potential increases, the cooling laser (centered at −23 MHz from bare resonance) is further red detuned from the shifted resonance, resulting in reduced cooling efficiency.

5.8 Probe-Induced Heating

The loss mechanisms of the optically trapped neutral atoms include the collision with background molecules, parametric heating from the trap laser intensity fluctuation [136, 138], the heating from the radiation pressure during the detection process, etc. For our system, the 10^{-11} Torr background pressure and the stability of the trapping laser allow us to achieve trap lifetime greater than 100 seconds. On the other hand, continuous detection of optically trapped atoms with near resonant laser can heat the atoms out of the trap in far less than a second. Therefore, it is important to study the probe-induced heating and use this information to develop neutral atom qubits with long storage time. The experiments in this and the following sections are done before the implementation of the new single focus trap and hence are performed in the 1D optical lattice.

In order to study the heating mechanism of the probe beams induced on the atoms, we measure the temperature of the atoms in a 1D optical lattice after probing the atoms. After the initial loading of atoms into the 1D optical lattice, we use

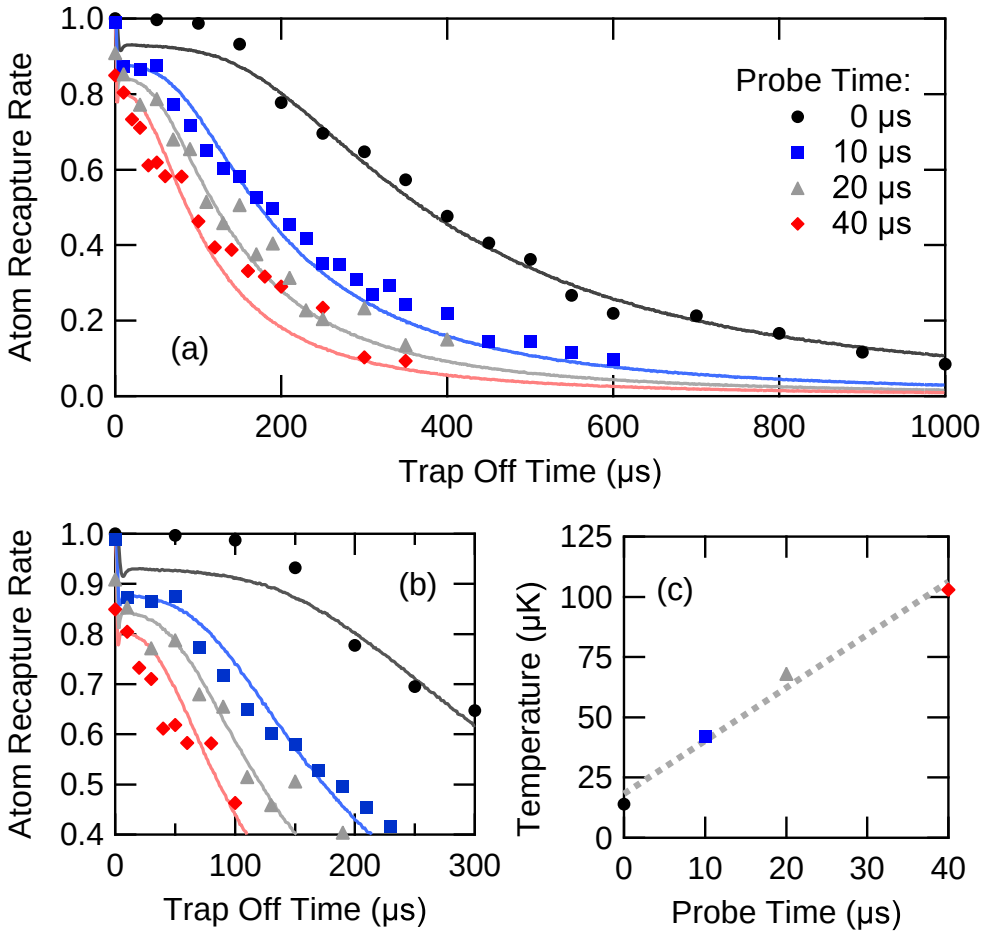

Figure 38: Temperature measurements of atoms in the 1D optical lattice with 1.5 mK trapping potential for studying the probe-induced heating. The probe intensity is $\simeq 0.5 I_{sat}$ and the probe detuning is +33.2 MHz from the bare resonance. The results are fitted to the Monte-Carlo simulation to determine the temperature of the atoms. (a) Temperature measurements for after atoms being probed for 0, 10 μs, 20 μs, and 40 μs. (b) Zoom in of (a) showing the first 300 μs. (c) The temperature of the atoms versus the probe time.

the camera to take a background subtracted image with 1 s exposure time. The MOT cooling beams are turned off 10 ms before applying probe laser for different durations, then the trap beam is switched off for a pre-determined time. Another background subtracted image is taken after the MOT cooling beams are turned back on to determine the atom recapture rate. For each data point in Figure 38(a), the fluorescent signal within the region of interest (9 by 32 pixels) is summed over 50 runs of the experiment to determine the atom survival rate. There are on average 10 atoms loaded in each run.

The trap beam has a measured 5 μs slow switch-off time due to the signal source (National Instruments PCI-6713) for controlling the AOM modulation source has a comparable switch-off time. In the single focus trap setup, it is replaced with a pulse generator (Berkeley Nucleonics Corporation Model 555) so that the switch-off time is limited by the optical rise and fall time of the AOM (200 ns).

The drop and recapture rate of atoms in the 1D optical lattice is plotted in Figure 38(a). The data is fitted to the Monte-Carlo simulation and the heating rate of the atoms due to the probe beams is plotted in Figure 38(c); the straight line fit has a slope of 2.2 μK/μs. The power of the probe beams are 1.38 μW and the detuning of the probe is +33.2 MHz from the bare resonance. The average count rate measured with the SPCM for these probe and trap parameters is 6 cts/ms, which corresponds to photon scattering rate of

$$\begin{aligned}\text{photon scattering rate} &= \frac{\text{detected count rate}}{\text{total collection efficiency}} \\ &= \frac{6\ \frac{\text{cts}}{\text{ms}}}{0.45\%} = 1.3\ \frac{\text{photon}}{\mu\text{s}}.\end{aligned}$$

Hence the average heating rate is 1.7 μK per scattering event. For comparison, with a perfectly balanced pair of counter-propagating beams, the average energy increase for each photon absorption and re-emission event is twice the recoil energy [113], which is 2×362 nK. The additional heating could come from the imbalanced probe beams

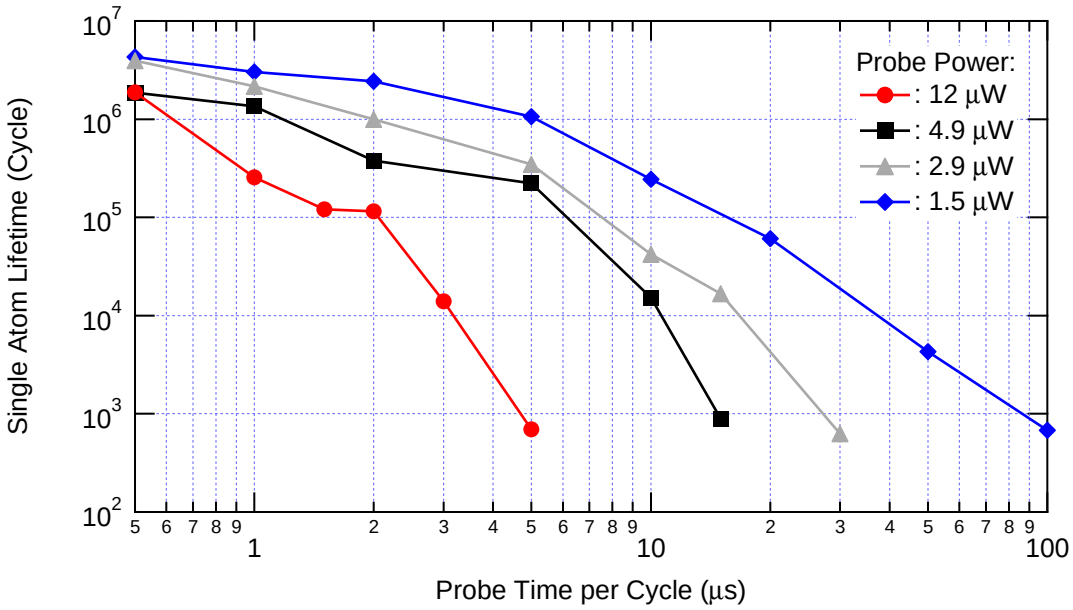

Figure 39: Plots of the single atom lifetime (in cycle) versus the probe time in each cycle. The probe detuning is 33.2 MHz from the bare resonance.

pair or if the actual photon collection efficiency is lower than the estimated value used in the calculation.

As shown in Figure 38(b), the recapture rates drop by ∼10% within the first 10 μs and continue to decay at a different rate. This results from highly anisotropic trapping geometry for the 1D optical lattice. The ratio of the high and the low trap frequencies is 60 for the 1D optical lattice and 13 for the single focus trap. With the same kinetic energy, it is easier for the atoms to escape from the trap along the tight confinement axis, the trap beam direction in 1D optical lattice and radial direction in single focus trap, during the trap off time.

With the knowledge of probe-induced heating, we will study the relation between trapped atom lifetime and the probe time per cycle in the following section.

5.9 Single Atom Trap Lifetime vs Data Acquisition Time

In Section 5.3, the gated probing/cooling technique was introduced. The cycle time and the probe time within each cycle is chosen such that the photon scattering for

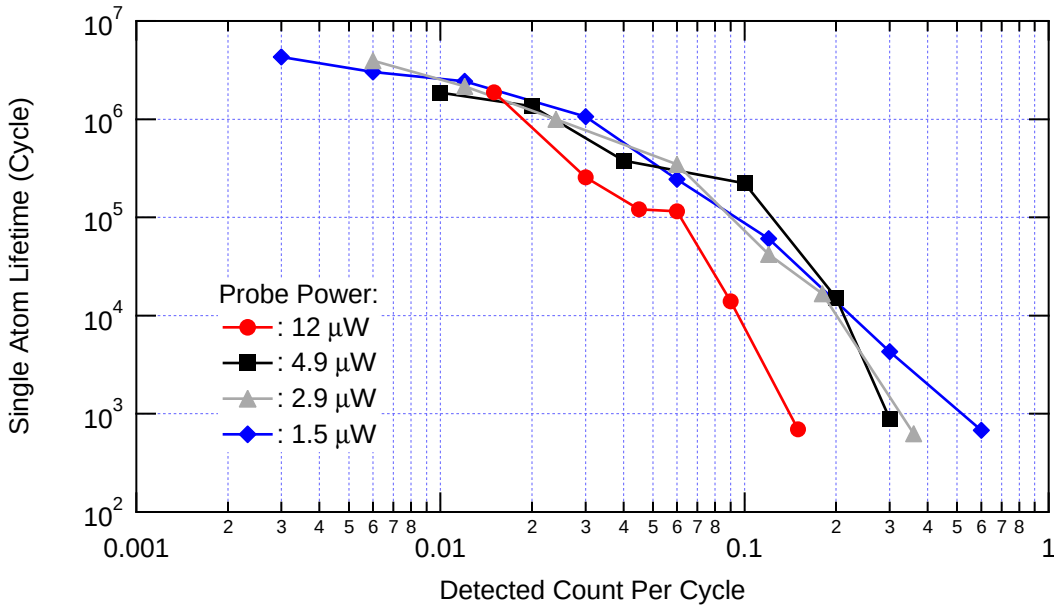

Figure 40: Plots of the single atom lifetime (in cycle) versus the detected count per cycle.

the chosen probe time does not heat the atom out of the trap, and the cooling time is sufficiently long for the cooling beams to recool the atoms. For example, in the previous section, the probe-induced heating measurements suggest each photon scattering event heats up the atom by 1.7 μK. Without cooling, a single atom in a 1 mK trap can scatter at most 590 photons before leaving the trap. It is important to maximize the probe time per cycle without significantly reducing the trap lifetime.

Figure 39 shows the plots of the single atom lifetime in a 1.1 mK trap versus the probe time in each cycle for various probe power. The cycle time ranges from 50 μs to 4 ms to ensure that the atoms are cooled to the bottom of the trap. Due to the various cycle time used in these measurements, the trap lifetime is expressed in the number of probing/cooling cycles instead of in the unit of time. For low probe power, it is possible to keep the single atoms for nearly 1000 cycles with 100 μs probe time.

In the above measurements, the single atom count rates for different probe power settings are, (12, 4.9, 2.9, 1.5) μW = (30, 20, 12, 8) cts/ms, respectively. Figure 40 shows the single atom lifetime versus the detected counts per cycle. As stated earlier,

a trapped atom cannot scatter more photons than that which the corresponding heating exceeds the trapping potential. Therefore, the single atom lifetime should be closely related to the total number of scattering events (or detected counts) per cycle instead of probe power or probe time per cycle. In the figure, the black, gray, and blue curves collapse rather closely to each other, which supports the above hypothesis.

5.10 Summary

In summary, we measured the m_F state dependent AC-Stark shifts with different polarizations of probe beams with single atoms in the single focus trap. The calculation of the AC-Stark shifts for the $F = 2 \rightarrow F' = 3$ transitions agrees well with the spectrum measurements of single atoms in the FORT. The trapping environments and the heating due to the probing process are also characterized for atoms in the trap, which can be used to guide future experiments with single atoms in the optical dipole traps.

CHAPTER VI

DYNAMICS OF CAVITY LIGHT FIELD IN A DUAL LATTICE CAVITY QED SYSTEM

In this chapter, I will discuss our experimental demonstration of deterministic delivery and selective addressability of single atoms to an optical cavity. I will also discuss a second experiment that couples atoms in dual quantum registers to an optical cavity. In the latter case, rubidium atoms are loaded into two independently controlled optical lattices, and the dynamics of the cavity mediated interaction are explored with this dual-conveyor cavity system.

6.1 Neutral Atom Register

The preparation and coupling of quantum registers to a cavity mode is a promising technology for the experimental realization of proposals for quantum computing [140, 141] and probing novel quantum phases [142]. In early experiments, loading atoms into the cavity is done in a probabilistic manner; either from free-falling laser-cooled atoms initially prepared in a magneto-optical trap (MOT) [58], or transferred atoms from a MOT using an optical dipole trap with unknown number of atoms [54, 67]. Deterministic loading of single atoms to the cavity and the precise control of these single atoms are required for some practical applications, and these are demonstrated by loading and transferring single atoms from a single-atom MOT [55]. Here we present an alternative route: load the optical dipole trap from a MOT with unknown number of atoms, bring these randomly distributed atoms through the cavity, use the time stamp of the signal to determine the positions of the atoms, and move the desired atom(s) back to the cavity on demand. This technique can be expanded to

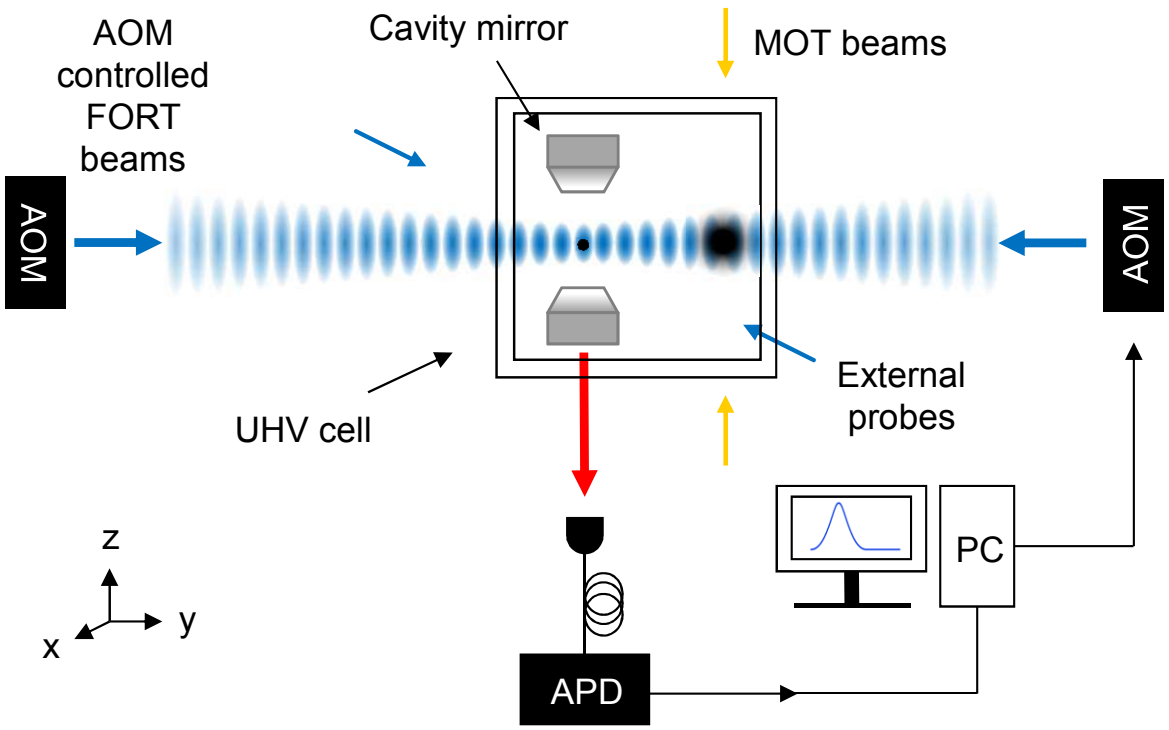

Figure 41: The schematic of the experiment. For simplicity, only one pair of MOT beams are shown in the figure, the other MOT beams lie on the x-y plane.

multi-conveyor coupled to a cavity and represents an important step towards scalable quantum information processing designs [143, 144].

6.1.1 Experimental Setup

The experiment begins with capturing and laser cooling ^{87}Rb atoms in a MOT. The laser cooled atoms are loaded into an optical conveyor [25] and transported to a cavity situated 3.2 mm away from the MOT. Figure 41 shows an illustration of the experimental setup. The MOT has a six-beam configuration with powers of 4 mW per beam and a diameter of 12 mm. The MOT is operated with a magnetic field gradient of $\sim$5 G/cm in order to sparsely load the atoms over half a millimeter in the optical dipole trap. In this section, only one of the lattices is used.

The far-off resonant trap (FORT) consists of two counter-propagating beams from a fiber laser operating at $\lambda = 1064$ nm. The foci of the lattice beams are located at the cavity, with a waist of 18 μm and optical powers of 2.5 W each, providing a

trap depth of $U/k_B = 2.1$ mK at the cavity and 170 μK at the MOT. The dipole trap beams are controlled by two phase-locked acousto-optical modulators (AOMs). When the frequencies of the two beams are the same, they create a stationary standing wave trap for atom storage. However, when a frequency difference is induced between the two AOMs, the resulting traveling wave forms an atomic conveyor lattice with submicron precision [55, 145], which can deterministically transport the atoms from the MOT to the cavity. The speed of the traveling wave is related to the frequency difference $\Delta\nu$ by,

$$v = \frac{\lambda \Delta\nu}{2}.$$

By inducing a 5 kHz frequency difference between the lattice beams, the atoms are transported towards the cavity with a velocity of 2.67 mm/s.

The atoms are moved 2.6 mm from the MOT and stopped about half a millimeter from the center of the cavity. They are then brought slowly through the cavity mode at a velocity of $1 \sim 5$ mm/s. In order to individually resolve the atoms, two probe beam pairs with a Rabi frequency of $\frac{\Omega}{2\pi} = 10$ MHz per beam are set to excite the atoms as they enter the cavity mode. Each probe consists of two frequencies, a pumping light locked 8.9 MHz red-detuned from the $F = 2 \rightarrow F' = 3$ transition of ^{87}Rb and a repumping light locked to the $F = 1 \rightarrow F' = 2$ transition to pump the atoms out of the $F = 1$ dark state. The two probe beams are focused at the cavity with a 60 μm waist and counter-propagate in a lin $\perp$ lin polarization configuration that allows the atoms to experience constant illumination, independent of position. With the combination of the probe, the AC-Stark shift due to the FORT, and the enhanced emission into the cavity mode, the atoms experience cooling when situated inside the cavity mode [146].

The cavity used in this experiment is constructed from two superpolished concave mirrors with the same radius of curvature (R = 2.5 cm) separated by 500 μm as shown in Figure 42. The cavity mirrors have transmission losses of 8 ppm and 100 ppm, so

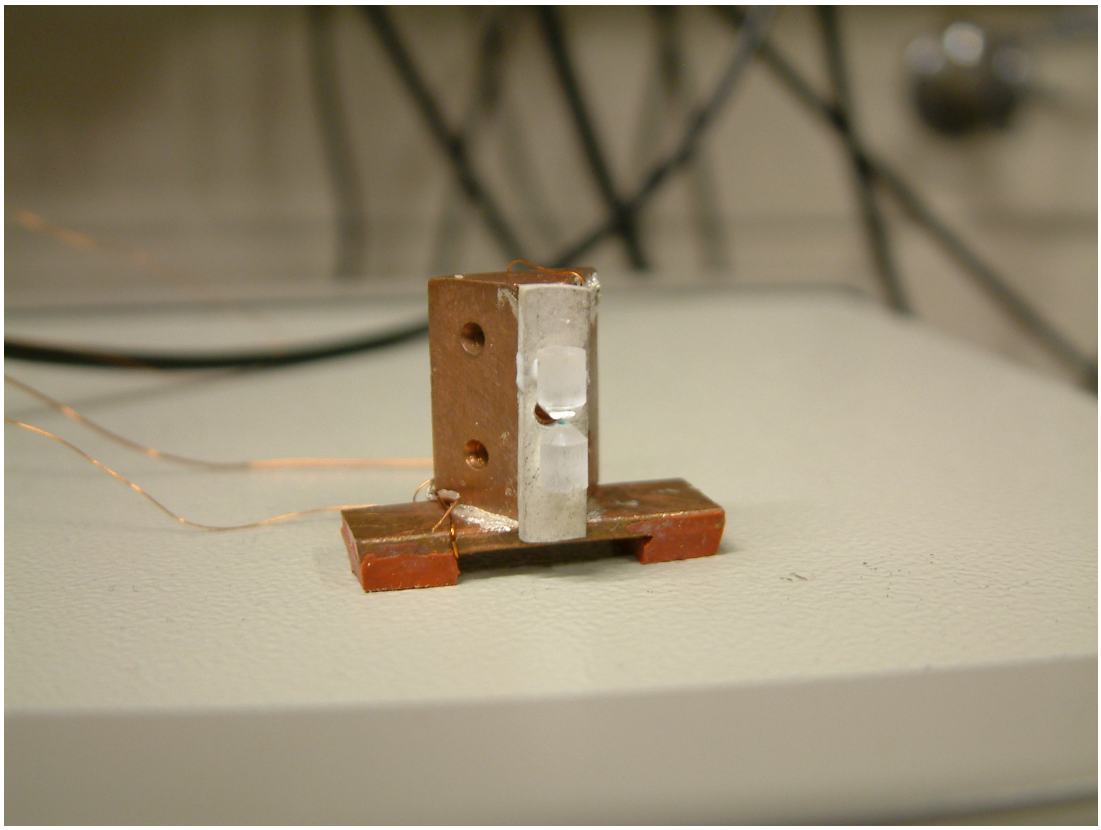

Figure 42: A close up picture of the cavity. The mirrors are coned down from a 3 mm diameter to a final surface diameter of 1 mm, which is machined from a 7.75 mm diameter mirror. The cavity mirrors are glued on to a piezo ceramic and separated by 500 μm.

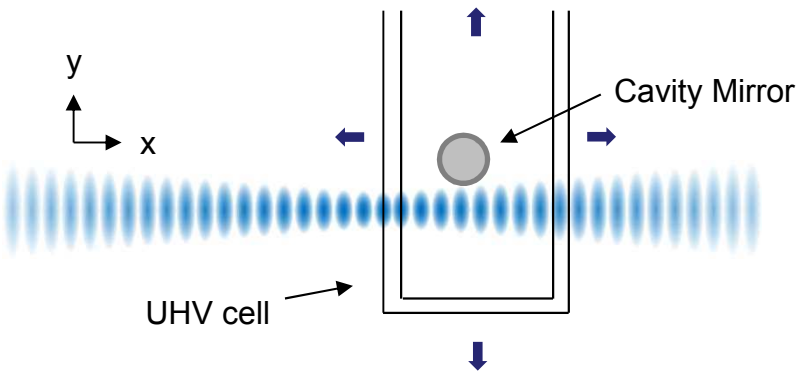

Figure 43: The top view of Figure 41 with one lattice and the cavity (gray circle) shown. The cavity position can be adjusted in the x-y plane (along the blue arrows directions) with the two 1D translation stages for maximizing the atom-cavity coupling rate.

that the photons escaping the system from the 100 ppm side is 12.5 times as much of the other side, making it a one-sided cavity. For cavity length control, the mirrors are glued on a piezo ceramic using Varian Torr Seal. A hole with ∼2 mm diameter is drilled at the center of the piezoceramic for the dipole trap laser beams to go through. The cavity TEM_{00} mode has a waist of 25 μm, and the total measured losses are 300 ppm. The vacuum chamber is mounted on a 1D translation stage which is mounted on another 1D translation state; it allows us to adjust the cavity position with respect to the FORT beams foci as shown in Figure 43. The overlap between the cavity mode and the lattice beams has to be optimized for maximizing the atom-cavity coupling rate.

For this system, the cavity QED parameters are $\frac{1}{2\pi}(g_0, \kappa, \gamma_\perp) = (9.3, 7.0, 3.0)$ MHz, respectively, where g_0 is the maximum atom-cavity coupling rate, κ is the decay rate of the cavity, and $\gamma_\perp$ is the transverse decay rate of ^{87}Rb. From Eq. 3.10 the single atom cooperativity of this system is $C_1 = 2.8$, hence the system operates in the intermediate coupling regime. The cavity is locked on resonance with the $F = 2 \rightarrow F' = 3$ transition via an off-resonant beam ($\lambda = 784$ nm) that is locked to the 780 nm laser via a transfer cavity. The transfer locking technique is described in

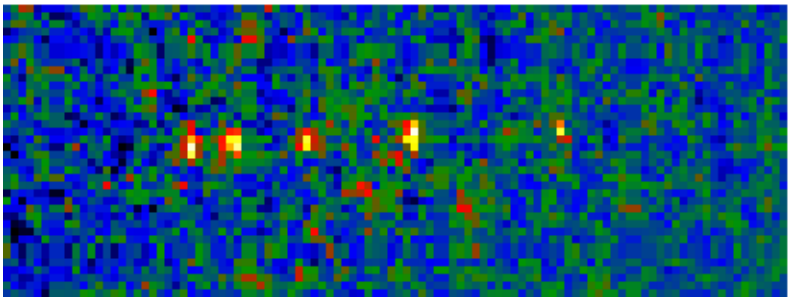

Figure 44: An background subtracted image of five atoms in the optical lattice taken in a different system. The pixel size is 2.5 μm by 2.5 μm. The two atoms on the very left are separated by 10 μm.

detail in [118, 119].

In order to separate the different wavelengths in the output of the cavity, a narrowband laserline filter is used such that the 784 nm locking light is reflected and the 780 nm atomic signal passes with 99% efficiency. The 784 nm light is fibercoupled into an optical heterodyne system to produce a locking signal. Then the 780 nm light is filtered once more with another narrowband laserline filter with 99% efficiency before it is fibercoupled into a single photon counting module (SPCM) for photon counting. As the atoms enter into the cavity mode and are excited by the external probe beams, the SPCM detects the scattered photons from the passing atoms with a total efficiency of 20%. This efficiency accounts for a 50% quantum efficiency of the SPCM and 40% efficiency from fiber coupling and transmission losses.

6.1.2 Experimental Results

Due to the method used to load the atoms into the optical dipole trap, the atoms are randomly distributed in the optical lattice. The neutral atom register is slowly scanned through the cavity mode in order to separately detect single atoms. For the case that the separation between adjacent atoms is less than twice the cavity mode waist ($\sim$50 μm), we will not be able to resolve them. To avoid this, the loading time of the MOT is set to $2 \sim 5$ seconds with gradient field of $\sim$5 G/cm so that the atom density in the MOT is low and the atoms are sparsely loaded in the optical lattice.

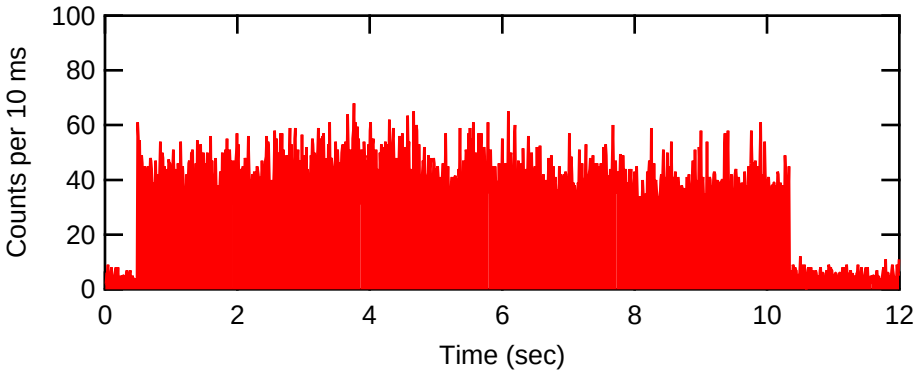

Figure 45: Single atom in the cavity with continuous observation about 10 seconds. The Rabi frequency is 19 MHz, the probe beam detuning is -8.9 MHz, the cavity detuning is -2 MHz, and the AC-Stark shift is $\sim$130 MHz.

Figure 44 is an image of five atoms randomly distributed in an optical lattice. The image is taken in a different 1D optical lattice setup with higher numerical aperture imaging system (Mitutoyo Corp. Plan Apo NIR Infinity-Corrected $20\times$, NA $= 0.4$) for the purpose of showing the randomness of loading process. In the cavity experiment, the restricted optical access makes it difficult to use the same imaging optics, hence a microscope objective with longer working distance (37.5 mm) and lower numerical aperture (Mitutoyo Corp. Plan Apo NIR Infinity-Corrected $5\times$, N.A. $= 0.14$) is used instead. The lower photon collection efficiency and the stray light scattering off the cavity mirrors make it impossible to detect single atoms using the camera.

Figure 45 shows a single atom delivered to the cavity via probabilistic loading and continuously observed for 10 seconds before lost from the trap. Once the atom is transferred to the cavity, it is excited by two counter-propagating external probe beams. For cavity frequency greater than the probe laser frequency, $\omega_c - \omega_p = \Delta_c - \Delta_p > 0$, an atom absorbing a photon from the external probe lasers and emitting it into the cavity mode causes the atom to lose energy. Continuous observation of atoms in the cavity with long lifetime is realized with this cavity-assisted cooling [54].

Deterministic loading of single atoms to the cavity have been demonstrated [55]. In this deterministic single atom loading scheme, only one single atom can be used

for each run of the experiment, which prohibits the possibility of realizing multi-qubit operation in a cavity. Here we present a technique to identify the randomly distributed atoms in the optical lattice and bring the desired atoms back on demand. In this fashion, multiple single atoms in the optical lattice can be coupled to the cavity one after another in a controlled manner, providing a promising route for realizing complex and scalable quantum information experiment designs.

Real time analysis of the cavity output signal in the course of lattice movement allows us to determine the position of a specific atom and move it back into the cavity mode on demand. We show this process in Figure 46. In (a), four atoms in the lattice are initially brought through the cavity mode with a velocity of 2.67 μm/ms. It can be seen that the second atom is 190 μm past the first atom and the third atom is 190 μm past the second atom. Finally, the last atom is 240 μm further away from the third atom. For the deterministic return, we focus on the first atom that entered the cavity mode. The position of the atom of interest is derived by measuring how much time the atom continued to travel in the optical trap after it was seen in the center of the cavity mode. Using this information, we can bring the desired atom back and continuously observe it in the cavity, as shown in (b). It is clear that the correct atom is addressed because the other three atoms are detected as they go through the cavity mode in the process of bringing the first atom back. For (c) and (d), the lattice speed is 1.60 μm/ms and the program is pre-coded such that, upon detecting 2 or more atoms, the lattice will bring the last atom back to the cavity mode and detect for 0.5 seconds, then it will bring the first atom to the cavity mode for continuous observation. The separation between these two atoms is 560 μm.

The success rate of bringing two atoms back to the cavity one after another as shown in Figure 46(c) and 46(d) is 5%. The failure comes from atom losses after the initial scanning and the distribution of atoms in the lattice, either too dense to resolve individual atoms or no atom at all in the scanning region. The atom losses

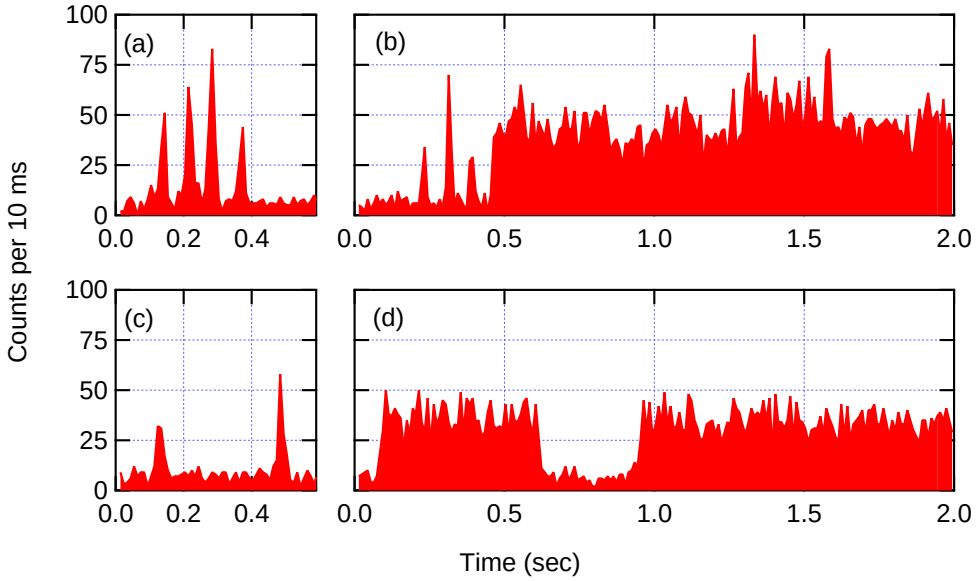

Figure 46: Deterministic selectivity of atoms in a register. In (a), four atoms are initially swept past the cavity mode with a velocity of 2.67 μm/ms. The atom of interest is located at 150 ms, the first atom that went through the cavity mode. The position of the first atom is obtained by determining the time stamp of the corresponding peak signal, then the atom is returned back to the cavity and continuously observed in (b). As the first atom was brought back to the cavity, the other three atoms are detected as they passed through. The cooling beams were -8.9 MHz detuned from the $F = 2 \rightarrow F' = 3$ transition with a Rabi frequency of 19 MHz, and the cavity was 2 MHz detuned from the $F = 2 \rightarrow F' = 3$ transition. In (c) and (d), the lattice speed is 1.60 μm/ms. The program is pre-coded such that, upon detecting 2 or more atoms, the lattice will bring the last atom back to the cavity mode and detect for 0.5 seconds, then it will bring the first atom to the cavity mode for continuous observation. The success rate for this operation is around 5%.

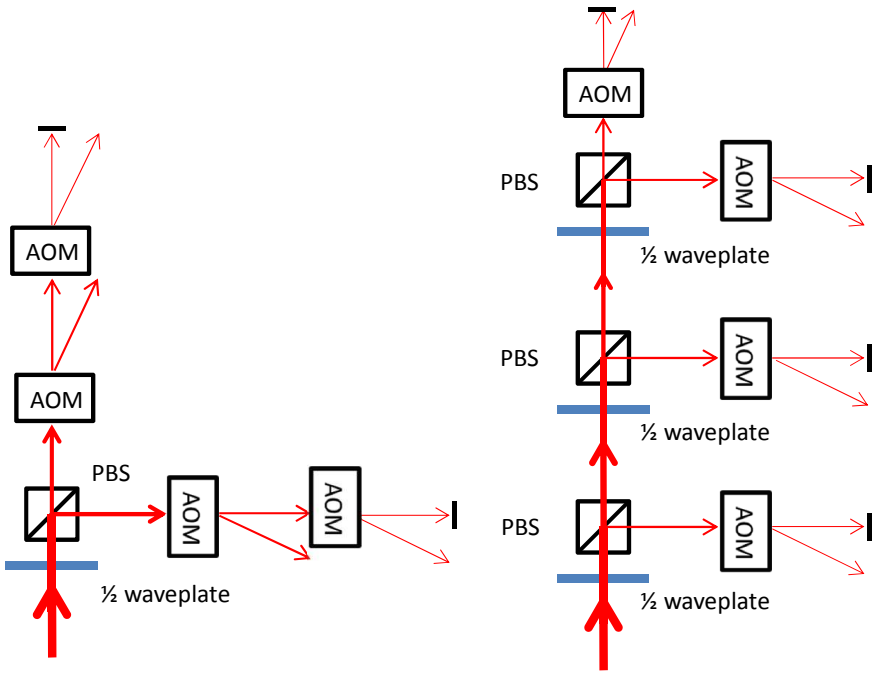

Figure 47: Illustrative diagram of two different methods used to distribute optical power for dual lattice setup.

could be improved by increasing the trapping potential of the lattice. The latter can be improved by increasing the MOT size (originally ~0.5 mm^3), scanning range, and trapping potential. Together, more atoms will be loaded into the lattice across more lattice sites, resulting a higher chance of getting resolvable single atoms.

6.2 Dual Conveyors

In this section, we will explain the experimental approach for adding a second atom conveyor to the system and demonstrate the coupling of atoms in two independent optical conveyors to the same cavity. With the ability to selectively address the desired atoms of each lattice in a dual lattice system, several quantum information protocols can be realized [143, 144]. It also allows us to study the cavity-assisted interaction between the independently controllable atoms. The experiment results are compared to the semi-classical model developed in Chapter 3.

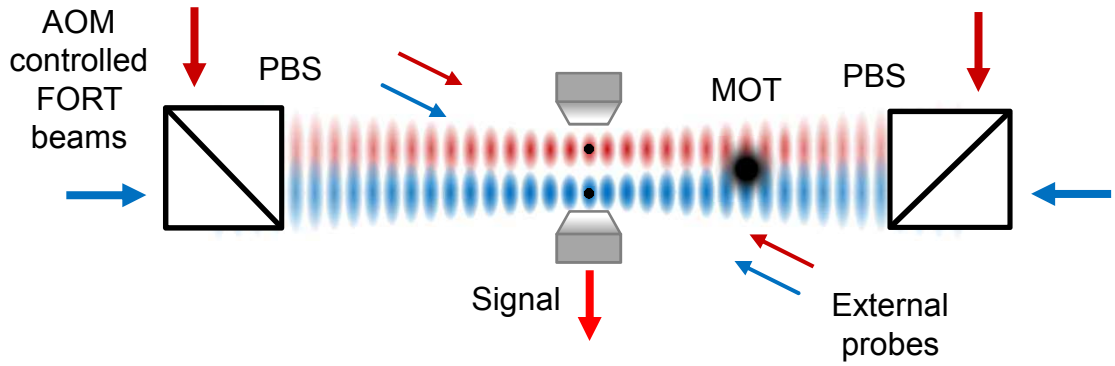

Figure 48: Illustrative diagram of the dual lattice cavity system. The two lattices are separated vertically by 150 μm at the cavity.

6.2.1 Experimental Setup

In order to change the system from a single atom register conveyor to a dual conveyor system, two different approaches have been taken to distribute the available optical power for the FORT beams as shown in Figure 47. In the first attempt, the zeroth order beams of the first AOMs are recycled to produce the other two necessary beams. In the second attempt, the initial fiber laser beam is split into four beams with half waveplates and polarizing beamsplitters (PBS) before sending through AOMs. In the first scenario, less optical power goes into the unused zeroth beams in the very end, at the expense of beam profile quality. The second method yields less power but better beam profile. The second method is used because it is easier to create two lattices with relatively close trapping potentials in this way. In both cases, the FORT beams have opposite polarization for different lattices, ensuring that the two traps do not interfere. This also allows us to combine the FORT beams using PBS with minimal losses.

An additional pair of probe beams are constructed for the second lattice with shutter controlled pumping and repumping lights. This allows us to excite atoms in both lattices, or only excite atoms in one lattice and shine repumping light on atoms in the other lattice to keep them out of the $F = 1$ dark state. In this case, atoms in the second lattice are not directly driven by the external probe lasers, instead, they

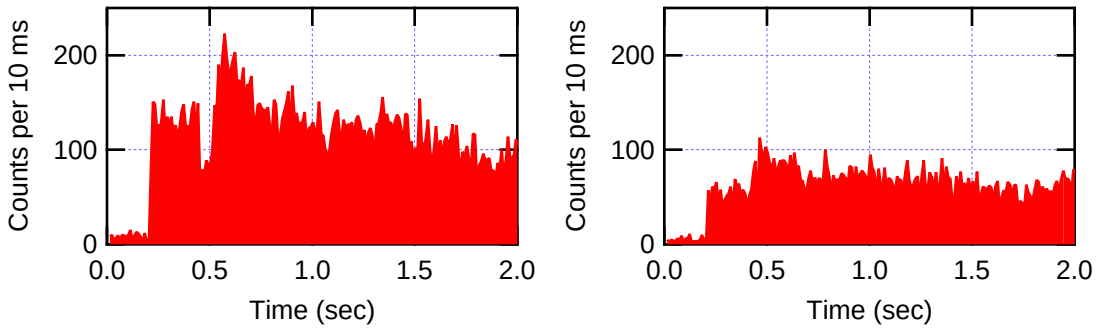

Figure 49: The change of the cavity output when the second lattice brings atoms into the cavity at 450 ms. For both figures, the number of atoms in each lattice is less than three. The cavity detuning is -4 MHz and the probe beam detuning is -8.9 MHz.

are driven by the cavity photons. The latter scheme is fundamentally different from a multi-atom-cavity system with only one optical dipole trap and one external probe lasers. An illustrative diagram of the dual lattice cavity system is shown in Figure 48. The two lattices are separated vertically by 150 μm at the cavity, sufficiently apart so that the probe beams excite atoms only in one of the lattices (probe beam waist = 60 μm). The atoms are loaded simultaneously from the MOT, but each lattice has independent translational control.

6.2.2 Dual Registers with A Cavity

In Section 6.1.2, the delivery of the desired atoms to the cavity is performed and the results are shown in Figure 46. In order to perform the proposed schemes for the controlled-Z, controlled phase-flip and Hadamard gate operations, a dual lattice system with two atoms in each lattice is required [143, 144]. As shown in Figure 46(c) and 46(d), the success rate of deterministically bring back two atoms, one after another is 5%. Therefore, the success rate of having two conveyors performing this task is 0.25%, making it impractical to test the above schemes before improvements are made to this technique. Hence we began to study the interaction between atoms in these two independently controllable lattices with the current system.

In the experiment, the first lattice brings atoms to the cavity with its dedicated

probe beams on, and continuously observe the atoms for a period of time and the second lattice brings more atoms to the cavity with only repump beams on. The probe beams for the lattices are separated by 150 μm and there is no cross addressing of atoms in the wrong lattice. Figure 49 shows the response of the cavity signal as the second lattice brings atoms to the cavity. It is peculiar that the cavity signal could either increase or decrease when the second lattice brings atoms to the cavity. In the rest of the chapter, we will focus on the study of this interaction and compare the results to the semi-classical model developed in Chapter 3.

In the following, we will refer to the two lattices as L1 and L2. In order to study the dynamics of the cavity photon field when L2 brings atoms into the cavity mode, the experiment is done with fixed probe beam detuning and various cavity detuning. Each lattice has $5 \sim 15$ atoms in the cavity mode on average. L1 brings atoms in with its dedicated pumping and repumping laser turned on, L2 brings in atoms 500 ms later with only repumping laser turned on. The atoms in L2 are indirectly excited by the cavity photons. Due to the lack of external probe beams and the subsequent three dimensional cooling, atoms in L2 have much shorter lifetime compared to atoms in L1. As atoms in L2 gradually leave the trap, the cavity output signal changes accordingly. In Figure 50 we show results at three different cavity detuning. The response of the cavity field depends on the cavity detuning and the number of atoms in L2. In Figure 50(a), as L2 brings atoms into the cavity mode, the cavity output signal drops significantly and as the atoms leave L2, the cavity signal resumes its original level. In Figure 50(b), the cavity output signal initially goes down as L2 brings in atoms and goes back up and exceeds the original level as the atoms leave L2. After all atoms in L2 are gone, the cavity output signal resume its original level. In Figure 50(c), the cavity signal goes up as L2 brings in atoms and goes back to its original level as atoms left L2.

In order to explain result shown in Figure 50, we use the semi-classical Hamiltonian

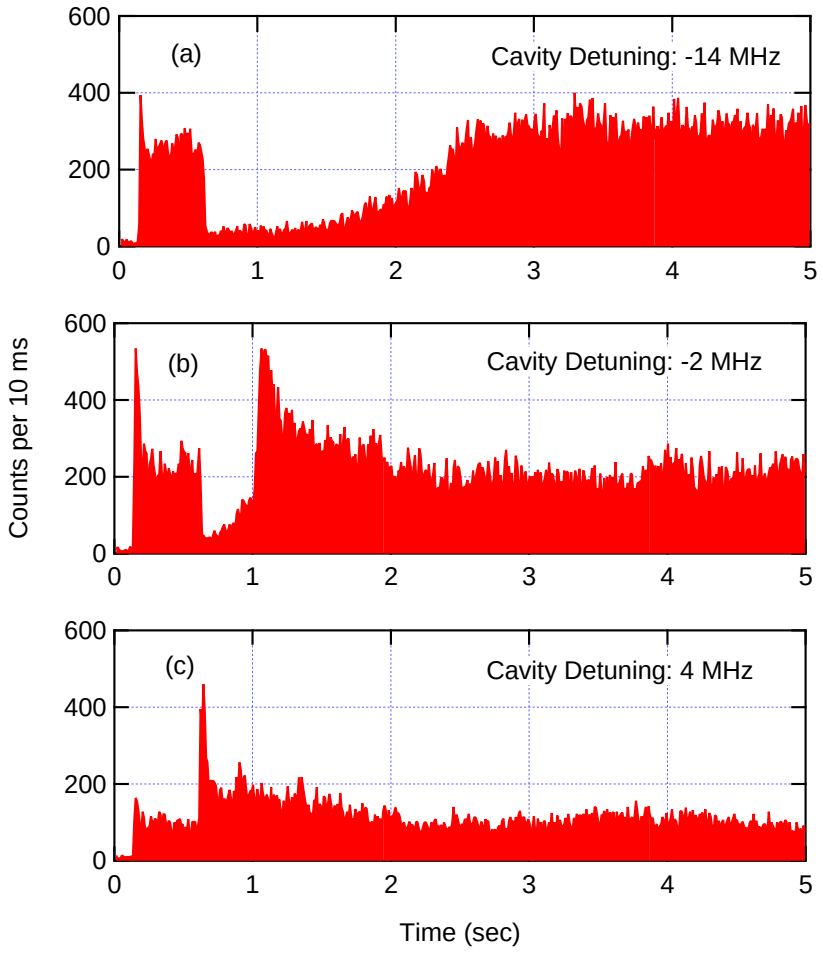

Figure 50: The change of the cavity output when the atoms in L2 enter/leave the cavity mode under different cavity detuning, (a) -14 MHz (b) -2 MHz (c) 4 MHz and the probe beam detuning is -8.9 MHz. With sufficient cooling, atoms in L1 typically have lifetime over 10 seconds unless the cavity detuning is near resonant. Indirect cooling for atoms in L2 greatly reduces the lifetime to less than 2 seconds for most of the cavity detuning.

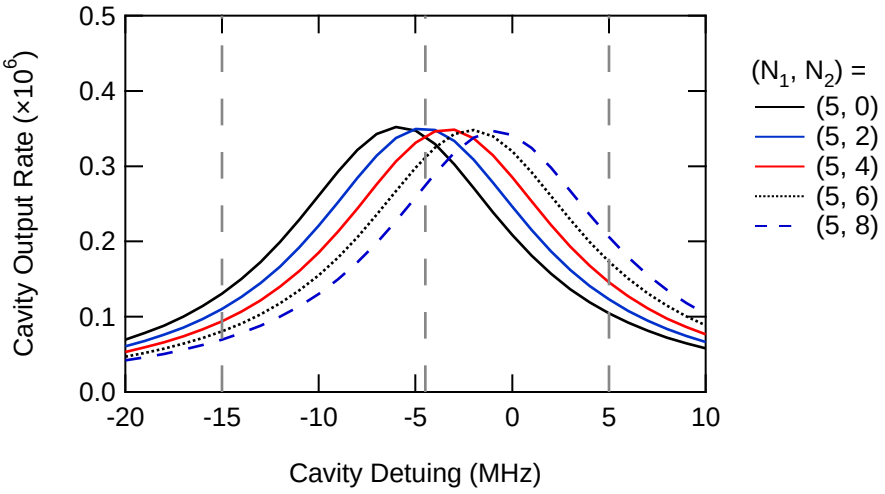

Figure 51: Calculation of the cavity output spectrum with different number of atom in L2 using semi-classical Hamiltonian. The parameters used in the calculation are, AC-Stark shift = 130 MHz (2 mK trap depth), $\frac{\Omega}{2\pi} = 6.7$ MHz, and $\frac{\Delta_p}{2\pi} = -8.9$ MHz.

described in Section 3.3.2,

$$\begin{aligned} H_{sc} &= (\Delta_1 - \Delta_p)\hat{\sigma}_{N_1+}\hat{\sigma}_{N_1-} + i\sqrt{N_1}g_0(\hat{a}^\dagger\hat{\sigma}_{N_1-} - \hat{\sigma}_{N_1+}\hat{a}) + \sqrt{N_1}\Omega(\hat{\sigma}_{N_1+} + \hat{\sigma}_{N_1-}) \\ &\quad +(\Delta_2 - \Delta_p)\hat{\sigma}_{N_2+}\hat{\sigma}_{N_2-} + i\sqrt{N_2}g_0(\hat{a}^\dagger\hat{\sigma}_{N_2-} - \hat{\sigma}_{N_2+}\hat{a}) + (\Delta_c - \Delta_p)\hat{a}^\dagger\hat{a}, \quad (6.1) \end{aligned}$$

where Ω is the Rabi frequency of the external pumping light, Δ_p and Δ_c are the pumping light and cavity detuning from the bare atom $F = 2 \rightarrow F' = 3$ transition, respectively. N_1 and N_2 are the number of atoms in each lattice, Δ_1 and Δ_2 are the AC-Stark shift for atoms in the corresponding optical dipole trap. $\hat{\sigma}_+$ and $\hat{\sigma}_-$ are the raising and lowering operator for the atom, $\hat{a}^\dagger$ and $\hat{a}$ are the creation and annihilation operator for the photons in the cavity mode. Figure 51 is a plot of the cavity output signal versus the cavity detuning with 5 atoms in L1 and different numbers of atoms in L2. The vertical gray dashed lines mark the regions that correspond to the three different types of signal seen in Figure 50 as atoms in L2 leave the trap. With constant number of atoms in L1, the increasing number of atoms in L2 shifts the peak to the higher cavity detuning with nearly constant height. On the other hand, changing the number of atoms in L1 will shift the peak as well as the peak height. Hence the results shown in Figure 50 is unique to the cavity system with two independently

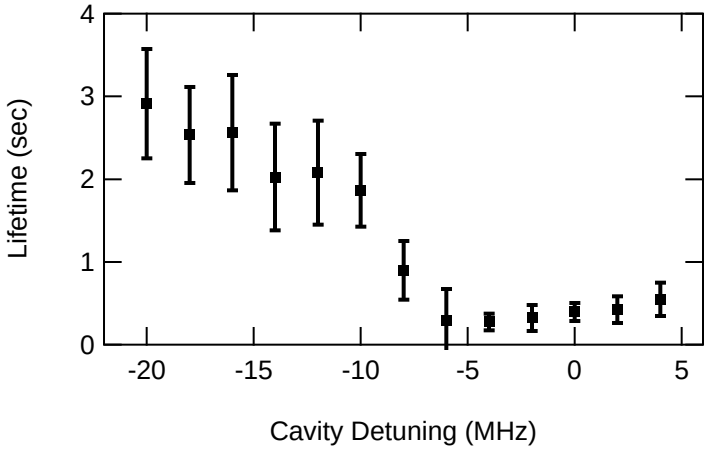

Figure 52: Lifetime of atoms in L2 that is indirectly cooled by the cavity photons.

addressable lattices.

The experiment is repeated 100 times at each cavity frequency ranging from -24 MHz to 4 MHz with increment of 2 MHz. The probe laser frequency and its intensity is the same throughout the experiment. The lifetime of atoms in L2 is shown in Figure 52. The signal level from atoms in L1, the ratio of signal after to before L2 brings atoms to the cavity, is shown in Figure 53. As stated earlier, the lack of cavity cooling makes the atoms in L2 have much shorter lifetime compared to the atoms in L1. For atoms in L1, absorbing a photon from the external probe and emitting it into the cavity mode cools the atom if the probe laser detuning is lower than the cavity detuning; absorbing a photon from the external probe and emitting it out of the cavity from the side also cools the atom if the probe laser frequency is less than the light shifted resonance frequency. On the other hand, atoms in L2 only absorb cavity photons, therefore the cooling and heating mechanisms are different from the atoms in L1. Qualitative analyses of these two mechanisms for atoms in L2 are presented below.

For atoms in L2, the absorption of cavity photons and re-emission back into the cavity mode does not cool the atoms since the energy of the absorbed and emitted photon have the same energy. For every absorption or emission event, the atom gains

a momentum of $\hbar/\lambda_c$ in either direction with equal opportunity (λ_c is the wavelength of the cavity photon). This is a one-dimensional random walk in the momentum space and the rms deviation of the momentum distribution after N_{ev} absorption and emission events is $\sqrt{N_{ev}}\hbar/2\lambda_c$. Therefore, this repeated cavity photon absorption and emission process heats up the atom in L2 and the heating rate is proportional to the cavity photon number, which scales linearly as the cavity output signal. In the experiment with about 10 atoms in L1, the cavity signal is at maximum for cavity detuning around -5 MHz, which corresponds to the maximum heating rate and the shortest lifetime for atoms in L2.

In our experiment, the rate of photon emitted into the cavity mode is $\frac{2g_0^2}{\kappa+\gamma_\perp} = 8.2$ MHz [44] and the rate emitted out of the cavity mode is $\frac{\gamma_\perp}{2\pi} = 3.0$ MHz. In this intermediate coupling regime, the photon emitted into modes other than the cavity mode are not negligible and have to be taken into account as well. The emitted photons from the light shifted atoms are $\sim$130 MHz with respect to the bare atomic resonance for 2 mK trapping potential and the absorbed photons from the cavity mode with cavity detuning around -10 MHz. Therefore, an atom absorbing a cavity photon and emitting it out of the cavity causes the atom to lose energy. The competition between the heating and cooling effects give rise to the observed lifetime for atoms in L2 as shown in Figure 52, where the heating is dominant with cavity detuning around -5 MHz.

The semi-classical Hamiltonian qualitatively shows the dynamics of the cavity field as the number of atoms in the indirectly cooled lattice changes accordingly. Figure 15(a) shows the spectrum of the cavity output signal with different number of atoms in L2 using Monte-Carlo simulation and the semi-classical Hamiltonian. In Figure 53, we present data fitted with the results of calculation obtained from the semi-classical Hamiltonian. The parameters used in the calculation are, AC-Stark shift = 130 MHz (corresponds to 2 mK trap depth), $\frac{\Omega}{2\pi} = 6.7$ MHz, and $\frac{\Delta_p}{2\pi} = -8.9$

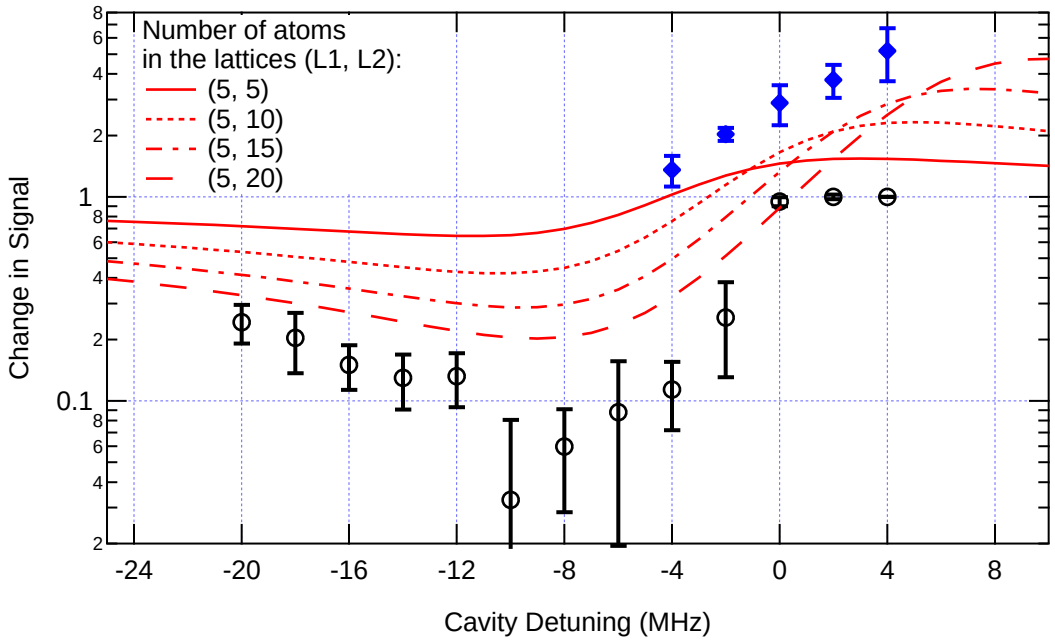

Figure 53: The results of the experiment fitted to the calculation with semi-classical Hamiltonian. The data is obtained by averaging over the ratio between the signal level when L2 brings in atoms and the signal level with only atoms in L1 stays in the cavity mode. For cavity detuning in-between -4 and 4 MHz, the initial drops in the signals when L2 brings atoms into the cavity are shown as black circles. As the atoms in L2 decreases, the signals increase above the original level and the overshoots are shown as blue diamonds.

MHz. There are 5 atoms in the lattice directly cooled by the external probe beams, and the 4 different curves in Figure 53 represent (5, 10, 15, 20) atoms in the other lattice, respectively.

The discrepancy between the calculation and the results of the experiment stem from the number of atoms in L1 and L2 are not the same for each run, and the number of atoms used in the calculation comes from the steady state cavity signal, which is smaller than the lattice originally brought in.

CHAPTER VII

CONCLUSION AND OUTLOOK

7.1 Cavity QED Experiment

In this thesis, a cavity system with the ability of detecting individually trapped atoms in a 1D optical lattice has been presented. The developed techniques of deterministic delivery and selective addressability of single atoms in the cavity system allow the next generation experiments to advance in utilizing single-atom qubit in the cavity system for quantum information protocols.

A dual lattice cavity system was explored in the many-atom regime. The system consists of two 1D optical lattices coupled to the same cavity with dedicated external probe lasers. The optical lattices and the probes are independently controllable and the interactions between atoms in these two lattices through the cavity photons have been observed. A semi-classical model was established based on the Jaynes-Cummings model with low number of atoms and it well describes the dynamics of the interaction between the atoms in these independently controlled lattices.

Performing logic gate operations and generating large-scale qubits have always been important research goals in the field of quantum information science. Proposed schemes for implementing controlled-Z, controlled phase-flip and Hadamard gates on two atomic qubits through cavity-assisted interaction in a dual lattice cavity system have been made [143, 144]. The dual lattice cavity system combined with the ability to identify single atoms in the 1D optical lattice and bring them back into the cavity on demand suggests a potential way to scale up the number of qubits in the cavity system. This is similar to the concepts of the scalable ion trap designs, where the trap is divided into the interaction region (trapping sites in the cavity mode) and

the storage regions (trapping sites outside the cavity mode). The cavity-assisted interaction in the strong coupling regime enables gate operation rates much faster than the decoherence rate, and the long storage time of single atoms in the optical traps makes it possible to greatly increase the repetition rate by reusing the qubits many times before losing them from the trap. Future cavity QED experiments can be envisioned that will provide both features presented in this thesis and enable future breakthroughs in the field of quantum information science.

7.2 Single Atom Trapping Experiment

In the other half of the thesis, experimental work on the characterization of single atoms in the optical dipole traps and the measurements of single atom fluorescent spectroscopies have been presented. The objective is to provide a extensive study on the optically trapped single atoms and the heating mechanism during the detection process for utilizing single atoms as long-lived atomic qubits.

The work begins with the construction of our newly designed single focus trap that uses the same optics as the detection system. The high numerical aperture microscope objective allows us to focus the 1064 nm trap beam to 2.5 μm minimum waist. This creates a single focus trap in the collisional blockade regime, which is ideal for the single atom experiments.

Next, the trapping potential is characterized by trap frequency measurements and compared to our previous 1D retro-reflecting optical lattice design. This new trap reduces the optical power required to create the same trapping potential compared to the 1D retro-reflecting optical lattice by a factor of 5; therefore, allows us to store single atoms in a much deeper trap that is robust against the probe induced heating.

Improvements have also been made to the detection system. The gated probing/cooling technique allows us to continuously observe long-lived atoms with high signal to noise ratio that is comparable to the destructive detection methods. Single

atom fluorescent spectroscopies with linearly and circularly polarized probe beams are taken with this technique to demonstrate and quantify the differential light shifts of the $5P_{3/2}$ $F' = 3$ Zeeman states.

The temperature of the atoms in the optical dipole traps are measured with the drop and recapture technique, which leads to the study of probe induced heating. The relation between single atom storage time and probe time per cycle is explored under different conditions, providing a better understanding on the trade-off between atom storage time and signal strength.

The future work of this experiment will be focused on utilizing these individually trapped atomic qubits in quantum information protocols based upon the current results. For instance, optical pumping is essential in the generation of entangled photon pairs [58, 141]. The optical pumping of ^{87}Rb atoms to the $|F = 2, m_F = \pm 2\rangle \rightarrow |F' = 3, m_{F'} = \pm 3\rangle$ cycling transition can be achieved by shining the σ^+ and σ^- lights resonant to the $F = 2 \rightarrow F' = 3$ transition. On the other hand, ^{87}Rb atoms can be optically pumped to the $|F = 2, m_F = 0\rangle$ state by shining linearly polarized $F = 2 \rightarrow F' = 2$ light. The dipole forbidden $|F = 2, m_F = 0\rangle \rightarrow |F' = 2, m_{F'} = 0\rangle$ transition prevents the atom being pumped after it falls into the $|F = 2, m_F = 0\rangle$ state. In both cases, a repumping laser is needed to bring the atoms out of the $F = 1$ dark state.

The newly designed single focus trap allows us to increase the trapping potential to 10 mK with the existing apparatus; therefore, significantly increases the amount of the maximum scattered photons from a single atom before being heated out of the trap. The increase in the trapping potential would drastically increase the differential light shifts of the $5P_{3/2}$ excited states to over 100 MHz; which would, in turn, greatly reduce the optical pumping efficiency. This can be prevented by implementing the scheme discussed in Chapter 2 to eliminate the light shift quadratically dependent on $m_{F'}$. Another solution is to utilize a electro-optic modulator (EOM) to create

sidebands that simultaneously address these well-separated transitions.

With these improvements, robust and long-lived single-atom qubits can be implemented for quantum information experiments that require precise addressing of the energy levels, and hence provides foundations for future developments in the research of quantum information science.

APPENDIX A

PROGRESS TOWARDS MECHANICAL OPTICAL CONVEYOR BELT

In Chapter 4, the technique of transporting atoms from the MOT to the cavity with optical conveyor belt is introduced. A high power beam is required for $3 \sim 4$ mm travel distance with sufficient trap depth. In the experimental setup of the optical conveyor belt, the AOM efficiency of the first order beam usually ranges from 60% to 70%. Along with other losses, $9 \simeq 10$ W of the total 18 W optical power is available for the trap beam. In the system with two optical conveyor belts, the trap only works marginally.

On the other hand, in the cavity experiment where strong interaction between the atoms and the cavity is desired, the cavity mirror spacing is typically on the order of hundreds of μm. A high power gaussian beam passing through the cavity will inevitably heat up the cavity. In our experiment, sending laser beams with $\sim$8 W optical power through a 500 μm cavity will thermally expand the cavity length by about 2×780 nm through inspection of the cavity mode, and it takes over an hour to reach the equilibrium. These are the two major reasons that drive the pursuit of a new trap design that requires less optical power.

A retro-reflecting optical lattice is a possible candidate for the goal of using the least optical power to create the trap with the same trapping potential. Wave envelopes in the retro-reflecting optical lattice can not be moved in the same fashion as the counter-propagating beam optical lattice. In Figure 54, it is shown that by physically moving the retro-reflecting mirror, the wave envelopes and the trapped atom move over the same distance. Without the need for setting up the counter-propagating

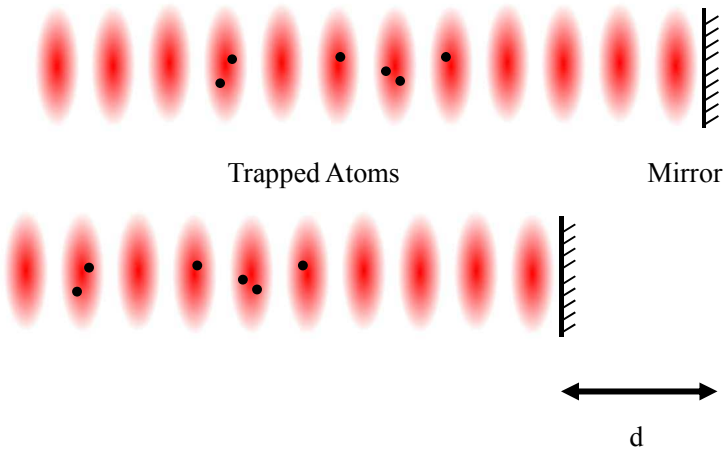

Figure 54: In the retro-reflecting optical lattice, the mirror defines the node of the standing wave. By moving the mirror along the beam propagation direction, the wave envelopes, and hence the trapped atom also move in the same direction over the same.

beam and the use of an AOM, only ∼40% of the optical power is required to achieve the same trapping potential. In this chapter, we will focus on the developments of mechanical optical conveyor belt.

A.1 Experimental Setup

One of the best technologies for positioning a physical object with submicron precision is the piezoelectric stacks. Typical travel distance of a preloaded piezo actuator ranges from tens of microns to hundreds of microns, which is much shorter than the distance between the MOT and the cavity in the experiment. Though long travel distance can be achieved by mounting several piezo actuators in series, it requires mounting space over a meter which is not realistic in our experiment. The cost and space effective solution is to combine the pneumatic cylinder (Clippard AF-RSR-10-1/2-V) and the open-loop preloaded piezo actuator (Physik Instrumente P840.60), in which the pneumatic cylinder pushes the mirror for several millimeters and the piezo actuator is responsible for precision positioning of the atoms relative to the cavity mode. Figure 55 shows the schematic of the experiment. The retro-reflecting mirror is mounted on a 1D translation stage (S1), and the stage motion is controlled by a

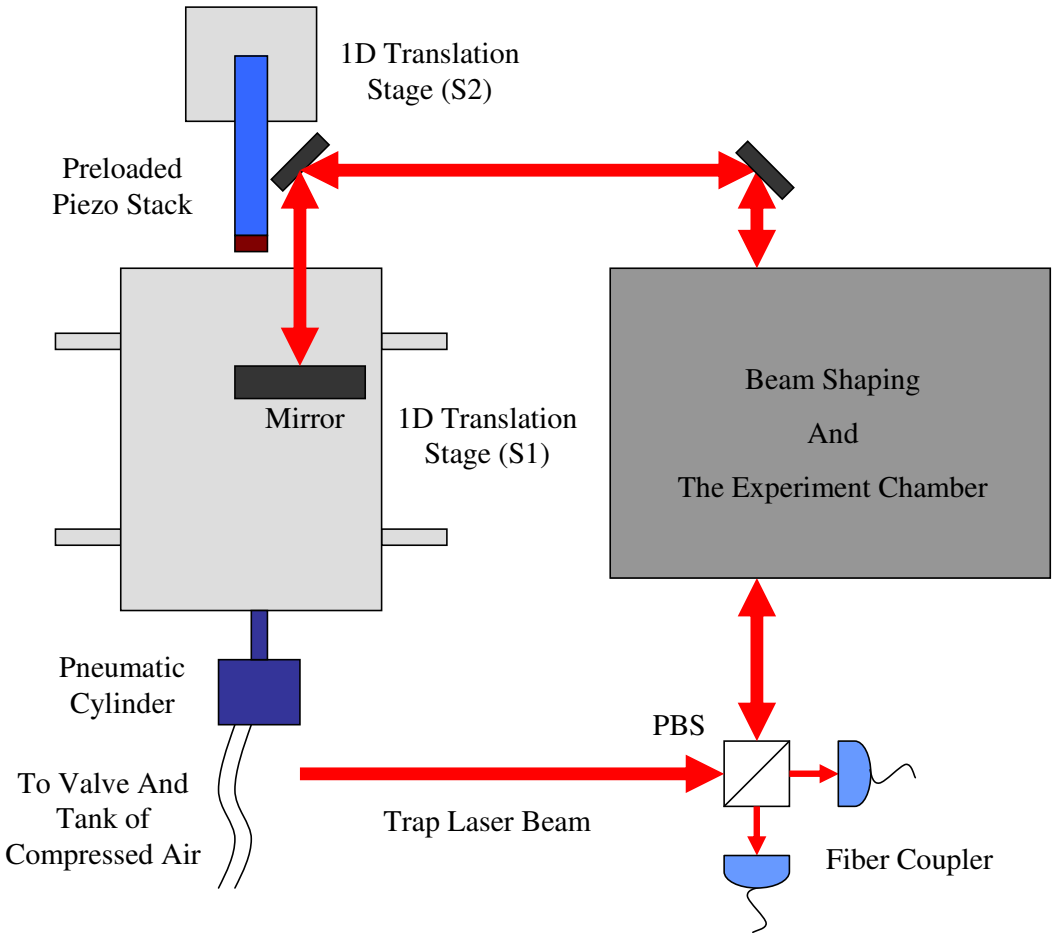

Figure 55: Illustrative digram showing the setup for the mechanical optical conveyor belt. The retro-reflecting mirror is mounted on a 1D translation stage (S1). The stage is pushed by the pneumatic cylinder when the valve to the air supply is open, stopped when the stage hits the rubber glued on the preloaded piezo stack mounted on another translation stage (S2).

pneumatic cylinder. A 3-way valve (Clippard ET-3-6 VDC) is utilized for external control of the air flow from the compressed air tank to the cylinder. The preloaded piezo actuator, which is also mounted on a 1D translation stage (S2), is used to stop the motion of S1 along with the mirror. The gap between the tip of the piezo actuator and S1 corresponds to the maximum travel distance of the mirror, is adjusted to the distance between the MOT and cavity with the use of S2.

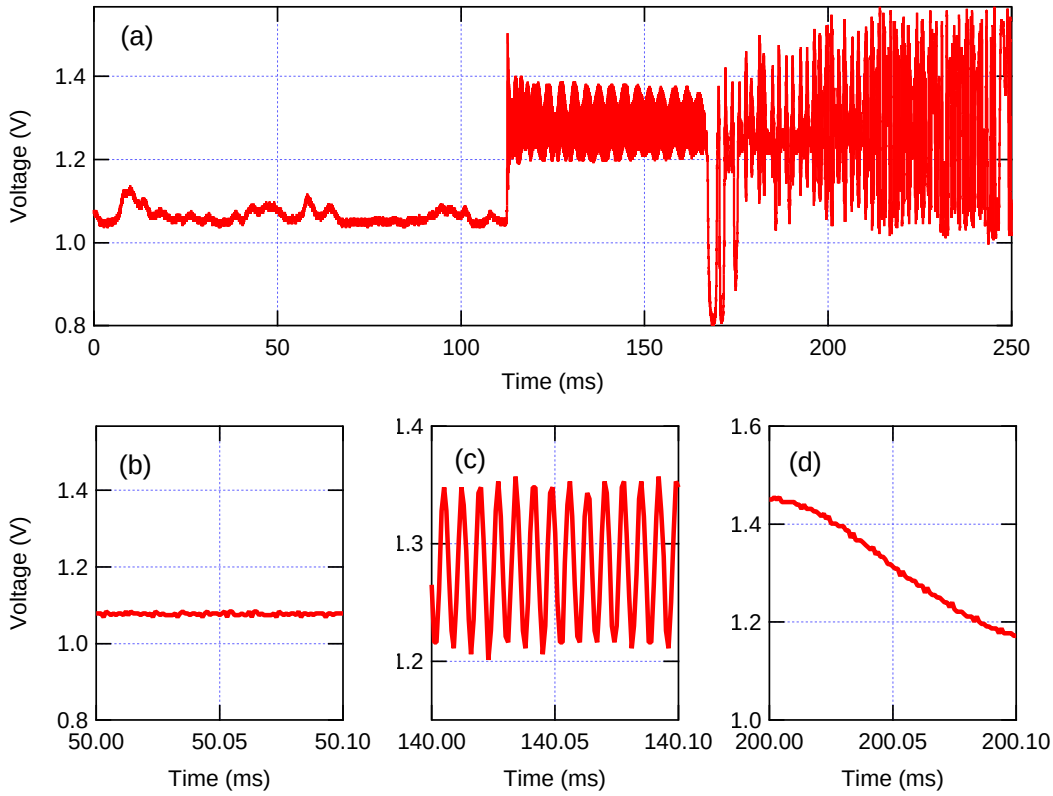

Figure 56: The detector signal of the interference fringes for one run is shown in (a). The zoomed-in view in (b), (c), and (d) correspond to the stage before, during, and after the mirror moves. The oscillation in (d) results from the mechanical vibration after the stage is stopped by the piezo actuator, which shows different pattern compared to (c).

A.2 Speed Measurement of The Optical Lattice

It is important to measure the speed of the optical lattice for the purpose of comparing it to the former experimental setup. As shown in Figure 55, a PBS is used to tap off a small percentage of optical power from the incoming beam and the retro-reflected beam. These two beams are fiber coupled and combined on a 50/50 neutral beamsplitter, and the output is directed to a optical detector. The interference fringes formed on the detector moves as the retro-reflection mirror moves. By counting the number of fringes swept across the sensor of the detector, the travel distance of the mirror, and hence the optical lattice, can be determined accurately to the level of half wavelength of the trap laser, 532 nm in this case.

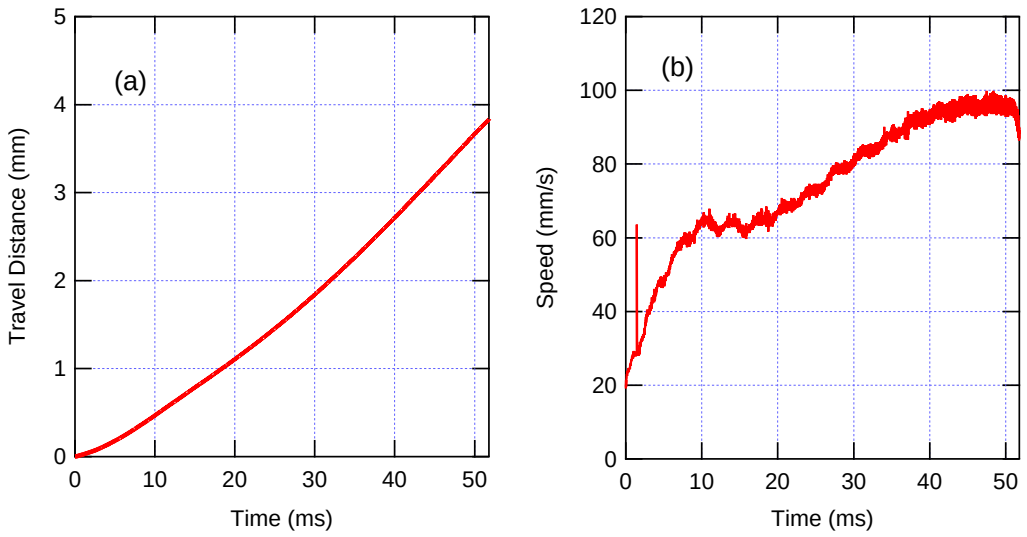

Figure 57: (a) The travel distance of the mirror by counting the number of interference fringes swept through the detector. (b) The speed of the mirror.

Figure 56 shows the detector signal for one trial. A trigger signal opens the valve at 112 ms, the stage moves about 50 ms before hitting the piezo actuator and stopped. The stage vibrates for another few hundred milliseconds after it is brought to stop, it is believed that this causes significant loss of atoms in the trap. The travel distance and speed is plotted in Figure 57. The travel distance is obtained by counting the number of interference fringes swept through the detector and multiply by the half the trap laser wavelength, and the speed is obtained by taking the derivative of the above data. By changing the pressure of the supplied air with regulator, the average speed can be adjusted accordingly.

Fluorescent images of the atoms in the optical lattice are taken with Andor camera before and after moving the optical lattice. It is shown that the vibration of the mirror after it is stopped causes great loss of atoms in the trap. Attempts have been made to reduce the impact by lowering the speed of the mirror and replacing various vibration absorptive materials for stopping the stage motion. Nevertheless, the loss rate remains high and makes this scheme impractical, unfortunately.

A.3 Possible Improvements

By using the interferometric detection technique, it is demonstrated that the current mechanical optical conveyor setup has the required travel range and the ability to accurately position the atoms. Nevertheless, the vibration caused by stopping the conveyor is responsible for significant loss of the atoms and makes the current design impractical. The possible improvements include connecting many piezo stack in series or using low vibration linear actuators. With these improvements, the mechanical optical conveyor with long travel distance and low atom loss can greatly increase the trapping potential with the same optical power, which can in turn reduce the atom loss rate and improve the success rate of the experiment described in Chaptor 6.

REFERENCES

[1] M. Planck, "Über eine Verbesserung der Wienschen Spectralgleichung," *Verhandl. Dtsc. Phys. Ges.* **2**, 202 (1900).

[2] A. Einstein, "Über einen die Erzeugung und Verwandlung des Lichtes betreffenden heuristischen Gesichtspunkt," *Annalen der Physik* **322**, 132 (1905).

[3] N. Bohr, "On the Constitution of Atoms and Molecules, Part II Systems Containing Only a Single Nucleus," *Philosophical Magazine* **26**, 146 (1913).

[4] N. Bohr, "The spectra of hydrogen and helium," *Nature* **95**, 6 (1915).

[5] W. Gerlach and O. Stern, "Das magnetische Moment des Silberatoms," *Zeitschrift für Physik* **9**, 353 (1922).

[6] A. H. Compton, "A quantum theory of the scattering of x-rays by light elements," *Physical Review* **21**, 0483 (1923).

[7] P. A. M. Dirac, *The principles of quantum mechanics*, 4th ed. (Clarendon Press, Oxford, 1958).

[8] D. Hilbert, T. Sauer, and U. Majer, *David Hilbert's lectures on the foundations of physics, 1915-1927 : relativity, quantum theory and epistemology* (Springer, Dordrecht ; New York, 2009).

[9] J. Von Neumann, *Mathematical foundations of quantum mechanics*Investigations in physics (Princeton University Press, Princeton N.J., 1955).

[10] N. Ramsey, *Molecular beams* (Clarendon Press, Oxford, 1956).

[11] I. I. Rabi, S. Millman, P. Kusch, and J. R. Zacharias, "The Molecular Beam Resonance Method for Measuring Nuclear Magnetic Moments. The Magnetic Moments of $_3Li^6$, $_3Li^7$ and $_9F^{19}$," *Phys. Rev.* **55**, 526 (1939).

[12] N. Ramsey, *Nuclear moments* (Wiley, New York, 1953).

[13] L. Essen and J. V. L. Parry, "An Atomic Standard of Frequency and Time Interval: A Cæsium Resonator," *Nature* **176**, 280 (1955).

[14] A. L. Schawlow and C. H. Townes, "Infrared and Optical Masers," *Phys. Rev.* **112**.

[15] T. H. Maiman, "Stimulated Optical Radiation in Ruby," *Nature* **187**.

[16] T. W. Hänsch and A. L. Schawlow, "Cooling of Gases by Laser Radiation," *Optics Communications* **13**, 68 (1975).

[17] D. Wineland and H. Dehmelt, "Proposed $10^{14}\delta\nu < \nu$ Laser Fluorescence Spectroscopy on TI^+ Mono-Ion Oscillator III," *Bulletin of the American Physical Society* **20**, 637 (1975).

[18] M. H. Anderson, J. R. Ensher, M. R. Matthews, C. E. Wieman, and E. A. Cornell, "Observation of Bose-Einstein Condensation in a Dilute Atomic Vapor," *Science* **269**, 198 (1995).

[19] S. Chu, "The manipulation of neutral particles," *Reviews of Modern Physics* **70**, 685 (1998).

[20] W. D. Phillips, "Laser cooling and trapping of neutral atoms," *Reviews of Modern Physics* **70**, 721 (1998).

[21] C. N. Cohen-Tannoudji, "Manipulating atoms with photons," *Reviews of Modern Physics* **70**, 707 (1998).

[22] Z. Hu and H. J. Kimble, "Observation of a Single-Atom in a Magnetooptical Trap," *Optics Letters* **19**, 1888 (1994).

[23] D. Frese, B. Ueberholz, S. Kuhr, W. Alt, D. Schrader, V. Gomer, and D. Meschede, "Single atoms in an optical dipole trap: Towards a deterministic source of cold atoms," *Physical Review Letters* **85**, 3777 (2000).

[24] N. Schlosser, G. Reymond, P. I, and P. Grangier, "Sub-poissonian loading of single atoms in a microscopic dipole trap," *Nature* **411**, 1024 (2001).

[25] D. Schrader, I. Dotsenko, M. Khudaverdyan, Y. Miroshnychenko, A. Rauschenbeutel, and D. Meschede, "Neutral atom quantum register," *Physical Review Letters* **93**, 150501 (2004).

[26] T. Grünzweig, A. Hilliard, M. McGovern, and M. F. Andersen, "Near-deterministic preparation of a single atom in an optical microtrap," *Nature Physics* **6**, 951 (2010).

[27] A. M. Kaufman, B. J. Lester, and C. A. Regal, "Cooling a Single Atom in an Optical Tweezer to Its Quantum Ground State," *Physical Review X* **2**, 041014 (2012).

[28] J. D. Thompson, T. G. Tiecke, A. S. Zibrov, V. Vuletić, and M. D. Lukin, "Coherence and Raman sideband cooling of a single atom in an optical tweezer," (2012), arXiv:1209.3028.

[29] K. D. Nelson, X. Li, and D. S. Weiss, "Imaging single atoms in a three-dimensional array," *Nat Phys* **3**, 556 (2007).

[30] W. S. Bakr, J. I. Gillen, A. Peng, S. Folling, and M. Greiner, "A quantum gas microscope for detecting single atoms in a Hubbard-regime optical lattice," *Nature* **462**, 74 (2009).

[31] M. Karski, L. Förster, J. M. Choi, W. Alt, A. Widera, and D. Meschede, "Nearest-Neighbor Detection of Atoms in a 1D Optical Lattice by Fluorescence Imaging," *Phys. Rev. Lett.* **102**, 053001 (2009).

[32] J. Volz, M. Weber, D. Schlenk, W. Rosenfeld, J. Vrana, K. Saucke, C. Kurtsiefer, and H. Weinfurter, "Observation of entanglement of a single photon with a trapped atom," *Physical Review Letters* **96**, 030404 (2006).

[33] E. Urban, T. A. Johnson, T. Henage, L. Isenhower, D. D. Yavuz, T. G. Walker, and M. Saffman, "Observation of Rydberg blockade between two atoms," *Nature Physics* **5**, 110 (2009).

[34] A. Gaëtan, Y. Miroshnychenko, T. Wilk, A. Chotia, M. Viteau, D. Comparat, P. Pillet, A. Browaeys, and P. Grangier, "Observation of collective excitation of two individual atoms in the Rydberg blockade regime," *Nature Physics* **5**, 115 (2009).

[35] T. Wilk, A. Gaëtan, C. Evellin, J. Wolters, Y. Miroshnychenko, P. Grangier, and A. Browaeys, "Entanglement of Two Individual Neutral Atoms Using Rydberg Blockade," *Physical Review Letters* **104**, 010502 (2010).

[36] K. C. Younge, B. Knuffman, S. E. Anderson, and G. Raithel, "State-Dependent Energy Shifts of Rydberg Atoms in a Ponderomotive Optical Lattice," *Physical Review Letters* **104**, 173001 (2010).

[37] J. Y. Kim, J. S. Lee, J. H. Han, and D. Cho, "Optical dipole trap without inhomogeneous ac stark broadening," *Journal of the Korean Physical Society* **42**, 483 (2003).

[38] F. Markert, P. Würtz, A. Koglbauer, T. Gericke, A. Vogler, and H. Ott, "ac-Stark shift and photoionization of Rydberg atoms in an optical dipole trap," *New Journal of Physics* **12**, 113003 (2010).

[39] M. K. Tey, Z. L. Chen, S. A. Aljunid, B. Chng, F. Huber, G. Maslennikov, and C. Kurtsiefer, "Strong interaction between light and a single trapped atom without the need for a cavity," *Nature Physics* **4**, 924 (2008).

[40] M. J. Gibbons, S. Y. Kim, K. M. Fortier, P. Ahmadi, and M. S. Chapman, "Achieving very long lifetimes in optical lattices with pulsed cooling," *Physical Review A* **78**, 023401 (2008).

[41] M. J. Gibbons, C. D. Hamley, C. Y. Shih, and M. S. Chapman, "Nondestructive Fluorescent State Detection of Single Neutral Atom Qubits," *Physical Review Letters* **106**, 133002 (2011).

[42] M. O. Scully and M. S. Zubairy, *Quantum optics* (Cambridge University Press, Cambridge ; New York, 1997).

[43] D. F. Walls and G. J. Milburn, *Quantum optics* (Springer-Verlag, Berlin ; New York, 1995).

[44] P. R. Berman, *Cavity quantum electrodynamics* (Academic Press, Boston, 1994).

[45] E. M. Purcell, "Spontaneous Emission Probabilities at Radio Frequencies," *Physical Review* **69**, 681 (1946).

[46] E. T. Jaynes and F. W. Cummings, "Comparison of Quantum and Semiclassical Radiation Theories with Application to Beam Maser," *Proceedings of the Ieee* **51**, 89 (1963).

[47] Y. Kaluzny, P. Goy, M. Gross, J. M. Raimond, and S. Haroche, "Observation of Self-Induced Rabi Oscillations in Two-Level Atoms Excited Inside a Resonant Cavity: The Ringing Regime of Superradiance," *Phys. Rev. Lett.* **51**, 1175 (1983).

[48] D. Meschede, H. Walther, and G. Müller, "One-Atom Maser," *Phys. Rev. Lett.* **54**, 551 (1985).

[49] G. Rempe, H. Walther, and N. Klein, "Observation of quantum collapse and revival in a one-atom maser," *Phys. Rev. Lett.* **58**, 353 (1987).

[50] M. Brune, J. M. Raimond, P. Goy, L. Davidovich, and S. Haroche, "Realization of a two-photon maser oscillator," *Phys. Rev. Lett.* **59**, 1899 (1987).

[51] M. G. Raizen, R. J. Thompson, R. J. Brecha, H. J. Kimble, and H. J. Carmichael, "Normal-Mode Splitting and Linewidth Averaging for 2-State Atoms in an Optical Cavity," *Physical Review Letters* **63**, 240 (1989).

[52] F. Bernardot, P. Nussenzveig, M. Brune, J. M. Raimond, and S. Haroche, "Vacuum Rabi Splitting Observed on a Microscopic Atomic Sample in a Microwave Cavity," *Europhysics Letters* **17**, 33 (1992).

[53] R. J. Thompson, G. Rempe, and H. J. Kimble, "Observation of Normal-Mode Splitting for an Atom in an Optical Cavity," *Physical Review Letters* **68**, 1132 (1992).

[54] S. Nußmann, K. Murr, M. Hijlkema, B. Weber, A. Kuhn, and G. Rempe, "Vacuum-stimulated cooling of single atoms in three dimensions," *Nature Physics* **1**, 122 (2005).

[55] K. M. Fortier, Y. Kim, M. J. Gibbons, P. Ahmadi, and M. S. Chapman, "Deterministic loading of individual atoms to a high-finesse optical cavity," *Physical Review Letters* **98**, 233601 (2007).

[56] M. Khudaverdyan, W. Alt, I. Dotsenko, T. Kampschulte, K. Lenhard, A. Rauschenbeutel, S. Reick, K. Schörner, A. Widera, and D. Meschede, "Controlled insertion and retrieval of atoms coupled to a high-finesse optical resonator," *New Journal of Physics* **10**, 073023 (2008).

[57] A. Kuhn, M. Hennrich, and G. Rempe, "Deterministic Single-Photon Source for Distributed Quantum Networking," *Phys. Rev. Lett.* **89**, 067901 (2002).

[58] T. Wilk, S. C. Webster, A. Kuhn, and G. Rempe, "Single-atom single-photon quantum interface," *Science* **317**, 488 (2007).

[59] M. Lettner, M. Mücke, S. Riedl, C. Vo, C. Hahn, S. Baur, J. Bochmann, S. Ritter, S. Dürr, and G. Rempe, "Remote Entanglement between a Single Atom and a Bose-Einstein Condensate," *Physical Review Letters* **106**, 210503 (2011).

[60] M. A. Armen and H. Mabuchi, "Low-lying bifurcations in cavity quantum electrodynamics," *Physical Review A* **73**, 063801 (2006).

[61] S. Gupta, K. L. Moore, K. W. Murch, and D. M. Stamper-Kurn, "Cavity nonlinear optics at low photon numbers from collective atomic motion," *Physical Review Letters* **99**, 213601 (2007).

[62] N. Brahms, T. Botter, S. Schreppler, D. W. C. Brooks, and D. M. Stamper-Kurn, "Optical Detection of the Quantization of Collective Atomic Motion," *Physical Review Letters* **108**, 133601 (2012).

[63] K. W. Murch, K. L. Moore, S. Gupta, and D. M. Stamper-Kurn, "Observation of quantum-measurement backaction with an ultracold atomic gas," *Nature Physics* **4**, 561 (2008).

[64] A. Wallraff, D. I. Schuster, A. Blais, L. Frunzio, R.-S. Huang, J. Majer, S. Kumar, S. M. Girvin, and R. J. Schoelkopf, "Strong coupling of a single photon to a superconducting qubit using circuit quantum electrodynamics," *Nature* **431**, 162 (2004).

[65] T. Yoshie, A. Scherer, J. Hendrickson, J. Hendrickson, G. Khitrova, H. M. Gibbs, G. Rupper, C. Ell, O. B. Shchekin, and D. G. Deppe, "Vacuum Rabi splitting with a single quantum dot in a photonic crystal nanocavity," *Nature* **432**, 200 (2004).

[66] J. P. Reithmaier, G. Sek, A. Loffler, C. Hofmann, S. Kuhn, S. Reitzenstein, L. V. Keldysh, V. D. Kulakovskii, T. L. Reinecke, and A. Forchel, "Strong coupling in a single quantum dot-semiconductor microcavity system," *Nature* **432**, 197 (2004).

[67] J. A. Sauer, K. M. Fortier, M. S. Chang, C. D. Hamley, and M. S. Chapman, "Cavity QED with optically transported atoms," *Physical Review A* **69**, 051804(R) (2004).

[68] S. Chu, J. E. Bjorkholm, A. Ashkin, and A. Cable, "Experimental-Observation of Optically Trapped Atoms," *Physical Review Letters* **57**, 314 (1986).

[69] E. L. Raab, M. Prentiss, A. Cable, S. Chu, and D. E. Pritchard, "Trapping of Neutral Sodium Atoms with Radiation Pressure," *Physical Review Letters* **59**, 2631 (1987).

[70] M. A. Nielsen and I. L. Chuang, *Quantum computation and quantum information* (Cambridge University Press, Cambridge ; New York, 2000).

[71] M. Saffman, T. G. Walker, and K. Mølmer, "Quantum information with Rydberg atoms," *Reviews of Modern Physics* **82**, 2313 (2010).

[72] L. Isenhower, E. Urban, X. L. Zhang, A. T. Gill, T. Henage, T. A. Johnson, T. G. Walker, and M. Saffman, "Demonstration of a Neutral Atom Controlled-NOT Quantum Gate," *Physical Review Letters* **104**, 010503 (2010).

[73] I. Bloch, J. Dalibard, and W. Zwerger, "Many-body physics with ultracold gases," *Reviews of Modern Physics* **80**, 885 (2008).

[74] Y. O. Dudin, R. Zhao, T. A. B. Kennedy, and A. Kuzmich, "Light storage in a magnetically dressed optical lattice," *Phys. Rev. A* **81**, 041805 (2010).

[75] H. Katori, T. Ido, and M. Kuwata-Gonokami, "Optimal design of dipole potentials for efficient loading of Sr atoms," *Journal of the Physical Society of Japan* **68**, 2479 (1999).

[76] B. Arora, M. S. Safronova, and C. W. Clark, "Magic wavelengths for the np-ns transitions in alkali-metal atoms," *Physical Review A* **76**, 052509 (2007).

[77] A. Derevianko, "Theory of magic optical traps for Zeeman-insensitive clock transitions in alkali-metal atoms," *Phys. Rev. A* **81**, 051606 (2010).

[78] N. Lundblad, M. Schlosser, and J. V. Porto, "Experimental observation of magic-wavelength behavior of ^{87}Rb atoms in an optical lattice," *Phys. Rev. A* **81**, 031611 (2010).

[79] M. Takamoto, F. L. Hong, R. Higashi, and H. Katori, "An optical lattice clock," *Nature* **435**, 321 (2005).

[80] J. Ye, H. J. Kimble, and H. Katori, "Quantum state engineering and precision metrology using state-insensitive light traps," *Science* **320**, 1734 (2008).

[81] A. D. Ludlow, M. M. Boyd, T. Zelevinsky, S. M. Foreman, S. Blatt, M. Notcutt, T. Ido, and J. Ye, "Systematic study of the Sr-87 clock transition in an optical lattice," *Physical Review Letters* **96**, 033003 (2006).

[82] R. Le Targat, X. Baillard, M. Fouche, A. Brusch, O. Tcherbakoff, G. D. Rovera, and P. Lemonde, "Accurate optical lattice clock with Sr-87 atoms," *Physical Review Letters* **97**, 130801 (2006).

[83] Y. O. Dudin, A. G. Radnaev, R. Zhao, J. Z. Blumoff, T. A. B. Kennedy, and A. Kuzmich, "Entanglement of Light-Shift Compensated Atomic Spin Waves with Telecom Light," *Phys. Rev. Lett.* **105**, 260502 (2010).

[84] S. Zhang, F. Robicheaux, and M. Saffman, "Magic-wavelength optical traps for Rydberg atoms," *Phys. Rev. A* **84**, 043408 (2011).

[85] R. Grimm, M. Weidemüller, and Y. B. Ovchinnikov, "Optical dipole traps for neutral atoms," *Advances in Atomic Molecular, and Optical Physics, Vol. 42* **42**, 95 (2000).

[86] A. Ashkin and J. M. Dziedzic, "Optical Trapping and Manipulation of Viruses and Bacteria," *Science* **235**, 1517 (1987).

[87] D. J. Griffiths, *Introduction to electrodynamics*, 3rd ed. (Prentice Hall, Upper Saddle River, N.J., 1999).

[88] J. D. Jackson, *Classical electrodynamics*, 3rd ed. (Wiley, New York, 1999).

[89] N. Davidson, H. J. Lee, C. S. Adams, M. Kasevich, and S. Chu, "Long Atomic Coherence Times in an Optical Dipole Trap," *Physical Review Letters* **74**, 1311 (1995).

[90] I. Lindgren and J. Morrison, *Atomic many-body theory*, 2nd ed. (Springer-Verlag, Berlin ; New York, 1986).

[91] E. Merzbacher, *Quantum mechanics*, 3rd ed. (Wiley, New York, 1998).

[92] K. Beloy, "*Theory of the ac Stark effect on the atomic hyperfine structure and applications to microwave atomic clocks*," PhD thesis University of Nevada, Reno 2009.

[93] C. J. Joachain, N. J. Kylstra, and R. M. Potvliege, *Atoms in intense laser fields* (Cambridge University Press, Cambridge ; New York, 2011).

[94] D. M. Brink and G. R. Satchler, *Angular momentum* (Clarendon Press, Oxford, 1962).

[95] D. A. Steck, "*Rubidium 87 d line data*," [http://steck.us.alkalidata], 2008.

[96] R. Loudon, *The quantum theory of light*, 3rd ed. (Oxford University Press, Oxford ; New York, 2000).

[97] M. S. Safronova and U. I. Safronova, "Critically evaluated theoretical energies, lifetimes, hyperfine constants, and multipole polarizabilities in ^{87}Rb," *Physical Review A* **83**, 052508 (2011).

[98] A. Kramida, Y. Ralchenko, J. Reader, and N. A. T. (2012), "NIST Atomic Spectra Database (version 5.0)," (2012), [http://physics.nist.gov/asd], (National Institute of Standards and Technology, Gaithersburg, MD.

[99] E. Gomez, F. Baumer, A. D. Lange, G. D. Sprouse, and L. A. Orozco, "Lifetime measurement of the 6s level of rubidium," *Physical Review A* **72**, 012502 (2005).

[100] D. Sheng, A. P. Galván, and L. A. Orozco, "Lifetime measurements of the 5d states of rubidium," *Physical Review A* **78**, 062506 (2008).

[101] J. Marek and P. Munster, "Radiative Lifetimes of Excited-States of Rubidium up to Quantum Number N=12," *Journal of Physics B-Atomic Molecular and Optical Physics* **13**, 1731 (1980).

[102] C. E. Theodosiou, "Lifetimes of Alkali-Metal - Atom Rydberg States," *Physical Review A* **30**, 2881 (1984).

[103] A. Ekers, M. Glódź, J. Szonert, B. Bieniak, K. Fronc, and T. Radelitski, "Inelastic cross-sections and natural lifetimes for the $6^2D_{3/2,5/2}$ and $8^2S_1/2$ states of Rb," *European Physical Journal D* **8**, 49 (2000).

[104] R. F. Gutterres, C. Amiot, A. Fioretti, C. Gabbanini, M. Mazzoni, and O. Dulieu, "Determination of the ^{87}Rb 5p state dipole matrix element and radiative lifetime from the photoassociation spectroscopy of the Rb_2 $0_g^-(P_{3/2})$ long-range state," *Physical Review A* **66**, 024502 (2002).

[105] E. Gomez, S. Aubin, L. A. Orozco, and G. D. Sprouse, "Lifetime and hyperfine splitting measurements on the 7s and 6p levels in rubidium," *Journal of the Optical Society of America B-Optical Physics* **21**, 2058 (2004).

[106] P. Rosenbusch, S. Ghezali, V. A. Dzuba, V. V. Flambaum, K. Beloy, and A. Derevianko, "ac Stark shift of the Cs microwave atomic clock transitions," *Physical Review A* **79**, 013404 (2009).

[107] D. Budker, D. F. Kimball, and D. P. DeMille, *Atomic physics : an exploration through problems and solutions* (Oxford University Press, Oxford ; New York, 2004).

[108] D. A. Varshalovich, A. N. Moskalev, and V. K. Khersonskii, *Quantum theory of angular momentum: irreducible tensors, spherical harmonics, vectors coupling coefficients, 3nj symbols.* (World Scientific Pub., Singapore ; Teaneck, NJ, USA, 1988).

[109] N. L. Manakov, V. D. Ovsiannikov, and L. P. Rapoport, "Atoms in a Laser Field," *Physics Reports-Review Section of Physics Letters* **141**, 319 (1986).

[110] G. Racah, "Theory of complex spectra. II," *Physical Review* **62**, 438 (1942).

[111] R. E. Tuzun, P. Burkhardt, and D. Secrest, "Accurate computation of individual and tables of 3-j and 6-j symbols," *Computer Physics Communications* **112**, 112 (1998).

[112] C. Tuchendler, A. M. Lance, A. Browaeys, Y. R. P. Sortais, and P. Grangier, "Energy distribution and cooling of a single atom in an optical tweezer," *Physical Review A* **78**, 033425 (2008).

[113] H. J. Metcalf and P. Van der Straten, *Laser cooling and trapping* (Springer, New York, 1999).

[114] M. L. Citron, H. R. Gray, C. W. Gabel, and C. R. Stroud, "Experimental Study of Power Broadening in a 2-Level Atom," *Physical Review A* **16**, 1507 (1977).

[115] A. E. Siegman, *Lasers* (University Science Books, Mill Valley, Calif., 1986).

[116] F. Reif, *Fundamentals of statistical and thermal physics* (McGraw-Hill, New York, 1965).

[117] J. A. Sauer, "*Cold Atom Manipulation for Quantum Computing and Control*," PhD thesis Georgia Institute of Technology 2004.

[118] K. Fortier, "*Individual Trapped Atoms For Cavity QED Quantum Information Applications*," PhD thesis Georgia Institute of Technology 2007.

[119] S. Y. Kim, "*Cold Single Atoms For Cavity QED Experiments*," PhD thesis Georgia Institute of Technology 2008.

[120] C. J. Hood, "*Real-Time Measurement and Trapping of Single Atoms by Single Photons*," PhD thesis California Institute of Technology 2000.

[121] G. Rempe, R. J. Thompson, R. J. Brecha, W. D. Lee, and H. J. Kimble, "Optical Bistability and Photon Statistics in Cavity Quantum Electrodynamics," *Physical Review Letters* **67**, 1727 (1991).

[122] H. J. Briegel and B. G. Englert, "Quantum Optical Master-Equations - the Use of Damping Bases," *Physical Review A* **47**, 3311 (1993).

[123] S. M. Tan, "A computational toolbox for quantum and atomic optics," *Journal of Optics B-Quantum and Semiclassical Optics* **1**, 424 (1999).

[124] J. R. Johansson, P. D. Nation, and F. Nori, "QuTiP: An open-source Python framework for the dynamics of open quantum systems," *Computer Physics Communications* **183**, 1760 (2012).

[125] P. D. Nation and J. Johansson, "*QuTiP: The Quantum Toolbox in Python*," [http://qutip.googlecode.com/svn/doc/2.0.0/html/index.html], 2012.

[126] A. T. Rosenberger, L. A. Orozco, H. J. Kimble, and P. D. Drummond, "Absorptive Optical Bistability in 2-State Atoms," *Physical Review A* **43**, 6284 (1991).

[127] H. J. Carmichael, "Quantum Fluctuations in Absorptive Bistability without Adiabatic Elimination," *Physical Review A* **33**, 3262 (1986).

[128] B. P. Anderson and M. A. Kasevich, "Loading a vapor-cell magneto-optic trap using light-induced atom desorption," *Physical Review A* **63**, 023404 (2001).

[129] F. Favre, D. Leguen, J. C. Simon, and B. Landousies, "External-Cavity Semiconductor-Laser with 15-Nm Continuous Tuning Range," *Electronics Letters* **22**, 795 (1986).

[130] C. C. Bradley, J. Chen, and R. G. Hulet, "Instrumentation for the Stable Operation of Laser-Diodes," *Review of Scientific Instruments* **61**, 2097 (1990).

[131] N. Schlosser, G. Reymond, and P. Grangier, "Collisional blockade in microscopic optical dipole traps," *Physical Review Letters* **89**, 203005 (2002).

[132] M. J. Gibbons, "*Robust, reusable qubits for quantum information applications*," PhD thesis Georgia Institute of Technology 2011.

[133] L. Allen and J. H. Eberly, *Optical resonance and two-level atoms* (Wiley, New York, 1975).

[134] J. Vanier and C. Audoin, *The Quantum Physics of Atomic Frequency Standards* (IOP Publishing, Ltd., Bristol, England, 1990).

[135] A. Fuhrmanek, R. Bourgain, Y. R. P. Sortais, and A. Browaeys, "Light-assisted collisions between a few cold atoms in a microscopic dipole trap," *Phys. Rev. A* **85**, 062708 (2012).

[136] J. W. Wu, R. Newell, M. Hausmann, D. J. Vieira, and X. X. Zhao, "Loading dynamics of optical trap and parametric excitation resonances of trapped atoms," *Journal of Applied Physics* **100**, 054903 (2006).

[137] M.-S. Chang, "*Coherent Spin Dynamics of a Spin-1 Bose-Einstein Condensate*," PhD thesis Georgia Institute of Technology 2006.

[138] S. Friebel, C. D'Andrea, J. Walz, M. Weitz, and T. W. Hansch, "CO_2-laser optical lattice with cold rubidium atoms," *Physical Review A* **57**, R20 (1998).

[139] A. Weis and G. D. Domenico, "*Optical Pumping: Population Dynamics*," [http://demonstrations.wolfram.com/OpticalPumpingPopulationDynamics/].

[140] T. Pellizzari, S. A. Gardiner, J. I. Cirac, and P. Zoller, "Decoherence, Continuous Observation, and Quantum Computing - a Cavity Qed Model," *Physical Review Letters* **75**, 3788 (1995).

[141] X. X. Yi, X. H. Su, and L. You, "Conditional quantum phase gate between two 3-state atoms," *Physical Review Letters* **90**, 097902 (2003).

[142] I. B. Mekhov, C. Maschler, and H. Ritsch, "Probing quantum phases of ultracold atoms in optical lattices by transmission spectra in cavity quantum electrodynamics," *Nature Physics* **3**, 319 (2007).

[143] P. Xue and Y. F. Xiao, "Universal quantum computation in decoherence-free subspace with neutral atoms," *Physical Review Letters* **97**, 140501 (2006).

[144] L.-M. Duan, B. Wang, and H. J. Kimble, "Robust quantum gates on neutral atoms with cavity-assisted photon scattering," *Physical Review A* **72**, 032333 (2005).

[145] S. Nußmann, M. Hijlkema, B. Weber, F. Rohde, G. Rempe, and A. Kuhn, "Submicron positioning of single atoms in a microcavity," *Physical Review Letters* **95**, 173602 (2005).

[146] K. Murr, S. Nußmann, T. Puppe, M. Hijlkema, B. Weber, S. C. Webster, A. Kuhn, and G. Rempe, "Three-dimensional cavity cooling and trapping in an optical lattice," *Physical Review A* **73**, 063415 (2006).